Doctoral Dissertation (Censored)

博士論文（要約）

Terahertz nonlinear optical responses in high-temperature cuprate superconductors

(銅酸化物高温超伝導体における テラヘルツ非線形光学応答の研究)

A Dissertation Submitted for the Degree of Doctor of Philosophy

December 2020

令和2年12月博士(理学)申請

Department of Physics, Graduate School of Science,
The University of Tokyo
東京大学大学院理学系研究科
物理学専攻

Kota Katsumi
勝見　恒太

Abstract

Ever since the discovery of the high-temperature cuprate superconductors, tremendous research has been performed to uncover the mechanism of superconductivity. Nevertheless, their unusual physical properties are long-standing mysteries in condensed matter physics.

One of the intriguing phenomena in cuprate superconductors is the superconducting fluctuations. To understand how the Cooper pairs emerge from the complex metallic state, various experiments have been performed to elucidate the onset temperature of the superconducting fluctuations. Nevertheless, the reported onset temperatures depend on experimental techniques, and a unified understanding of the onset of superconducting fluctuations is still lacking. Thus, a novel approach that can sensitively probe the superconducting order parameter has been desired.

Another remarkable phenomenon is the photo-induced superconductivity, recently reported in various types of cuprate superconductors. It has been reported that a Josephson plasma resonance (JPR)-like response emerges in the c-axis reflectivity and concomitantly the imaginary part of the optical conductivity $\sigma_2(\omega)$ exhibits the $1/\omega$-like response after the irradiation of an intense laser pulse even at temperatures far above the superconducting critical temperature (T_c), and interpreted as photo-induced superconductivity. However, in principle, there remains an ambiguity that one cannot distinguish the $1/\omega$-response of the superconductivity and the Drude response of the quasiparticle (QP) excitation with a low scattering rate in the measured terahertz (THz) frequency range. Since the photo-induced $1/\omega$-like response in the $\sigma_2(\omega)$ spectrum disappears in a few picoseconds, it cannot be investigated by resistivity or magnetic susceptibility measurements. Therefore, an alternative ultrafast probe of the superconducting order parameter has been required.

In this study, we have investigated the superconducting fluctuations and

the photo-induced nonequilibrium superconductivity via the THz nonlinear optical responses caused by the collective excitation of the superconducting order parameter in high-T_c cuprate superconductors: the Higgs mode and JPR, which directly reflect the development of the superconducting order parameter within a picosecond time resolution.

First, we have investigated the Higgs-mode response through the THz Kerr effect in $Bi_2Sr_2CaCu_2O_{8+x}$ (BSCCO) thin films utilizing the THz pump-optical probe spectroscopy. In the THz Kerr signal, two onset temperatures are identified. Combining the results of single-crystalline samples, we have found that the lower one ($T_1^{\rm ons}$) is slightly above T_c, whereas the higher one ($T_2^{\rm ons}$) is located substantially higher than T_c. $T_1^{\rm ons}$ coincides with that of the superfluid density evaluated from the THz optical conductivity measurements, indicating the the superconducting phase fluctuation on the picosecond time scale evolves from slightly above T_c, while the static superconducting phase coherence develops below T_c. On the other hand, the coincidence between $T_2^{\rm ons}$ and the superconducting gap opening temperature in the previous studies for BSCCO suggests that $T_2^{\rm ons}$ is associated with the preformed Cooper pairs.

Next, we have applied the THz nonlinear optical responses to elucidate the photo-induced nonequilibrium state in cuprate superconductors. To this end, we have started from the optical pump-THz probe spectroscopy for an underdoped $YBa_2Cu_3O_{6+y}$ (YBCO). We have indeed observed the photo-induced $1/\omega$-like increase in the imaginary part of the c-axis optical conductivity above T_c, consistent with the previous studies. However, the a-axis THz reflectivity is shown to decrease upon the photo-excitation, which is against the interpretation of the photo-induced superconductivity.

The observed prompt optical conductivity in YBCO is further examined by the Higgs-mode response by THz pump-optical probe spectroscopy. We have identified the THz-pulse driven Higgs mode and the superconducting QP excitation below T_c in the THz-pump induced optical reflectivity change $\Delta R/R$. When the sample is irradiated with near-infrared (NIR) pump pulse below T_c, the Higgs-mode and QP responses are suppressed, which agrees with the photo-induced destruction of the superconductivity. Above T_c, neither the Higgs mode nor the QP responses are observed in $\Delta R/R$, indicating that it is unlikely to attribute the photo-induced state above T_c to the superconducting phase.

To further examine the photo-induced state above T_c, we have studied the THz third-harmonic generation (THG) caused by the nonlinear c-axis

Josephson current. Using a narrowband THz-pulse, we have observed the THG in the reflected THz electric field from YBCO below T_c. Besides, we have performed the NIR pump-THG probe experiments and shown that the THG intensity below T_c decreases after photo-excitation, consistent with the results of the Higgs mode-response. At 100 K, the THG is not identified either in equilibrium or in the photo-induced state.

Therefore, we have concluded that the optically-induced increase in the imaginary part of the c-axis optical conductivity is attributed to the QP excitation but not to the photo-induced superconductivity. Since the temperature range where the characteristic c-axis transient optical conductivity appears coincides with the pseudogap temperature region, the observed nonequilibrium response is most likely attributed to the QP excitation correlated with the pseudogap phase. Even though the photo-induced state is not ascribed to the superconductivity, it is highly intriguing that coherent QPs with the scattering rate as low as a few THz appear under the photo-excitation in the pseudogap phase, considering the incoherent c-axis transport in equilibrium. This result would provide an important clue to understanding the pseudogap phase.

Notably, the THz nonlinear responses demonstrated here would also provide access to the study of the dynamical interplay between the superconductivity and other competing or coexisting orders in unconventional superconductors (beyond the BCS framework) though the observation of the collective modes arising from those orders in the time domain. Furthermore, being an ultrafast probe of the superconducting order parameter, these THz nonlinear responses would lay the foundation to explore the nonequilibrium superconductivity in a wide variety of unconventional superconductors.

Contents

List of abbreviation

- ARPES : Angle-resolved photoemission spectroscopy
- BCS : Bardeen Cooper Schrieffer
- BSCCO : $Bi_2Sr_2CaCu_2O_{8+x}$
- EO sampling : Electro-optical sampling
- JPR : Josephson plasma resonance
- LBCO : $La_{2-x}Ba_xCuO_4$
- LSCO : $La_{2-x}Sr_xCuO_4$
- MIR : Mid-infrared
- NIR : Near-infrared
- OD : Overdoped
- OP : Optimally doped
- OPA : Optical parametric amplification
- OPOP : Optical pump-optical probe spectroscopy
- OPTP : Optical pump-THz probe spectroscopy
- OP-TPOP : Optical pump-THz pump-optical probe spectroscopy
- QP : Quasiparticle
- THG : Third-harmonic generation
- THz-TDS : Terahertz time-domain spectroscopy
- TPOP : THz pump-optical probe spectroscopy
- UD : Underdoped
- YBCO : $YBa_2Cu_3O_{6+y}$

Chapter 1

Introduction

1.1 Background

Superconductivity was initially discovered by Onnes in 1911, in mercury [1]. Subsequently, various elemental superconductors had been reported, and their superconducting properties were successfully explained by the Bardeen-Cooper-Schrieffer (BCS) theory [2]. In 1986, Bednorz and Müller discovered high-temperature superconductivity in a cuprate $La_{2-x}Ba_xCuO_4$ (LBCO) [3]. Since their physical properties are beyond the framework of the BCS theory, they are classified as "unconventional superconductors." A typical example is that the superconducting gap in the cuprate superconductors shows a d-wave symmetry [4], while that of the BCS superconductors has an isotropic s-wave symmetry. Though tremendous researches have been performed on cuprate superconductors, their unusual physical properties compared to the BCS superconductors are long-standing mysteries in condensed matter physics as described below.

1.1.1 Phase diagram of cuprate superconductors

Figure 1-1(a) illustrates the phase diagram of the hole-doped cuprate superconductors [5, 6]. The non-doped cuprate, which is often called parent compound, is an antiferromagnetic Mott insulator. With increasing the hole concentration p in the CuO_2 plane [Fig. 1-1(b)] of the parent compound, the antiferromagnetic order is suppressed and the superconductivity emerges for $p > 0.05$. The superconducting transition temperature T_c shows a dome-like structure as a function of p. The hole doping which gives the highest su-

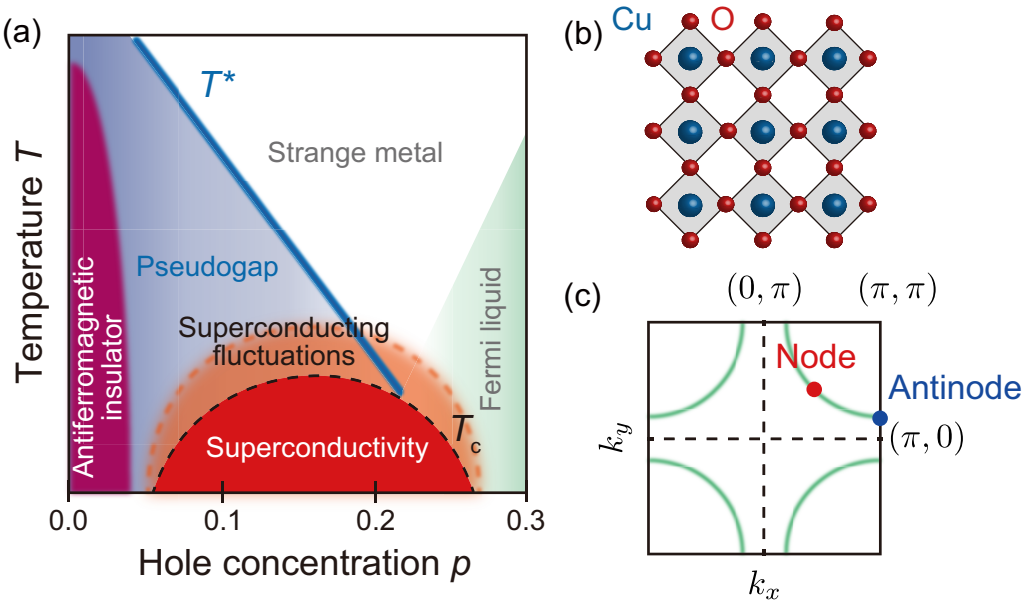

Figure 1-1: (a) Schematic phase diagram of the hole-doped cuprate superconductors. (b) The crystal structure of the CuO_2 planes. (c) Schematic illustration of the Fermi surface in the momentum space.

perconducting transition temperature T_c ($p \sim 0.16$) is referred to as optimal doping. The lower ($p < 0.16$) and higher ($p > 0.16$) hole dopings are called underdoping and overdoping, respectively.

In the heavily overdoped (OD) region with $p > 0.2$, the normal state of the compounds is referred to as the Fermi liquid phase. The quantum oscillation measurement demonstrates a presence of a well-developed Fermi surface, which is well described by the Fermi-liquid theory [7]. One of the most prominent features of the Fermi liquid phase is that the in-plane resistivity follows the squared temperature T^2 above T_c [8]. On the other hand, as the doping is lowered, the in-plane resistivity scales linearly with T and cannot be described by the Fermi liquid theory. Thus, this region is referred to as the strange metal phase [5, 8]. In some studies, the T-linear resistivity behavior has been associated with the critical fluctuations at the vicinity of a quantum critical point of the pseudogap (the point where the pseudogap ends at $T = 0$) [8, 9].

1.1.2 Pseudogap

The underdoped (UD) region is characterized by the pseudogap state. The pseudogap was initially identified in $YBa_2Cu_3O_{6+y}$ (YBCO) by the nuclear magnetic resonance (NMR): the Knit shift and spin-lattice relaxation rate decrease from a characteristic temperature T^* with decreasing temperature, indicating the presence of the energy gap for spin excitations, and the suppression of the density of states around the Fermi energy [10]. Subsequently, anomalies at $T_c < T < T^*$ have been observed by various experimental techniques such as transport, specific heat, tunneling spectroscopy, and c-axis polarized infrared optical conductivity [11].

The structure of the pseudogap in momentum space was revealed by angle-resolved photoemission spectroscopy (ARPES) [12–14]. Figure 1-1(c) illustrates the schematic of the Fermi surface. The pseudogap opens around the antinode of the Fermi surface, and the ungapped Fermi arc emerges around the node. It has been well established by various measurements that both the pseudogap opening temperature and the pseudogap energy increase toward UD region [11]. In the last decade, extensive evidences of the electronic symmetry breaking (nematicity) at or below T^* have been reported [15–22], and thus pseudogap is associated with the nematicity [20–22]. Meanwhile, other candidates of the pseudogap have been proposed such as the density wave [23] or precursor of the superconductivity [6], and the origin of the pseudogap remains elusive.

1.1.3 Superconducting fluctuations

Superconducting fluctuations have been extensively studied over decades to unveil the Cooper pairing above the superconducting transition temperature T_c [24]. To this end, various experimental approaches have been performed: terahertz (THz) [25–28] and microwave spectroscopy [29–31], infrared spectroscopy [32–34], Nernst measurement [35,36], torque magnetometry [37–40], scanning tunneling microscopy (STM) [41], ARPES [42–45], and ultrafast pump-probe spectroscopy [46–49]. Most of these experiments have investigated the onset temperature of the superconducting fluctuations (T_{ons}) to understand how the superconducting coherence emerges from the complex metallic state. Nevertheless, the reported onset temperatures depend on experimental techniques, and a unified framework for the onset of superconducting fluctuations is still lacking.

For instance, in the previous THz and microwave spectroscopy measurements, the onset temperature $T_{\rm ons}$ has been discerned at most 10-20 K above $T_{\rm c}$ in various cuprate superconductors [25–31]. On the other hand, the Nernst, ARPES, and infrared spectroscopy measurements have identified much higher temperatures of $T_{\rm ons}$, up to 50-100 K above $T_{\rm c}$ [32–36, 42–46]. However, the Nernst signal was shown to be enhanced by the stripe order, and its origin is still an open question [50]. Therefore, an alternative method that can sensitively probe the superconducting order parameter has been required.

1.1.4 Photo-induced superconductivity

Recently, light control of the superconductivity using ultrashort laser pulses has attracted a great interest to reveal the Cooper pairing in the cuprate superconductors [51]. One of the most intriguing nonequilibrium phenomena is the so-called light-induced superconductivity. The light-induced superconductivity was initially reported in the stripe-ordered $La_{1.675}Eu_{0.2}Sr_{0.125}CuO_4$ [52]. Upon photo-excitation with a mid-infrared pulse, the induced c-axis THz reflectivity change displayed a shoulder-like structure around 60 cm^{-1} as shown in Fig. 1-2(a), which resembled the equilibrium c-axis Josephson plasma resonance (JPR). Furthermore, in the imaginary part of the optical conductivity $\sigma_2(\omega)$ presented in Fig. 1-2(b), $1/\omega$-like response was identified, similar to the equilibrium response of the superconductors. These results were interpreted as evidence of the photo-induced superconductivity by melting the stripe order that competes with superconductivity.

Eventually, similar superconducting-like c-axis THz responses were identified in underdoped $YBa_2Cu_3O_{6+y}$ (YBCO) [53–56]. Since the photo-induced change in $\sigma_2(\omega)$ was the largest when the pump-frequency was tuned to the phonon-frequency of 20 THz ($\sim$ 15 μm in wavelength), it was interpreted that the nonlinear phonon excitation realized the crystal structure which is favorable for the superconductivity. However, it was pointed out that one could not distinguish the $1/\omega$-like response of the superconductivity and the Drude response of the quasiparticle excitation with a low scattering rate in the limited THz measurement frequency range [57]. As the transient $\sigma_2(\omega)$ relaxes in a few picoseconds, it cannot be studied by the resistivity or magnetic susceptibility. Therefore, a novel ultrafast probe of the superconducting order parameter has been called for.

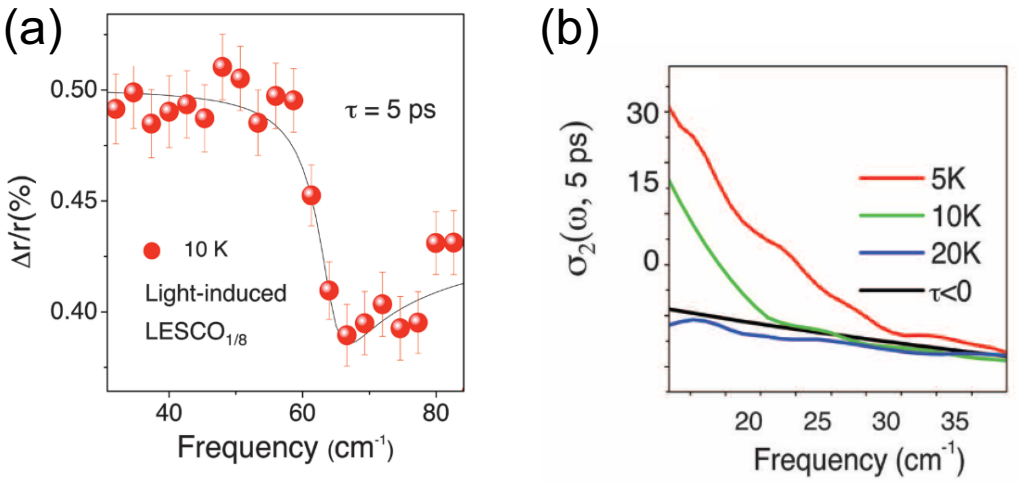

Figure 1-2: (a) Transient c-axis reflectivity change of $La_{1.675}Eu_{0.2}Sr_{0.125}CuO_4$ at 10 K with the pump wavelength of 16 μm. (b) Transient imaginary part of the optical conductivity. τ denotes the pump-probe delay time. Figures are adopted from Ref. [52].

1.2 Purpose

To explore the superconducting order parameter in cuprate superconductors in both equilibrium and nonequilibrium, we focus on the THz nonlinear responses arising from the collective excitations of the superconducting order parameter: the Higgs mode and JPR, which directly manifest the development of the superconducting order parameter within a picosecond time resolution. In this thesis, the following two main subjects are investigated.

(1) To elucidate the onset temperature of the superconducting fluctuations, we investigate the Higgs-mode response in $Bi_2Sr_2CaCu_2O_{8+x}$ thin films by THz pump-optical probe spectroscopy (TPOP).

(2) We study the photo-induced nonequilibrium state in underdoped YBCO single crystals via the THz nonlinear responses of the Higgs mode and JPR to clarify whether the light-induced superconducting-like state is actually the superconductivity or not. First, the photo-induced c-axis THz response of YBCO is studied by optical pump-THz

probe spectroscopy. Secondly, we explore the photo-induced nonequilibrium state in YBCO through the observation of the Higgs mode by THz pump-optical probe spectroscopy. Furthermore, the photo-induced nonequilibrium state in YBCO is examined by the THz third-harmonic generation associated with the JPR.

1.3 Dissertation structure

This dissertation is structured as follows:

Chapter 2 reviews the basics of the Higgs mode and JPR. The THz nonlinear responses caused by these collective excitations are also summarized.

In Chapter 3, we explain the experimental techniques, e.g., THz-pulse generation and detection methods, principles of the THz-time domain spectroscopy, and the mid-infrared pulse generation method combined with the optical parametric amplifier.

The results of the THz pump-optical probe spectroscopy in BSCCO thin films are presented in Chapter 4. The relation between the Higgs-mode response and the superconducting fluctuations in cuprate is discussed.

Chapter 5 describes the results of the optical pump-THz probe spectroscopy in a YBCO single crystal.

In Chapter 6, we report the results of the photo-induced nonequilibrium state in YBCO samples investigated by the THz-pulse-driven Higgs mode.

Chapter 7 shows the observation of the THG associated with the Josephson current in the YBCO single crystal. Besides, the results of the THG with the photo-excitation is presented. At the end of Chapter 7, we discuss the origin of the photo-induced c-axis response combining the results of Chapters 5 and 6.

Finally, our conclusions and the outlook for the relevant studies are summarized in Chapter 8.

Chapter 2

Background

In this chapter, we describe the two types of collective excitations of the superconducting order parameter: the Higgs mode and Josephson plasma resonance (JPR). We also review the nonlinear terahertz (THz) optical responses arising from these collective excitations.

2.1 Higgs mode in superconductors

2.1.1 Collective modes in a symmetry broken system

Phase transitions can be described in terms of a spontaneous symmetry breaking and a concomitant order parameter. When continuous symmetry is spontaneously broken, two types of collective modes generally emerge: amplitude and phase fluctuations of the order parameter, which are schematically depicted in Fig. 2-1(a). In general, the amplitude mode is massive, whereas the phase mode, which is also referred to as Nambu-Goldstone (NG) mode, is massless [58–62]. This is because the potential curvature as a function of the complex order parameter Ψ along the radial direction is finite while that along the azimuthal direction is zero, as shown in Fig. 2-1(a).

In the case of superconductors, where the order parameter couples to the gauge field, the amplitude mode is special compared to the other symmetry-broken systems. The massless phase mode is screened by long-range Coulomb interactions and is lifted up to the plasma frequency ω_p due to the Anderson-Higgs mechanism as schematically illustrated in Fig. 2-1(b) [59–61, 63–65].

The Ginzburg-Landau (GL) theory offers a simple description of the cou-

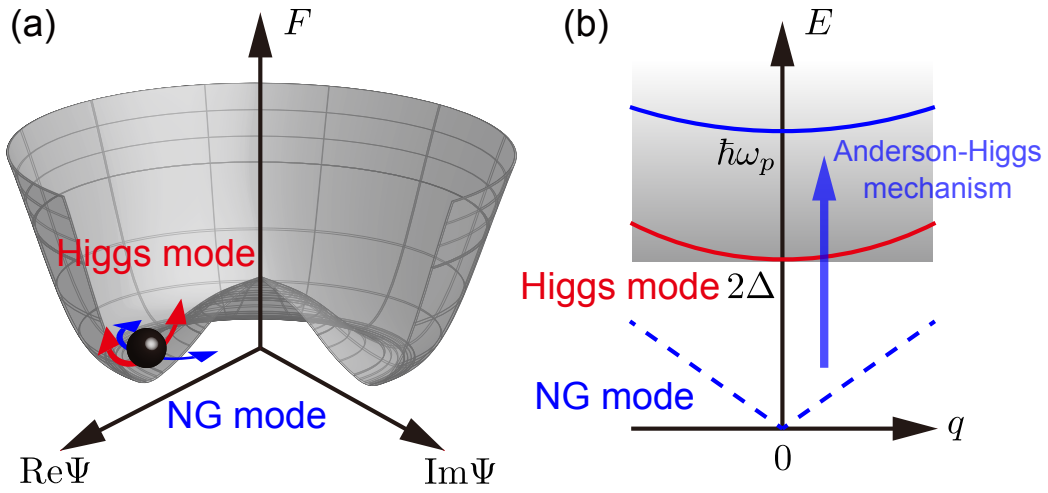

Figure 2-1: (a) A schematic illustration of the Higgs mode (red arrow) and NG mode (blue arrow) represented by the GL free energy potential as a function of complex order parameter Ψ. (b) A schematic picture of the energy of the two collective modes and a quasiparticle excitation in a superconductor with the Anderson-Higgs mechanism.

pling between the Higgs mode and gauge field. Based on the GL theory, the free energy density of the system under the presence of the vector potential $\mathbf{A}(\mathbf{r})$ can be generally expanded in terms of the complex order parameter $\Psi(\mathbf{r})$ [66, 67] as

$$f(\mathbf{r}) = f_0 + a|\Psi(\mathbf{r})|^2 + \frac{b}{2}|\Psi(\mathbf{r})|^4 + \frac{1}{2m^*}|(-i\hbar\nabla - e^*\mathbf{A}(\mathbf{r}))\Psi(\mathbf{r})|^2, \qquad (2\text{-}1)$$

where $a = a_0(T - T_c)$ ($a_0 > 0$), a_0 and b are some constants ($b > 0$), e^* and m^* are the effective charge and mass of the Cooper pair. At temperatures $T > T_c$, $f(\mathbf{r})$ is minimum when $\Psi(\mathbf{r}) = 0$. However, at $T < T_c$, $f(\mathbf{r})$ as a function of $\Psi(\mathbf{r})$ shows a shape of a Mexican hat as displayed in Fig. 2-1(a). Ψ takes a finite value at the minimum of the free energy density $f(\mathbf{r})$. After the phase transition, the phase of $\Psi(\mathbf{r})$ is fixed at a specific point, which means that the phase rotational symmetry is spontaneously broken in the superconducting state.

The order parameter can be expanded around the ground state Ψ_0 in

terms of its amplitude and phase fluctuations as

$$\Psi(\mathbf{r}) = [\Psi_0 + H(\mathbf{r})]e^{i\theta(\mathbf{r})}, \tag{2-2}$$

where $H(\mathbf{r})$ is the amplitude fluctuation, and $\theta(\mathbf{r})$ is the phase fluctuation. Then $f(\mathbf{r})$ can be expanded to the second-order of the fluctuation as

$$f(\mathbf{r}) = -2aH(\mathbf{r})^2 + \frac{1}{2m^*}\nabla(H(\mathbf{r}))^2 + \frac{e^{*2}}{2m^*}\left[\mathbf{A}(\mathbf{r}) - \frac{1}{e^*}\nabla\theta(\mathbf{r})\right]^2. \tag{2-3}$$

Under the unitary gauge transformation $\mathbf{A}(\mathbf{r}) \rightarrow \mathbf{A}(\mathbf{r}) + \nabla\theta(\mathbf{r})/e^*$, we can eliminate $\theta(\mathbf{r})$ in Eq. (2-3) as

$$f(\mathbf{r}) = -2aH(\mathbf{r})^2 + \frac{1}{2m^*}\nabla(H(\mathbf{r}))^2 + \frac{e^{*2}\Psi_0^2}{2m^*}\mathbf{A}(\mathbf{r})^2 + \frac{e^{*2}\Psi_0}{m^*}\mathbf{A}(\mathbf{r})^2 H(\mathbf{r}). \tag{2-4}$$

The third term indicates that the electromagnetic field acquires mass $\sqrt{e^{*2}\Psi_0^2/2m^*}$ via the Anderson-Higgs mechanism. Equation (2-4) also shows that the Higgs mode does not couple to the electromagnetic field in the linear response regime. However, in Eq.(2-4) there is a term $\mathbf{A}(\mathbf{r})^2 H(\mathbf{r})$ which corresponds to the second-order coupling between the Higgs mode and the electromagnetic wave. This nonlinear coupling plays a crucial role to observe the Higgs mode as explained in the next subsection.

Unlike the nonlinear coupling between the Higgs mode and the electromagnetic wave, the Higgs mode has been anticipated to appear in the nonadiabatic excitation condition [68–73]. The nonadiabatic excitation condition requires that the order parameter changes faster than the response time of the BCS state $\sim \hbar/\Delta$. In addition, the photon energy of the excitation pulse should be close to 2Δ to avoid the excess heating of the system, which results in the destruction of the superconducting condensate. These conditions are satisfied when a single-cycle short THz pulse is employed, whose photon energy is close to 2Δ. In the following, the experimental observations of the Higgs mode are reviewed.

2.1.2 Higgs mode in conventional superconductors

The experimental difficulty in observing the Higgs mode in superconductors is that the Higgs mode does not couple to electromagnetic fields in the linear-response regime because it does not have any electric charge nor dipole.

While some exceptions are reported in the dichalcogenide compounds that exhibit the charge-density wave (CDW) and superconductivity [74–79], for decades, it has been considered that the Higgs mode cannot be detected by light.

However, with the recent advances of intense THz-pulse generation techniques [80, 81], it has become possible to observe the Higgs mode by ultrafast pump-probe spectroscopy and THz third-harmonic generation (THG) [66,67,82–87]. The observation of the Higgs mode has been first demonstrated in an s-wave superconductor NbN by THz pump-THz probe spectroscopy as shown in Fig. 2-2(a) [82]. After the excitation with a single-cycle THz-pulse, the oscillation of the order parameter is identified. Here, the role of the THz pump-pulse is to excite the quasiparticles instantaneously at the gap edge without giving excess energy to the system. The superconducting gap 2Δ is self-consistently determined by the BCS gap equation:

$$\Delta = V \sum_{\mathbf{k}} \frac{\Delta}{2E_{\mathbf{k}}}[1 - 2f(E_{\mathbf{k}})], \tag{2-5}$$

where V is the pairing interaction, $E_{\mathbf{k}} = \sqrt{\epsilon_{\mathbf{k}}^2 + \Delta^2}$, $\epsilon_{\mathbf{k}}$ is the band dispersion measured from Fermi energy, and $f(E_{\mathbf{k}})$ is the Fermi distribution function. The instantaneous injection of the quasiparticles by the THz pulse changes the Fermi function, resulting in a nonadiabatic quench of 2Δ through Eq. (2-5), and a free oscillation of the Higgs mode.

It has been further demonstrated that the Higgs mode couples nonlinearly to the THz electromagnetic field [83]. Using a multi-cycle THz pulse, the oscillation of the superconducting order parameter which follows the squared THz electric field (E-field) has been observed as shown in Fig. 2-2(b). Besides, the THz THG mediated by this nonlinear coupling has also been identified [83]. The temperature dependence of the THG intensity displays a resonance when the incident THz frequency ω satisfies the relation $2\omega = 2\Delta$, which is successfully explained by the Anderson pseudospin model [88].

Subsequently, it has been theoretically pointed out that not only the Higgs mode but also the charge density fluctuation (CDF), i.e., the quasiparticle excitation contribute to the THG [89]. The important point is that the Higgs mode does not depend on the polarization of the THz pulse, while the CDF strongly depends on it. The polarization-resolved measurement has shown that THG does not depend on the polarization of the incident THz pulse, indicating that the THG is attributed to the Higgs mode [66].

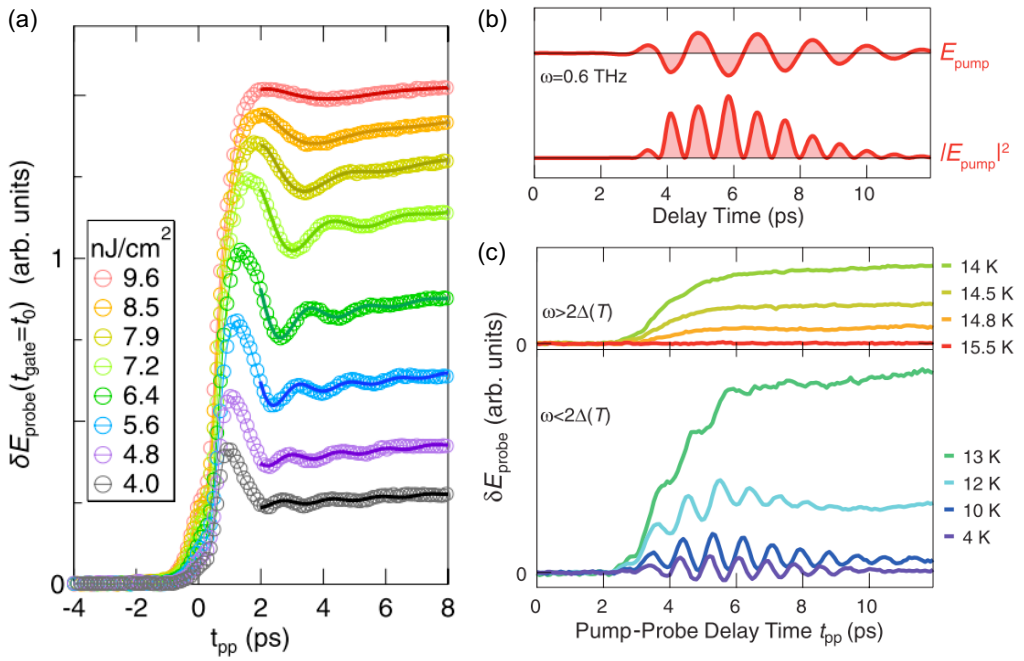

Figure 2-2: (a) Single-cycle THz pump-induced change in the THz probe-induced E-field below T_c [82]. (b) The waveform of the narrow band THz E-field whose frequency is at 0.6 THz and that of its squared E-field. (c) Narrow band THz pump-induced change in the THz probe-induced E-field below T_c. Figures (b) and (c) are adopted from [83].

In parallel, substantial theoretical progress has been made to understand the observability of the Higgs mode in the nonlinear THz optical responses [67,88–96]. It has been recently shown that the paramagnetic coupling of the light-matter interaction plays a crucial role in the Higgs-mode contribution to the nonlinear THz optical responses [93, 96].

2.1.3 Higg mode in cuprate superconductors

More recently, we have observed the Higgs mode in the d-wave cuprate superconductor $Bi_2Sr_2CaCu_2O_{8+x}$ (BSCCO) by THz pump-optical probe (TPOP) spectroscopy in the reflection geometry (my master course study) [85]. As shown in Fig. 2-3(a), the THz pump-induced reflectivity change $\Delta R/R$ displays oscillatory behavior that follows the squared pump THz E-field, which

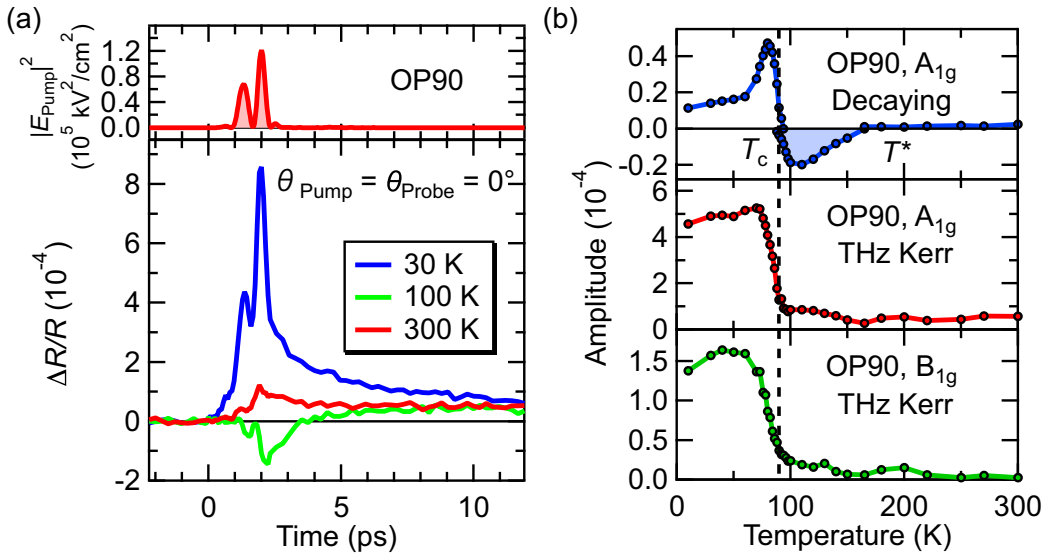

Figure 2-3: (a) THz pump-induced reflectivity change for optimally doped $Bi_2Sr_2CaCu_2O_{8+x}$ (T_c = 90 K) at selected temperatures. (b) Temperature dependencies of the A_{1g} decaying component (blue), the A_{1g} THz Kerr component (red), and the B_{1g} THz Kerr component (green). Figures are adopted from [85].

is referred to as the THz Kerr effect: the intense THz pump pulse modifies the optical response of the near-infrared probe pulse. The polarization-resolved measurements revel that $\Delta R/R$ is decomposed into the polarization independent A_{1g} component and polarization dependent B_{1g} component. Both the A_{1g} and B_{1g} THz Kerr components of $\Delta R/R$ increase below T_c as plotted in Fig. 2-3(b), indicating their relevance to the superconductivity. It should be noted that the A_{1g} and B_{1g} THz Kerr components show decreasing trends approximately below 70 K and 40 K, respectively. These are because the THz electric field which penetrates into the sample decreases as the temperature is lowered. This effect is considered in this study, as we will describe in Chapter 4. In addition, since the A_{1g} decaying component switches its sign at T_c and T^* [97], the positive decaying component below T_c and negative decaying component above T_c are ascribed to the incoherent quasiparticle excitation in the superconducting and pseudogap state, respectively. Mean-field calculations demonstrate that the A_{1g} THz Kerr component is attributed to the Higgs mode of the d-wave superconducting order parameter, whereas the B_{1g}

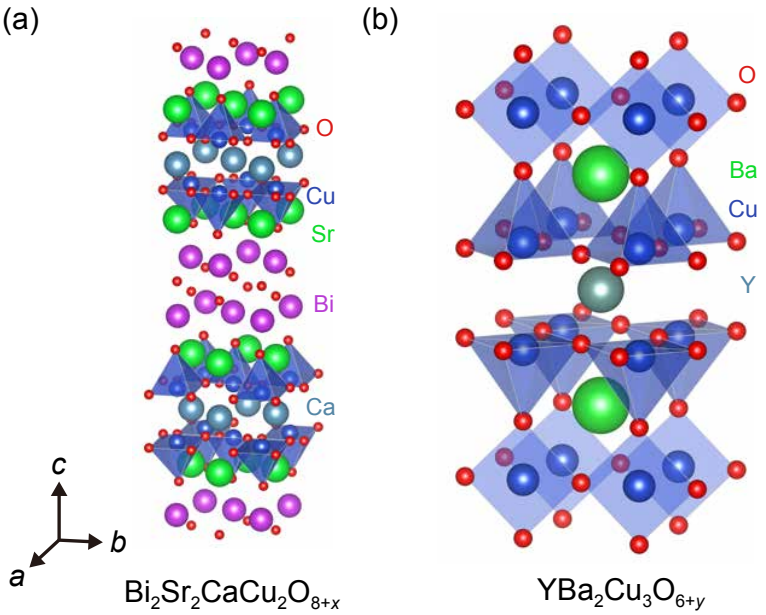

Figure 2-4: Crystal structures of (a) $Bi_2Sr_2CaCu_2O_{8+x}$ and (b) $YBa_2Cu_3O_{6+y}$ drawn by VESTA [98].

THz Kerr component most likely originates from the CDF [85].

Subsequently, THG from cuprate superconductors has been reported in other cuprate superconductors such as LSCO, $YBa_2Cu_3O_{6+y}$ (YBCO) and $DyBa_2Cu_3O_{7-x}$ and interpreted in terms of Higgs mode-mediated THG [87].

2.2 Josephson plasma resonance (JPR)

2.2.1 General optical response above T_c

Figures 2-4(a) and (b) illustrate the crystal structures of BSCCO and YBCO, respectively, which are investigated in this study. Cuprate superconductors have a layered perovskite structure that is consisted of alternating conducting CuO_2 planes (ab-plane) and insulating blocking layers along the c-axis. The insulating layers provide charge carriers to the CuO_2 layers.

The electronic anisotropy between the ab-plane and c-axis of the cuprate is discerned in the optical responses. Figure 2-5 shows the room-temperature reflectivity of BSCCO [99]. While the b-axis reflectivity shows a Drude-

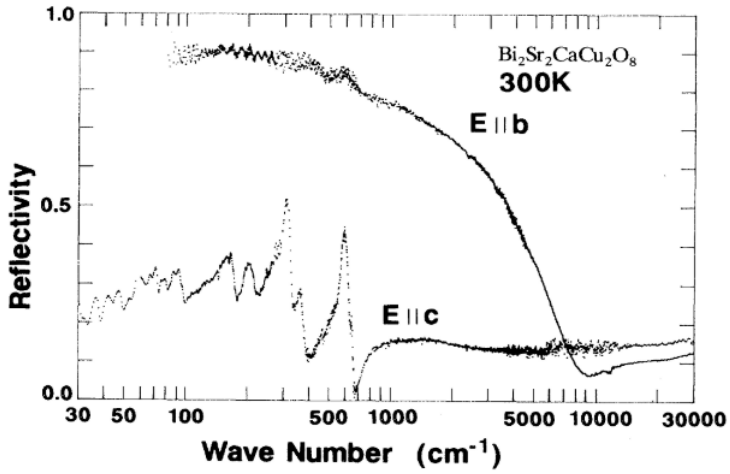

Figure 2-5: Reflectivity of $Bi_2Sr_2CaCu_2O_8$ at room temperature for the b-axis and the c-axis [99].

like metallic behavior, the c-axis reflectivity is insulator-like and very low. Also, the c-axis reflectivity is governed by various phonons in the far-infrared region. It should be noted that the normal state optical spectrum of cuprate superconductors for a wide frequency range cannot be described by the simple Drude model, and has been intensively studied [100].

2.2.2 c-axis linear optical response below T_c

While the charge carrier dynamics along the c-axis is incoherent above T_c, Cooper pairs can tunnel along the c-axis when the superconductivity sets in due to the Josephson effect. As a consequence, a sharp plasma edge structure appears in the c-axis reflectivity spectrum below T_c. This plasma mode is referred to as the Josephson plasma resonance (JPR), and corresponds to the collective excitation of the superconducting phase along the c-axis..

In the simple case of the single layer cuprate such as $La_{2-x}Sr_xCuO_4$, the dielectric function can be well described by the two-fluid model [102]:

$$\varepsilon(\omega) = \varepsilon_b \left(1 - \frac{\omega_n^2}{\omega^2 + i\gamma\omega} - \frac{\omega_s^2}{\omega^2}\right), \tag{2-6}$$

where ω_n and ω_s are the plasma frequency of the Drude and superconducting components, respectively, and γ is the scattering rate of the Drude com-

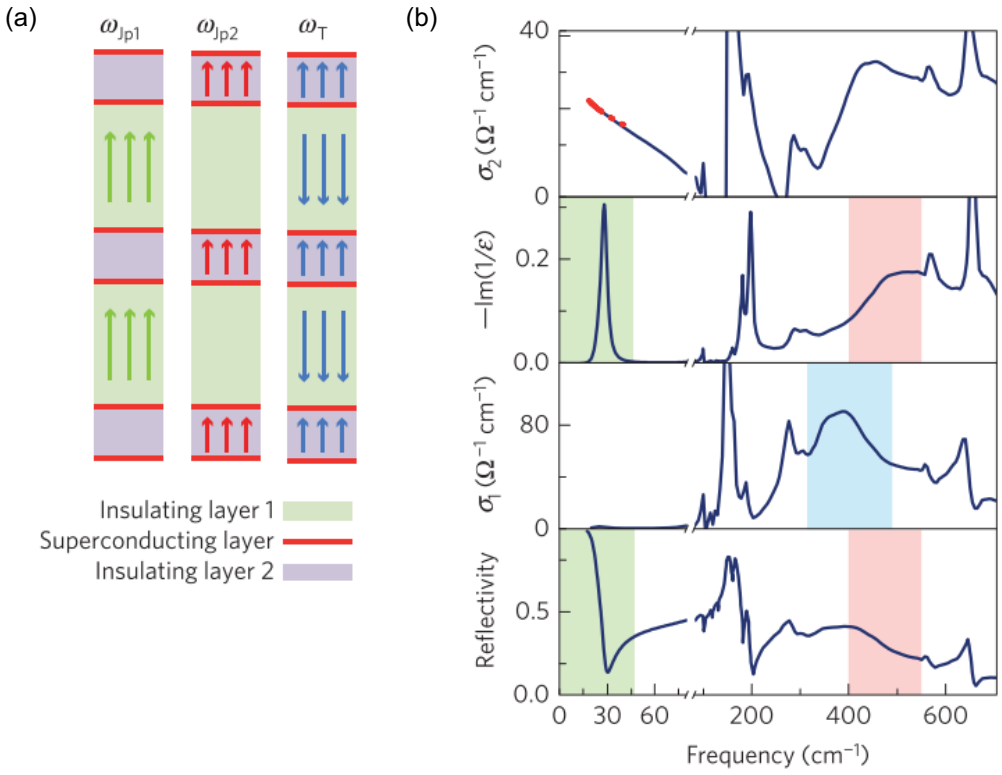

Figure 2-6: (a) Schematic of the plasma modes of two inequivalent Josephson junctions below T_c. Two longitudinal modes (ω_{JP1} and ω_{JP2}) and a transverse mode ω_T are illustrated. (b) The equilibrium c-axis optical properties for underdoped YBCO ($T_c = 50$ K) [53, 101]. The data for low-frequency below ~ 80 cm^{-1} are reported in Ref. [101] and those for high-frequency above ~ 300 cm^{-1} are reported in Ref. [53]. Figures are adopted from Ref. [53].

ponent. ε_b is the background dielectric constant and $\varepsilon_b = 4.5$ in cuprate superconductors [103].

In the case of bilayer cuprates such as YBCO and BSCCO (Bi2212), there are two inequivalent Josephson junctions as schematically shown in Fig. 2-6(a). Usually, the thicker one is called "inter-bilayer" [the insulating layer 1 in Fig. 2-6(a)] and the thinner one [the insulating layer 2 in Fig. 2-6(a)] is called "intra-bilayer". For two junctions 1 and 2, the dielectric function is written as [104]

$$\frac{\varepsilon(\omega)}{\varepsilon_b} = \frac{(\omega^2 - \omega_{\mathrm{JP1}}^2)(\omega^2 - \omega_{\mathrm{JP2}}^2)}{\omega^2(\omega^2 - \omega_{\mathrm{T}}^2)}. \tag{2-7}$$

Here, the Drude term is neglected for clarity. ω_{JP1} and ω_{JP2} are the plasma frequency of the superconducting components in the junctions 1 and 2. ω_{T} is the plasma frequency of the transverse mode which satisfies

$$\omega_{\mathrm{T}}^2 = \frac{d_2\omega_{\mathrm{JP1}}^2 + d_1\omega_{\mathrm{JP2}}^2}{d_1 + d_2}, \tag{2-8}$$

where d_1 and d_2 are the thickness of the junctions 1 and 2, respectively.

Figure 2-6(b) displays the c-axis optical constants of underdoped YBCO below T_{c}. Two longitudinal JPRs appear as two peaks in the loss function $-\mathrm{Im}(1/\varepsilon(\omega))$ and two plasma edges on the reflectivity around 30 cm^{-1} [the green shaded area in the bottom panel in Fig. 2-6(b)] and 475 cm^{-1} [the red shaded area in the bottom panel in Fig. 2-6(b)]. Besides, the transverse mode is identified as a broad peak around 400 cm^{-1} in the real part of the optical conductivity $\sigma_1(\omega)$ (blue shaded area).

2.2.3 c-axis nonlinear optical response below T_{c}: THz third-harmonic generation (THG)

As mentioned before, cuprate superconductors consist of the stack of the Cu-O layer and insulating layer along the c-axis. In the superconducting state, the Cooper pairs in each Cu-O layer can tunnel along the c-axis (Josephson effect). The Josephson supercurrent $I(t)$ is determined by the phase difference between two adjacent superconducting layers $\theta(t)$, and they satisfy the Josephson relations [105]:

$$\frac{\partial\theta(t)}{\partial t} = \frac{2ed}{\hbar}E(t), \tag{2-9}$$

$$I(t) = I_c \sin\theta(t), \tag{2-10}$$

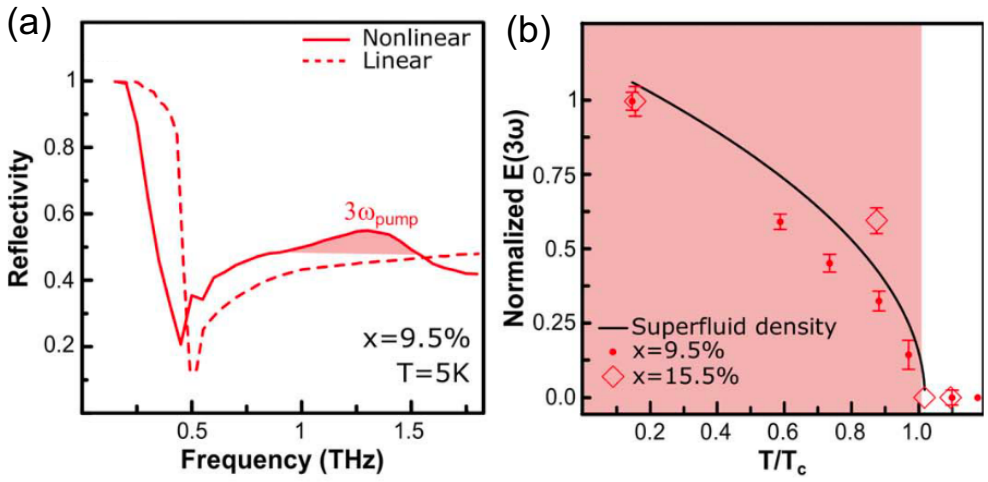

Figure 2-7: (a)Reflectivity spectrum of LBCO ($x = 9.5\%$) at 5 K below T_c. (b) Temperature dependence of the THG intensity. Figures are adopted from [106].

where d is the distance between two superconducting layers, $2e$ is the Cooper pair charge, and I_c is the critical current. Assuming an incident THz E-field of $E(t) = E_0 \sin(\omega_{\mathrm{THz}} t)$ polarized along the c-axis, the time-dependent phase follows $\theta(t) \propto \theta_0 \cos(\omega_{\mathrm{THz}} t)$, where $\theta_0 = 2edE_0/\hbar\omega_{\mathrm{THz}}$. Using Eq. (2-10), the THz pulse-induced current along the c-axis is written as

$$\begin{aligned} I(t) &= I_c \sin\theta(t) = I_c \sin\theta_0 \cos(\omega_{\mathrm{THz}} t) \\ &\simeq I_c \left[\theta_0 \cos(\omega_{\mathrm{THz}} t) - \frac{\theta_0^3}{6} \cos^3(\omega_{\mathrm{THz}} t) \right]. \end{aligned} \tag{2-11}$$

The second term in Eq. (2-11) generates the third-harmonics of the incident THz pulse.

The THG associated with the Josephson current has been recently observed in $La_{2-x}Ba_xCuO_4$ (LBCO) [106]. As shown in Fig. 2-7(a), the THG is observed in the THz reflectivity spectrum with an intense THz pulse, which is absent in the equilibrium reflectivity. The temperature dependence of the THG intensity follows that of the superfluid density as shown in Fig. 2-7(b), because the critical current I_c is proportional to the superfluid density. Therefore, the THG mediated by the Josephson current serves as a probe of the c-axis superconducting phase coherence.

Chapter 3

Experimental techniques

In this chapter, the basic principles of the experiments are briefly reviewed. First, the intense terahertz (THz) pulse generation and the THz pulse detection are explained. Second, the THz time-domain spectroscopy (THz-TDS) is introduced. Finally, we explain the wavelength conversion technique for near-infrared (NIR) and mid-infrared (MIR) pulses.

3.1 THz pulse generation and detection

3.1.1 THz pulse generation

Optical rectification

For the THz-pulse generation, the optical rectification method has been employed, which is the second-order nonlinear optical process [34, 107]. When a pulse laser is irradiated to nonlinear crystals (NCs) such as ZnTe, InAs, or $LiNbO_3$, the nonlinear polarization $\mathbf{P}^{(2)}(t)$ is induced, which can be expressed as

$$P_i^{(2)}(t) = \sum_{jk} \chi_{ijk}^{(2)} E_j(t) E_k(t), \tag{3-1}$$

where i denotes the x, y, z components of the induced nonlinear polarization, j and k denote those of the incoming electric field (E-field) $E(t)$ and $\chi_{ijk}^{(2)}$ is the second-order nonlinear susceptibility of the NC. This second-order nonlinear polarization $\mathbf{P}^{(2)}(t)$ radiates the E-field which is given by

$$\mathbf{E}_{\mathrm{rad}}(t) \propto \frac{\partial^2}{\partial t^2} \mathbf{P}^{(2)}(t). \tag{3-2}$$

Since $\mathbf{P}^{(2)}(t)$ varies in the time scale of the optical pulse width, the emitted E-field oscillates in the same time scale, whose frequency is located at THz range when the optical pulse width is around 100 fs.

Tilted pulse front technique for an intense THz pulse generation

To generate an intense THz pulse enough to access the nonlinear optical process in solids, $LiNbO_3$ is a promising candidate because it is known to have a larger nonlinear optical coefficient for optical rectification of 168 pm/V compared to that of GaP (24.8 pm/V) or ZnTe (68.5 pm/V) [108]. However, the mismatch between the group velocity of the optical pulse $v_{\mathrm{opt}}^{\mathrm{gr}}$ and the phase velocity of the THz pulse v_{THz} inside $LiNbO_3$ never satisfies the phase-matching condition which is expressed as

$$v_{\mathrm{opt}}^{\mathrm{gr}} = v_{\mathrm{THz}}, \tag{3-3}$$

making it difficult to generate an intense THz pulse in the collinear configuration. To circumvent this difficulty, the tilted pulse front technique was proposed [80]. In the noncollinear configuration by tilting the optical pulse front, the phase-matching condition of Eq. (3-3) is modified as

$$\cos\gamma = \frac{v_{\mathrm{THz}}}{v_{\mathrm{opt}}^{\mathrm{gr}}} = \frac{n_{\mathrm{opt}}^{\mathrm{gr}}}{n_{\mathrm{THz}}}, \tag{3-4}$$

where γ is the angle between the propagation directions of the optical and THz pulses as defined in Fig. 3-1. Since $n_{\mathrm{THz}} = 5.16$ and $n_{\mathrm{opt}}^{\mathrm{gr}} = 2.23$ for $LiNbO_3$ [108], Eq. (3-4) is satisfied when $\gamma = 63°$.

We combined a grating and two cylindrical lenses to tilt the optical pulse front by the angle γ, as shown in Fig. 3-1 [109]. In this configuration, the angle γ can be described as

$$\tan\gamma = \frac{m\lambda_{\mathrm{opt}}p}{n_{\mathrm{opt}}^{\mathrm{gr}}\beta_1\cos\theta_d}. \tag{3-5}$$

Here m, θ_d, and p are the diffraction order, the diffraction angle, and the groove density of the grating, respectively. λ_{opt} is the central wavelength of the pump pulse, and β_1 is the horizontal magnification factor of the cylindrical lens for the pump pulse front. To obtain the optimal THz beam characteristics and THz conversion efficiency, the tilt angle of the grating image

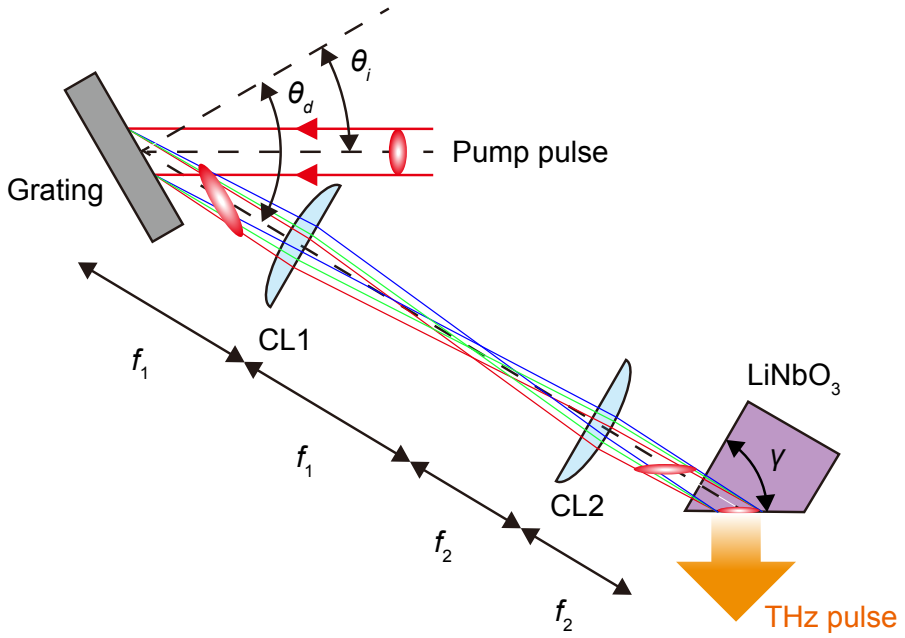

Figure 3-1: Configuration for the intense THz pulse generation from $LiNbO_3$ crystal employing the tilted pulse front technique. CL denotes a cylindrical lens.

inside the $LiNbO_3$ crystal θ should be equal to γ. The tilt angle θ is thus given by

$$\tan\theta = \tan\gamma = n_{\text{opt}}\beta_2 \tan\theta_d, \tag{3-6}$$

where n_{opt} is the refractive index of the $LiNbO_3$ for the optical pulse and β_2 is the horizontal magnification factor of the cylindrical lens for the grating image.

In this study, the first-order diffraction of the pump pulse ($m = 1$) is used for the wavelength $\lambda_{\text{opt}} = 800$ nm. The refractive index of $LiNbO_3$ at 800 nm is $n_{\text{opt}} = 2.16$ [108]. The groove density of the grating is $p = 1800$ mm^{-1} and the focal lengths of the lenses are $f_1 = 250$ mm and $f_2 = 150$ mm. This means that $\beta_1 = \beta_2 = f_2/f_1 = 0.6$. To satisfy both Eq. (3-5) and Eq. (3-6), we used $\theta_d = 56.1°$. The incident angle to the grating θ_i is estimated to be $\theta_i = 37.6°$ through the following relation:

$$\sin\theta_i + \sin\theta_d = \lambda_{\text{opt}} p. \tag{3-7}$$

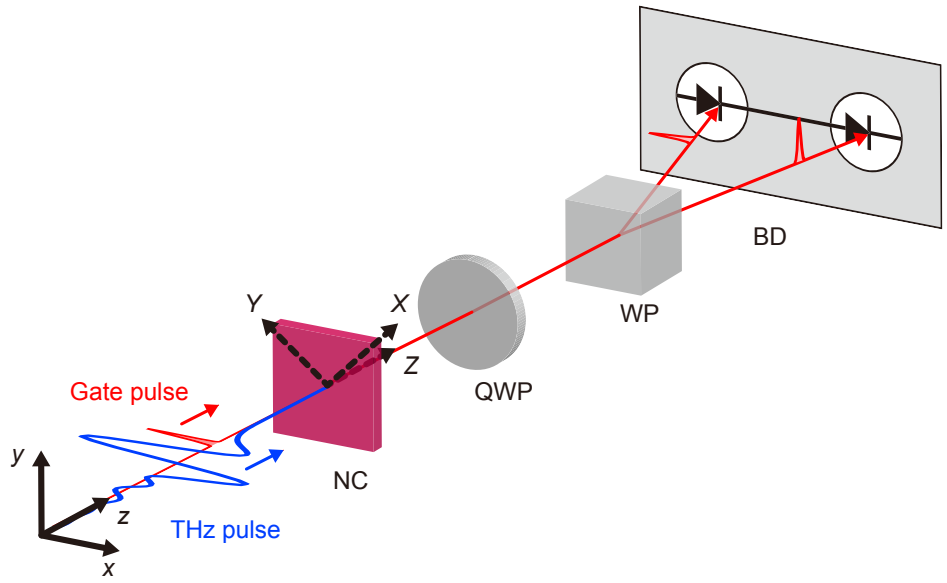

Figure 3-2: Configuration for the THz pulse-detection using EO sampling method. NC, QWP, WP, and BD denote a nonlinear crystal, quarter-wave plate, a Wollaston prism, and a balanced detector, respectively.

3.1.2 THz pulse detection

A THz E-field can be measured using an electro-optical (EO) sampling method based on the Pockels effect [110]. The Pockels effect is a second-order nonlinear optical effect where the refractive index of the NC is modulated in proportion to the incident THz E-field. Thus, the THz E-field can be determined by measuring the field-induced birefringence, which results in the polarization-rotation of the optical pulse, often referred to as the gate pulse. In this study, (110) oriented GaP or ZnTe crystals are used as a NC for the THz pulse-detection. The principle of the EO sampling method is given in Ref. [111] in detail, and the brief explanation is presented in the following.

A configuration of the THz pulse-detection is schematically shown in Fig. 3-2. Here the (x, y, z) coordinate system is defined as the principal-axis of the NC where the z-direction is parallel to the [110] direction of the NC. In this case, the field-induced birefringence is maximized when the THz and gate E-fields are parallel to the $[1\bar{1}0]$ direction of a (110) oriented NC. Using the (X, Y, Z) coordinate system, which is rotated 45° from the (x, y, z) coordinate

system around z-axis as shown in Fig. 3-2, the THz and gate E-fields can be expressed as

$$\mathbf{E}_{\mathrm{THz}} = \frac{E_{\mathrm{THz}}}{\sqrt{2}} \begin{pmatrix} 1 \\ -1 \\ 0 \end{pmatrix}, \ \mathbf{E_0} = \frac{E_0}{\sqrt{2}} \begin{pmatrix} 1 \\ -1 \\ 0 \end{pmatrix}. \tag{3-8}$$

In the (X, Y, Z) coordinate system, the refractive index of a NC with a THz E-field E_{THz} can be described up to first-order in E_{THz} as

$$n_X = n_0 - \frac{1}{2} n_0^3 r_{41} E_{\mathrm{THz}} \equiv n_0 - \Delta n, \tag{3-9}$$

$$n_Y = n_0 + \frac{1}{2} n_0^3 r_{41} E_{\mathrm{THz}} \equiv n_0 + \Delta n, \tag{3-10}$$

where n_0 is the refractive index of NC at the frequency of the gate pulse (ω_0) without the THz pulse, r_{41} is the EO coefficient of the NC and $\Delta n = n_0^3 r_{41} E_{\mathrm{THz}}$. As a result, the linear polarization of the gate pulse evolves into an elliptical polarization after propagating through the NC with the THz pulse. The gate E-field after propagating through the NC ($\mathbf{E}_{\mathrm{NC}}$) is given by

$$\mathbf{E}_{\mathrm{NC}} = \frac{E_0}{\sqrt{2}} e^{i n_0 \omega_0 d/c} \begin{pmatrix} e^{-i\Delta n \omega_0 d/c} \\ -e^{i\Delta n \omega_0 d/c} \\ 0 \end{pmatrix}. \tag{3-11}$$

Here, c is the speed of light, and d is the thickness of the NC. The gate pulse further propagates through the quarter-wave plate (QWP), whose fast axis is parallel to X-axis (or Y-axis). Thus, the gate E-field evolves into

$$\mathbf{E}_{\mathrm{QWP}} = \frac{E_0}{\sqrt{2}} e^{i n_0 \omega_0 d/c} \begin{pmatrix} e^{i(-\Delta n \omega_0 d/c + \pi/4)} \\ -e^{i(\Delta n \omega_0 d/c - \pi/4)} \\ 0 \end{pmatrix}. \tag{3-12}$$

In the (x, y, z) coordinate system, Eq. (3-12) can be represented as

$$\mathbf{E}^{xyz}_{\mathrm{QWP}} = \frac{E_0}{\sqrt{2}} e^{i n_0 \omega_0 d/c} \begin{pmatrix} -i(1 + \sin(\Delta n \omega_0 d/c)) \\ 1 - \sin(\Delta n \omega_0 d/c) \\ 0 \end{pmatrix} \tag{3-13}$$

$$\simeq \frac{E_0}{\sqrt{2}} e^{i n_0 \omega_0 d/c} \begin{pmatrix} -i(1 + \Delta\phi/2) \\ 1 - \Delta\phi/2 \\ 0 \end{pmatrix}, \tag{3-14}$$

where $\Delta\phi = 2\Delta n\omega_0 d/c$ is assumed to be small ($\Delta\phi \ll 1$). The intensities of the two gate beams separated by the Wollaston prism are

$$I_x = \frac{I_0}{2}(1 + \Delta\phi/2)^2 \simeq \frac{I_0}{2}(1 + \Delta\phi), \tag{3-15}$$

$$I_y = \frac{I_0}{2}(1 - \Delta\phi/2)^2 \simeq \frac{I_0}{2}(1 - \Delta\phi). \tag{3-16}$$

Here, $I_0 = \varepsilon_0 E_0^2$, and ε_0 is the dielectric constant of vacuum. Finally, the signal of the balanced detector ΔI can be expressed by

$$\Delta I = I_x - I_y = I_0\Delta\phi = I_0\frac{\omega_0 d n_0^3 r_{41}}{c}E_{\mathrm{THz}} = I_0\frac{2\pi d n_0^3 r_{41}}{\lambda_0}E_{\mathrm{THz}}, \tag{3-17}$$

where λ_0 is the wavelength of the gate pulse. Therefore, the THz E-field can be determined from ΔI as

$$E_{\mathrm{THz}} = \frac{\lambda_0}{2\pi d n_0^3 r_{41}}\frac{\Delta I}{I_0}. \tag{3-18}$$

The temporal waveform of the THz E-field can be obtained by measuring the THz E-field with changing the delay time between the THz pulse and the gate pulse.

3.2 THz time-domain spectroscopy (THz-TDS)

3.2.1 Experimental setup for THz-TDS

Figure 3-3(a) depicts the setup for the THz-TDS measurement in transmission geometry. The output from the Ti:sapphire mode-locked laser (Coherent Vitesse, the central wavelength of 800 nm, pulse duration of 100 fs, and repetition rate of 80 MHz) is divided into two beams: one for the THz-pulse generation using an InAs crystal in reflection geometry and the other for the EO sampling in a ZnTe crystal. The obtained waveform and the power spectrum of the THz E-field without a sample are displayed in Fig. 3-3(b) and (c), respectively.

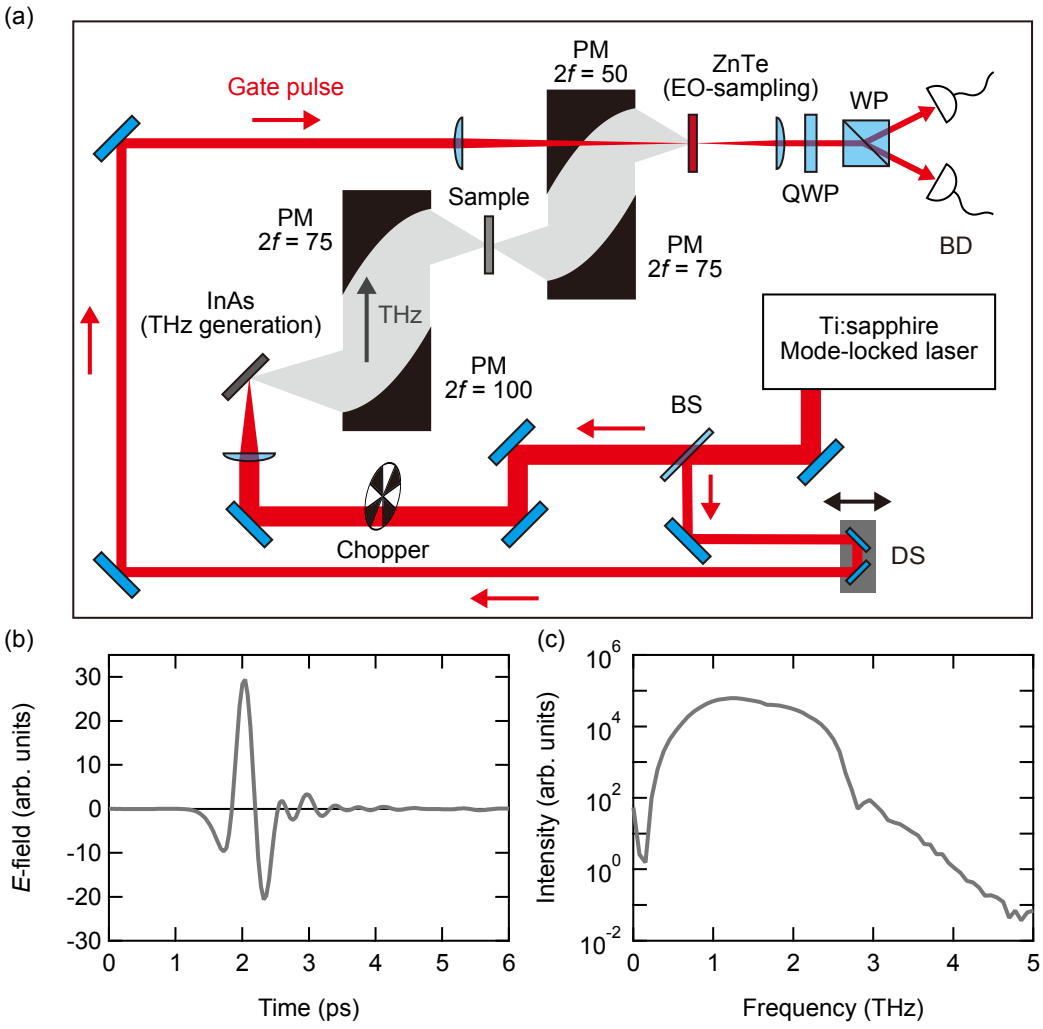

Figure 3-3: (a) Schematic representation of the THz-TDS setup in transmission geometry. BD, QWP, BS, PM, and DS are a balanced detector, quarter-wave plate, beam splitter, parabolic mirror, and delay stage, respectively. (b), (c) The waveform and the power spectrum of the THz E-field measured at the ZnTe position, respectively.

3.2.2 Determination of optical constants in THz-TDS

Using the fast Fourier transform (FFT) of the waveform of the THz E-field, the complex refractive index of a material in the frequency domain can be determined in THz-TDS. Here, the procedure to determine the complex optical constants is described in the cases of transmission geometry for thin film samples and reflection geometry for bulk samples.

Transmission geometry

First, the refractive index of a thick film sample can be determined as follows. The situation is schematically depicted in Fig. 3-4(a). The transmitted THz E-field after the sample $E_{\mathrm{out}}(\omega)$ is written in the frequency domain as

$$E_{\mathrm{out}}(\omega) = E_{\mathrm{in}}(\omega)\ \frac{4n(\omega)}{(n(\omega)+1)^2}\ e^{in(\omega)d\omega/c}. \tag{3-19}$$

Here, $E_{\mathrm{in}}(\omega)$ is the incident THz E-field, and $n(\omega)$ and d are the complex refractive index and the thickness of the sample, respectively. On the other hand, the THz E-field without the sample $E_{\mathrm{blank}}(\omega)$ is expressed as

$$E_{\mathrm{blank}}(\omega) = E_{\mathrm{in}}(\omega)\ e^{id\omega/c}. \tag{3-20}$$

Using $E_{\mathrm{out}}(\omega)$ and $E_{\mathrm{blank}}(\omega)$, the complex transmittance is given by

$$t(\omega) = \frac{E_{\mathrm{out}}(\omega)}{E_{\mathrm{blank}}(\omega)} = \frac{4n(\omega)}{(n(\omega)+1)^2}\ e^{i(n(\omega)-1)d\omega/c}. \tag{3-21}$$

The complex refractive index $n(\omega)$ can be obtained by numerically solving Eq. (3-21) in terms of $n(\omega)$ for each ω.

Next, a thin film sample on a thick substrate is assumed as depicted in Fig. 3-4(b). In this case, the multiple reflections of the THz E-field inside the film should be considered as depicted in Fig. 3-4(c), and the THz E-field inside the thin film $E_{\mathrm{film}}(\omega)$ can be represented as

$$\begin{aligned} E_{\mathrm{film}}(\omega) &= E_{\mathrm{in}}(\omega)\frac{2e^{in_f(\omega)d_f\omega/c}}{1+n_f(\omega)}\sum_{j=0}^{\infty}\left(\frac{n_f(\omega)-n_s(\omega)}{n_f(\omega)+n_s(\omega)}\frac{n_f(\omega)-1}{n_f(\omega)+1}\ e^{2in_f(\omega)d_f\omega/c}\right)^j \\ &= E_{\mathrm{in}}(\omega)\frac{2e^{in_f(\omega)d_f\omega/c}}{1+n_f(\omega)}\frac{1}{1-\dfrac{n_f(\omega)-n_s(\omega)}{n_f(\omega)+n_s(\omega)}\dfrac{n_f(\omega)-1}{n_f(\omega)+1}\ e^{2in_f(\omega)d_f\omega/c}}, \end{aligned} \tag{3-22}$$

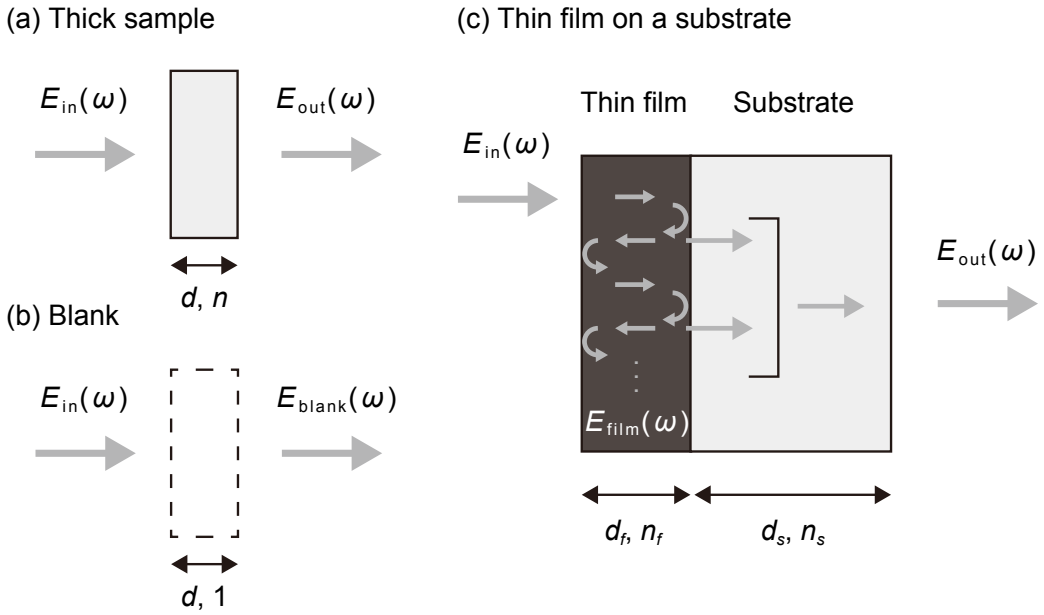

Figure 3-4: Schematic illustrations of the transmitted THz E-field for (a) a thick sample, (b) blank, and (c) a thin film on a substrate.

where $n_{f(s)}$ and $d_{f(s)}$ denote the refractive index and thickness of the thin film (substrate), respectively. Then, the transmitted THz E-field after the substrate $E_{\text{out}}(\omega)$ is written as

$$E_{\text{out}}(\omega) = E_{\text{film}}(\omega)\frac{2n_f(\omega)}{n_f(\omega)+n_s(\omega)}\frac{2n_s(\omega)}{n_s(\omega)+1}\, e^{in_s(\omega)d_s\omega/c}. \tag{3-23}$$

Since the blank THz E-field $E_{\text{blank}}(\omega)$ can be obtained by substituting $d = d_f + d_s$ into Eq. (3-20), the complex transmittance is given by

$$t(\omega) = \frac{E_{\text{out}}(\omega)}{E_{\text{blank}}(\omega)} = \frac{8n_f(\omega)n_s(\omega)}{(1+n_f(\omega))(n_f(\omega)+n_s(\omega))(n_s(\omega)+1)} \frac{e^{i\left[(n_f(\omega)-1)d_f+(n_s(\omega)-1)d_s\right]\omega/c}}{1-\frac{n_f(\omega)-n_s(\omega)}{n_f(\omega)+n_s(\omega)}\frac{n_f(\omega)-1}{n_f(\omega)+1}\, e^{2in_f(\omega)d_f\omega/c}}. \tag{3-24}$$

In the THz-TDS experiment, $n_f(\omega)$ is determined by measuring the THz E-field for the substrate, the thin film on the substrate, and blank. Firstly, using the THz E-field for the substrate and blank, $n_s(\omega)$ is obtained from Eq. (3-21). Secondly, using the obtained $n_s(\omega)$, the refractive index of the thin film $n_f(\omega)$ is obtained by solving Eq. (3-24) in terms of $n_f(\omega)$.

Reflection geometry

For bulk samples, the complex refractive index can be determined by THz-TDS in reflection geometry. The reflected THz E-field from the bulk sample as illustrated in Fig. 3-5(b) is represented by using the complex reflectivity $r_{\text{bulk}}(\omega)$ as

$$E_{\text{bulk}}(\omega) = r_{\text{bulk}}(\omega)E_{\text{in}}(\omega), \tag{3-25}$$

where $E_{\text{in}}(\omega)$ is the incident THz E-field. To obtain this incident THz E-field $E_{\text{in}}(\omega)$, the reflected THz E-field from a reference material is measured as shown in Fig. 3-5(a), which has a unity reflectivity at the THz frequency range like a gold mirror. Since the reflected THz E-field from a reference can be expressed as $E_{\text{ref}}(\omega) = -E_{\text{in}}(\omega)$, the complex reflectivity is written as

$$r_{\text{bulk}}(\omega) = -\frac{E_{\text{bulk}}(\omega)}{E_{\text{ref}}(\omega)}. \tag{3-26}$$

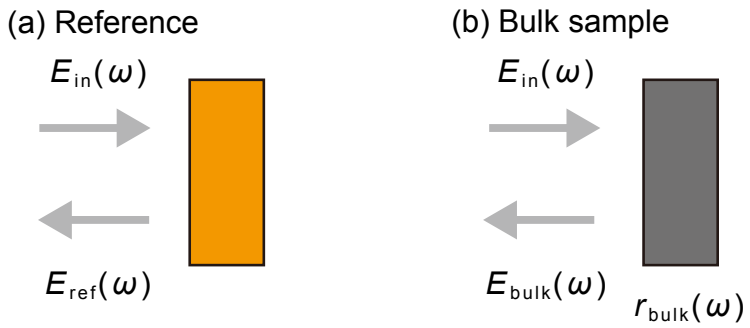

Figure 3-5: Schematic illustrations of the reflected THz E-field for (a) a reference gold mirror and (b) a bulk sample.

Using thus obtained $r_{\mathrm{bulk}}(\omega)$, the complex refractive index of the bulk sample is simply given by

$$n_{\mathrm{bulk}}(\omega) = \frac{1 - r_{\mathrm{bulk}}(\omega)}{1 + r_{\mathrm{bulk}}(\omega)}. \tag{3-27}$$

Dielectric function and optical conductivity

Once the complex refractive index of a sample $n(\omega)$ is determined, the complex dielectric constant $\varepsilon(\omega)$ and the complex optical conductivity $\sigma(\omega)$ can be calculated by using the following relations:

$$\varepsilon(\omega) = n(\omega)^2, \tag{3-28}$$

$$\sigma(\omega) = -i\varepsilon_0\omega(\varepsilon(\omega) - \varepsilon_b). \tag{3-29}$$

Here ε_b is the background dielectric constant of the sample.

3.3 Wavelength conversion to near-infrared and mid-infrared pulses

To perform the phonon-pumping experiment on $YBa_2Cu_3O_{6+y}$ (YBCO), we generated an intense MIR pulse by the difference frequency generation (DFG) method using two NIR pulses obtained by the optical parametric amplifier (OPA).

3.3.1 Optical parametric amplification (OPA)

The optical parametric amplification is one of the specific cases of the DFG [107, 112, 113]. The principle of the optical parametric amplification is as follows: when two beams are mixed in a suitable NC such as sapphire, the pulse energy is transferred from a higher-frequency and higher-intensity beam (pump beam, at the angular frequency ω_p) to a lower-frequency and lower-intensity one (signal beam, at the angular frequency ω_s) which is thus amplified. Besides, another beam (idler beam, at the angular frequency ω_i) is generated as shown in Fig. 3-6. These three beams satisfy energy conservation as follows:

$$\hbar\omega_p = \hbar\omega_s + \hbar\omega_i. \tag{3-30}$$

For the interaction to be efficient, they also satisfy the momentum conservation, which is called the phase-matching as

$$\hbar\mathbf{k}_p = \hbar\mathbf{k}_s + \hbar\mathbf{k}_i, \tag{3-31}$$

where $\mathbf{k}_p$, $\mathbf{k}_s$, and $\mathbf{k}_i$ are the wave vectors of the pump, signal, and idler beams, respectively.

To generate the MIR beam at the wavelength 15 μm by the DFG of signal and idler beams, the wavelengths of the signal and idler beams are set to $\lambda_s = 1.52$ μm and $\lambda_i = 1.69$ μm, respectively.

Phase-matching for OPA

When all the pump, signal, and idler beams are parallel (collinear geometry), the phase-matching condition Eq. (3-31) can be rewritten as follows:

$$n_p\omega_p = n_s\omega_s + n_i\omega_i, \tag{3-32}$$

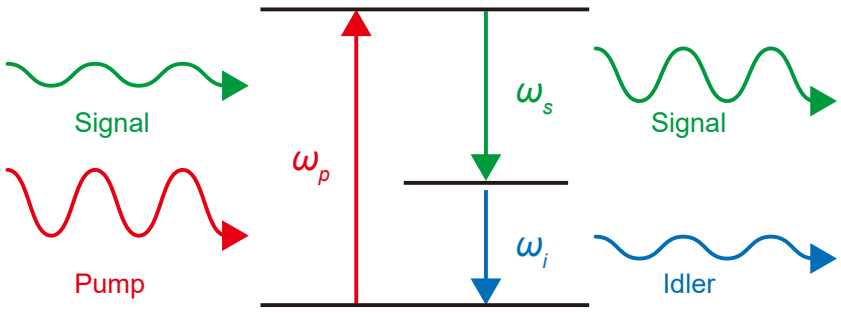

Figure 3-6: The energy diagram of the optical parametric amplification.

where n_p, n_s, and n_i are the refractive indexes of a NC at the pump, signal, and idler wavelength, respectively. It is clear that Eq. (3-32) cannot be satisfied in isotropic bulk materials in the normal dispersion region. However, in some birefringent crystals, Eq. (3-32) can be met by choosing the polarization of the pump beam, which gives the lower refractive index. There are two types of phase-matching: type I phase-matching is the case where both the signal and idler beams have the same polarization, while type II phase-matching is the case where either the signal ($o_s + e_i \rightarrow e_p$) or the idler ($e_s + o_i \rightarrow e_p$) has the orthogonal polarization to the pump [107].

The phase-matching condition is usually achieved by rotating the nonlinear crystal at θ_m from the optical axis. As an example, we consider the case of a negative uniaxial crystal β-barium borate (BBO), whose refractive index from 0.7 μm to 3 μm is calculated using the Sellmeier equation given in Ref. [114] and plotted in Fig. 3-7(a). The type II phase-matching ($o_s + e_i \rightarrow e_p$) is satisfied when

$$n_{ep}(\theta_m)\omega_p = n_{os}\omega_s + n_{ei}(\theta_m)\omega_i, \tag{3-33}$$

where the subscripts o and e denote ordinary and extraordinary polarization, respectively. The refractive index of the extraordinary direction is given by

$$\frac{1}{n_{ep}^2(\theta_m)} = \frac{\sin^2\theta_m}{n_{ep}^2} + \frac{\cos^2\theta_m}{n_{op}^2}, \tag{3-34}$$

$$\frac{1}{n_{ei}^2(\theta_m)} = \frac{\sin^2\theta_m}{n_{ei}^2} + \frac{\cos^2\theta_m}{n_{oi}^2}. \tag{3-35}$$

By numerically solving Eq. (3-33)-(3-35), the phase-matching angle θ_m is obtained as plotted in Fig. 3-7(b).

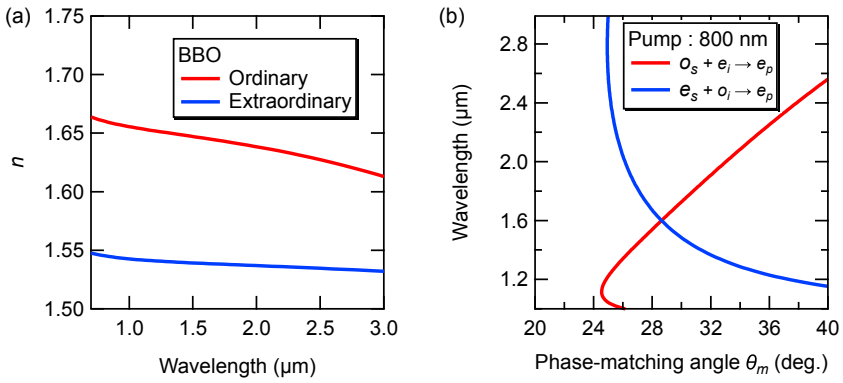

Figure 3-7: (a) The refractive index of a BBO for the ordinary and extraordinary directions [114]. (b) The phase-matching angle θ_m at the pump wavelength of 800 nm for the type II phase-matching.

OPA setup

The schematic illustration of the two-stage OPA is shown in Fig. 3-8. The fundamental 800 nm beam is delivered from a Ti:sapphire laser system, with a pulse duration of 100 fs, a 1 kHz repetition rate, and 4 mJ of pulse energy. For the MIR pulse generation, 2 mJ of the 800 nm beam is usually used to pump the OPA system. The 800-nm beam is split into two beams, with most of the beam used for the second stage amplification process. The fraction of the beam which goes to the first stage is further split into two. One lower intensity beam generates white light after passing through a 5-mm-thick sapphire plate. The visible component whose wavelength is shorter than 1000 nm is removed from the white light by the long-pass filter. The other higher intensity beam is mixed with the white light in the first BBO crystal (BBO1). Here, the type II phase-matching scheme is employed, and the polarization of the white light is rotated by 90° before the sapphire plate. To satisfy the phase-matching condition, we employed a 2.5-mm-thick 28° cut BBO crystal. After the first BBO crystal, a few μJ of the amplified signal beam is obtained.

The signal beam is sent to the second 4-mm-thick BBO crystal (BBO2) cut at 28°, and mixed with the higher intensity 800-nm pump beam reflected by the dichroic mirror (DM1). After the second BBO crystal, typically 500 μJ of the amplified signal and idler beams are obtained.

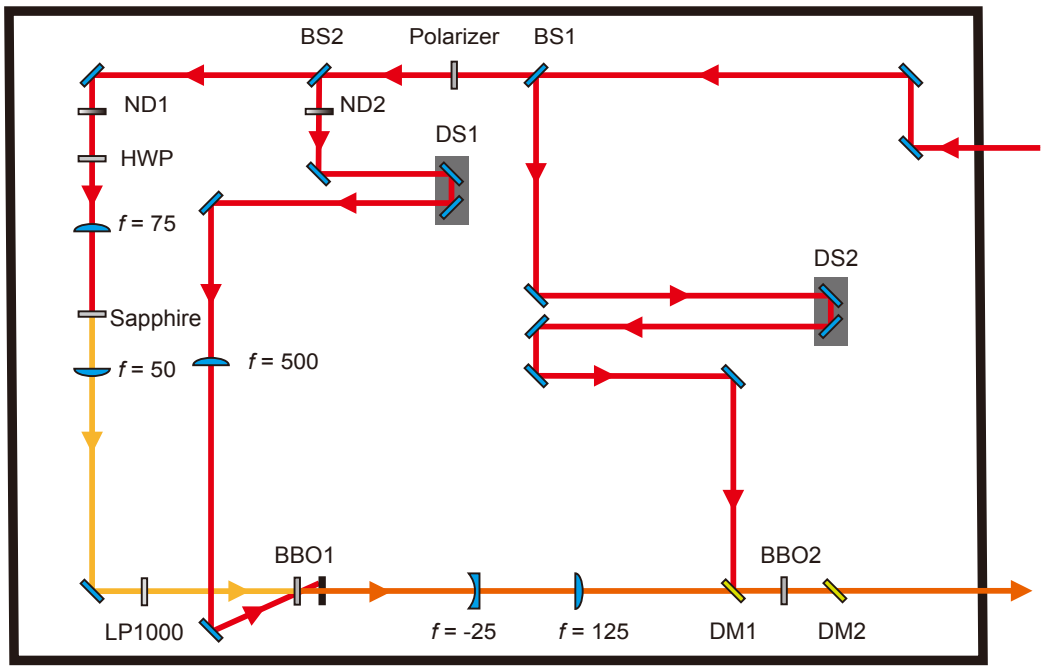

Figure 3-8: Schematic illustration of the two-stage OPA. BS, DS, LP, DM, and ND stand for the beam splitter, delay stage, long-pass filter, dichroic mirror, and neutral density filter, respectively. The focal length of the lens is denoted by f (mm).

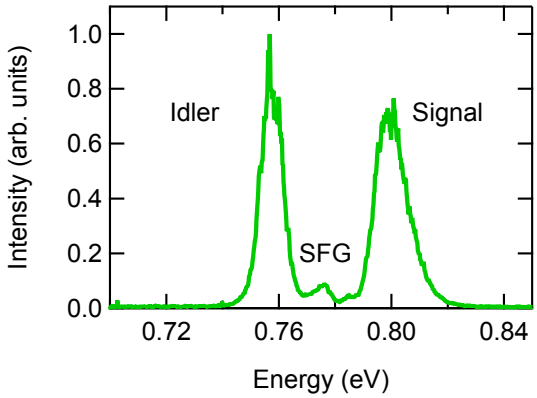

Figure 3-9: The SHG spectrum of the signal and idler pulses using a type-I BBO crystal. To clarify the original photon energy of the signal and idler pulses, the horizontal axis is divided by a factor of 2.

The wavelengths of the obtained signal and idler pulses are evaluated by measuring their second-harmonic generation (SHG) in a type-I BBO crystal. Figure 3-9 shows the typically obtained SHG spectrum of the signal and idler pulses, whose horizontal axis is divided by 2 to acquire the original photon energy. Here, the signal and idler photon energies are evaluated as 0.80 eV and 0.76 eV, respectively. It should be noted that the sum-frequency generation (SFG) of the signal and idler pulses is also detected, which is located in between the signal and idler pulses as its original photon energy of 1.55 eV is divided by a factor of 2.

3.3.2 Mid-infrared pulse generation

Phase matching for DFG

MIR pulses with wavelength at 5-16 μm are generated using a GaSe crystal by the DFG process between the signal and idler beams from the OPA (3-10(a)). The calculated DFG wavelength obtained as a function of signal wavelength is shown in Fig. 3-10(b). To spatially separate the signal and idler beams from the DFG beam, the signal and idler beams should be mixed in noncollinear geometry with an incident angle α. Using the refractive index of GaSe adopted from [115], the phase-matching angle θ and outgoing angle of DFG pulse β are calculated as a function of DFG wavelength for selected α, as plotted in Figs. 3-10(c) and (d).

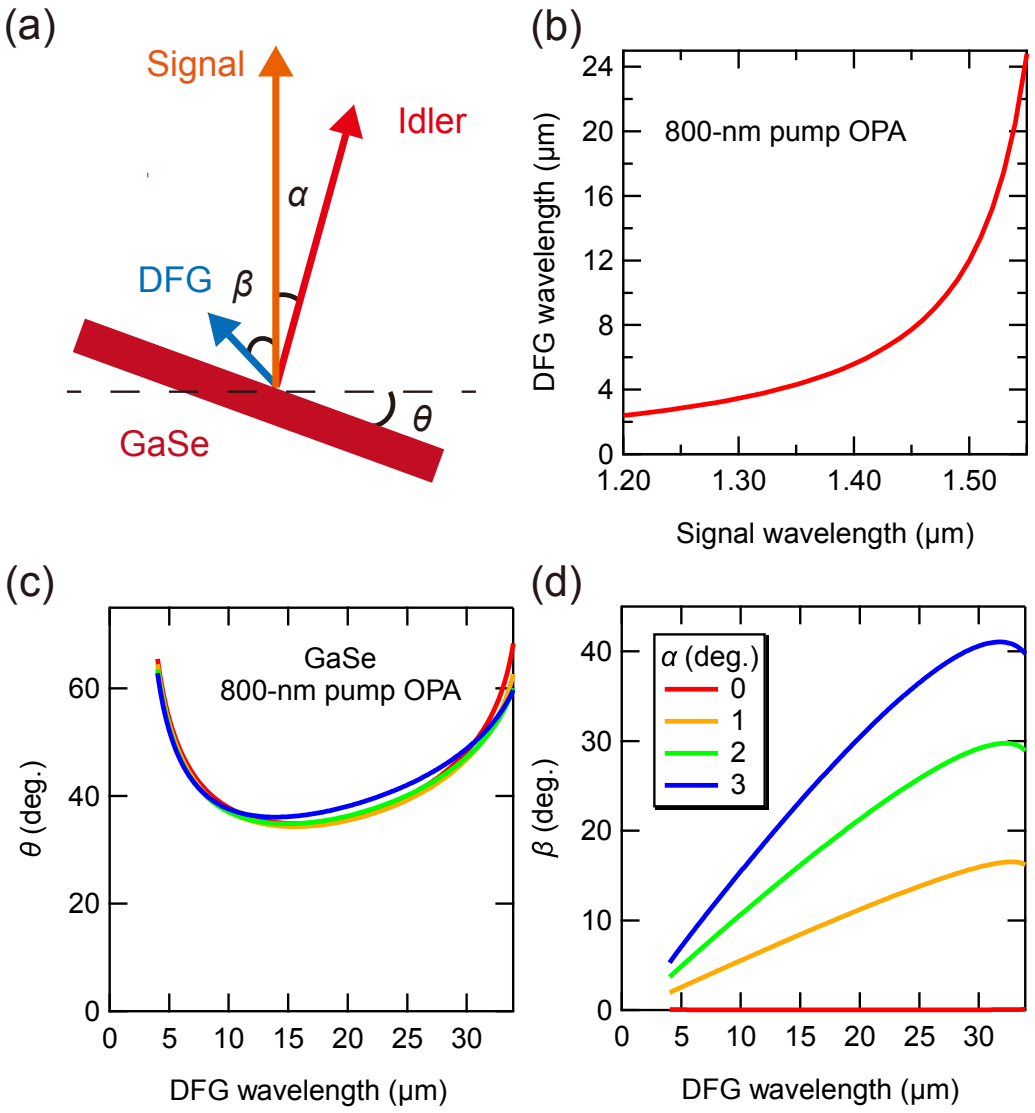

Figure 3-10: (a) Schematic of the DFG setup. (b) DFG wavelength as a function of the signal wavelength in the 800-nm pump OPA. (c) The phase-matching angle θ and (d) the outgoing angle of the DFG beam β for several idler incident angles α.

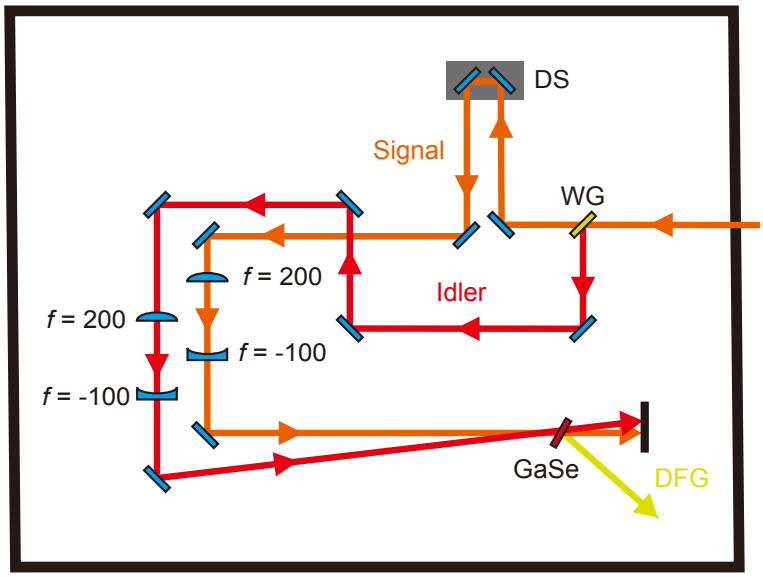

Figure 3-11: Schematic illustration of the DFG system. WG and DS stand for the wire grid polarizer and delay stage, respectively. The focal length of the lens is denoted by f (mm).

DFG setup

The signal and idler beams from the OPA are further delivered to the DFG part, as shown in Fig. 3-11. The polarization of the signal and idler beams are rotated by 90° to achieve the phase-matching of the z-cut GaSe in the p-plane. The beam divergence of the two beams is adjusted by the lens pairs independently. The signal and idler beams are separated by the wire grid polarizer and noncollinearly mixed at a 2 mm-thick GaSe crystal to separate the signal and idler beams from the DFG beam. The generated MIR beam power with a wavelength of 14 μm is typically 6 μJ.

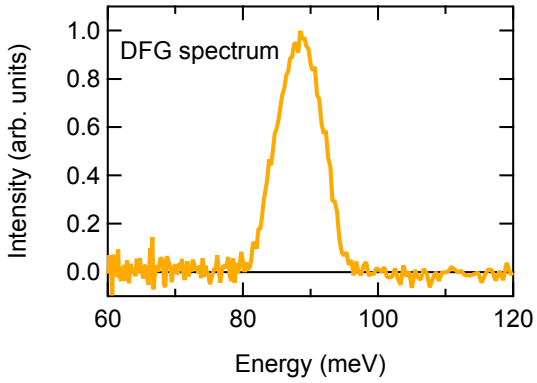

Figure 3-12: DFG spectrum measured by the MCT detector.

3.3.3 Characterizing the mid-infrared pulse

Wavelength

The DFG power spectrum is measured by a Mercury-Cadmium-Tellurium (MCT) detector (KMPC12-2-J1, Kolmar technologies) combined with a spectrometer. The obtained power spectrum of the DFG pulse is displayed in Fig. 3-12. Here, the center frequency of the DFG pulse is tuned to 88.5 meV = 21.4 THz, which corresponds to 14.0 μm in wavelength.

Pulse duration

The pulse duration of the MIR pulse is measured by intensity cross-correlation with an 800-nm pulse, whose pulse duration is obtained by intensity auto-correlation explained in the following.

First, the pulse duration of the 800-nm pulse is measured by the intensity auto-correlation using a 100-μm-thick type-I BBO crystal as depicted in Fig. 3-13(a). Figure 3-13(b) shows an intensity auto-correlation signal of the 800-nm pulse, whose FWHM is $\tau_a =$ 149 fs. Assuming that the optical pulse is a Gaussian pulse, the FWHM of the original pulse (τ_p) is estimated from that of the auto-correlation signal (τ_a) as

$$\tau_p = \frac{\tau_a}{\sqrt{2}}. \tag{3-36}$$

Thus, the pulse duration of 800-nm pulse is estimated as $\tau_p = 105$ fs.

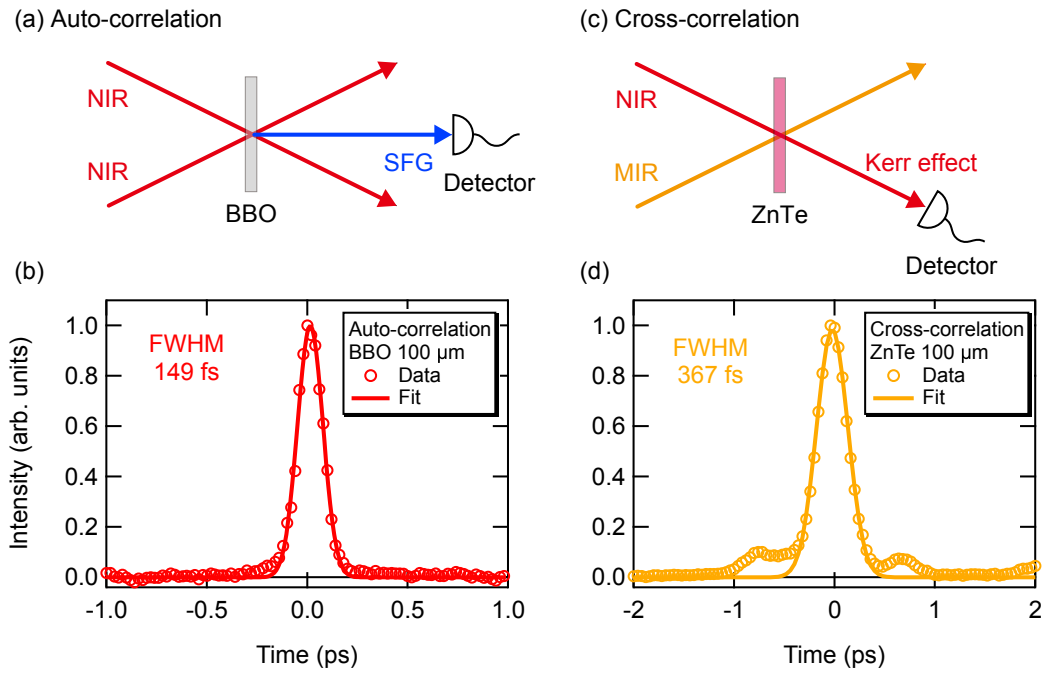

Figure 3-13: (a) Schematic illustration of the auto-correlation measurement. (b) The intensity auto-correlation signal of the 800-nm pulse. The FWHM of the auto-correlation signal is estimated as 149 fs from the Gaussian fit. (c) Schematic representation of the cross-correlation measurement. The polarization rotation of the 800-nm pulse induced by the MIR pulse is detected. (d) The cross-correlation signal of the 14-μm pulse with the 800-nm pulse. The FWHM of the cross-correlation signal is extracted as 367 fs from the Gaussian fit.

Next, the pulse duration of the MIR pulse is determined by the cross-correlation between itself and the 800-nm pulse using a 100-μm-thick ZnTe crystal as a consequence of the Kerr effect [116]. Figure 3-13(c) shows the setup for the cross-correlation measurement. The MIR pulse duration τ_{MIR} is given by the deconvolution of the cross-correlation signal (τ_c) as

$$\tau_{\mathrm{MIR}} = \sqrt{\tau_c^2 - \tau_p^2}. \tag{3-37}$$

Since the FWHM of the cross-correlation signal is extracted as $\tau_c = 367$ fs as shown in Fig. 3-13(d), the pulse width of MIR is estimated as $\tau_{\mathrm{MIR}} = 245$ fs.

Beam size

In the phonon-pumping experiment, the MIR beam is focused on the sample by a ZnSe lens. The MIR beam size at the sample position is estimated by THz camera (IR/V-T0831, NEC). Figure 3-14 shows a typical beam pattern of the MIR pulse measured at the sample position. Since the MIR pulse energy is typically 2 μJ after the ZnSe lens, the MIR fluence is around 200 μJ/cm^2 considering the power loss by the diamond window of the cryostat.

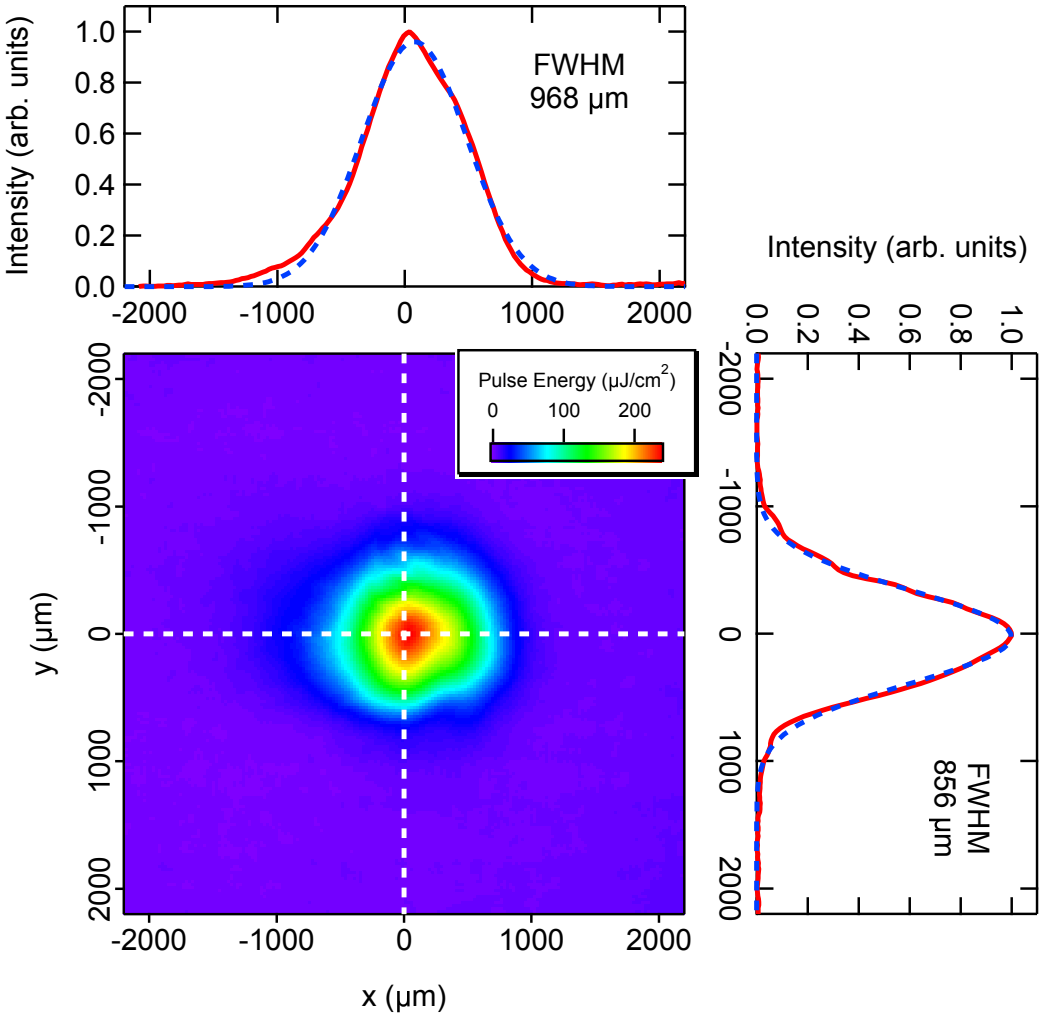

Figure 3-14: The MIR beam pattern at the sample position measured by a THz camera. The intensity profile of the horizontal and vertical direction along the white dashed lines are plotted in the top and right panels, respectively. The red curves denote the data, and the blue dashed curves are the Gaussian fits.

Chapter 4

Superconducting fluctuations in $Bi_2Sr_2CaCu_2O_{8+x}$

To elucidate the onset temperature of the superconducting fluctuations in cuprate superconductors by using the Higgs-mode response, THz pump-optical probe spectroscopy is performed on $Bi_2Sr_2CaCu_2O_{8+x}$ (BSCCO) thin films. In the oscillatory behavior of the pump-probe response, two onset temperatures are identified, and their origins are discussed in detail.

4.1 Sample properties

In THz pump-optical probe spectroscopy, underdoped (UD) and overdoped (OD) BSCCO thin films have been used, which are grown by the sputtering method on MgO substrates. The superconducting transition temperature (T_c) of these samples is determined by the magnetic moment measured by a superconducting quantum interference device (SQUID) under zero-field cooling (ZFC) and field-cooling (FC) as shown in Fig. 4-1. Since determined T_c is $T_c = 76$ K for the UD thin film and $T_c = 67$ K for the OD thin film, UD and OD thin films are referred to as UD76 and OD67, respectively.

The thickness of the film is 60 nm for UD76 and 160 nm for OD67. The reason why the films of different thicknesses have been used is the limited availability of high-quality BSCCO thin films grown on MgO. However, the film thickness does not affect the results of the THz pump-optical probe spectroscopy experiments as shown in Appendix A.

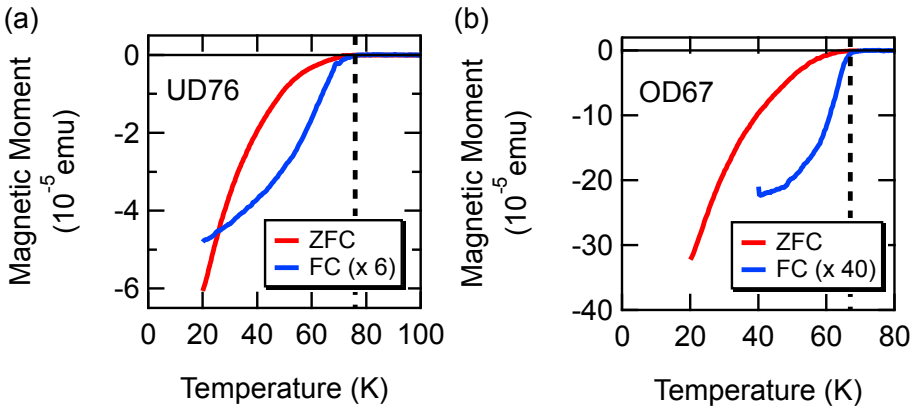

Figure 4-1: Magnetic moment of the (a) UD and (b) OD BSCCO thin films measured by SQUID. The black dashed lines denote the determined T_c's.

4.2 THz pump-optical probe spectroscopy

4.2.1 Experimental setup

A schematic illustration of the THz pump-optical probe spectroscopy setup is depicted in Fig. 4-2(a). The output of a regenerative amplified Ti:sapphire laser system (Coherent Libra, the central wavelength of 800 nm, pulse duration of 100 fs, pulse energy of 4 mJ, and repetition rate of 1 kHz) was split into two beams: one for intense THz-pump pulse generation and the other for the optical probe pulse. To generate an intense THz-pulse, we combined the tilted-pulse-front technique with a $LiNbO_3$ crystal explained in Chapter 3 and the tight focusing method [117]. The amplitude of the THz-pump electric field (E-field) is controlled by rotating the wire grid polarizer (WG2) in Fig. 4-2(a).

The THz-pump E-field is measured by electro-optical sampling in a 380-μm GaP (110) crystal. Figures 4-2(b) and (c) show the waveform and power spectrum of the THz-pump pulse inside the cryostat, respectively. The peak E-field reaches up to 400 kV/cm. The center frequency of the THz-pump E-field is around 0.6 THz, which is much smaller than the anti-nodal superconducting gap energy $2\Delta_0 > 20$ meV ~ 5 THz for the present doping levels of the BSCCO samples [97, 118–120].

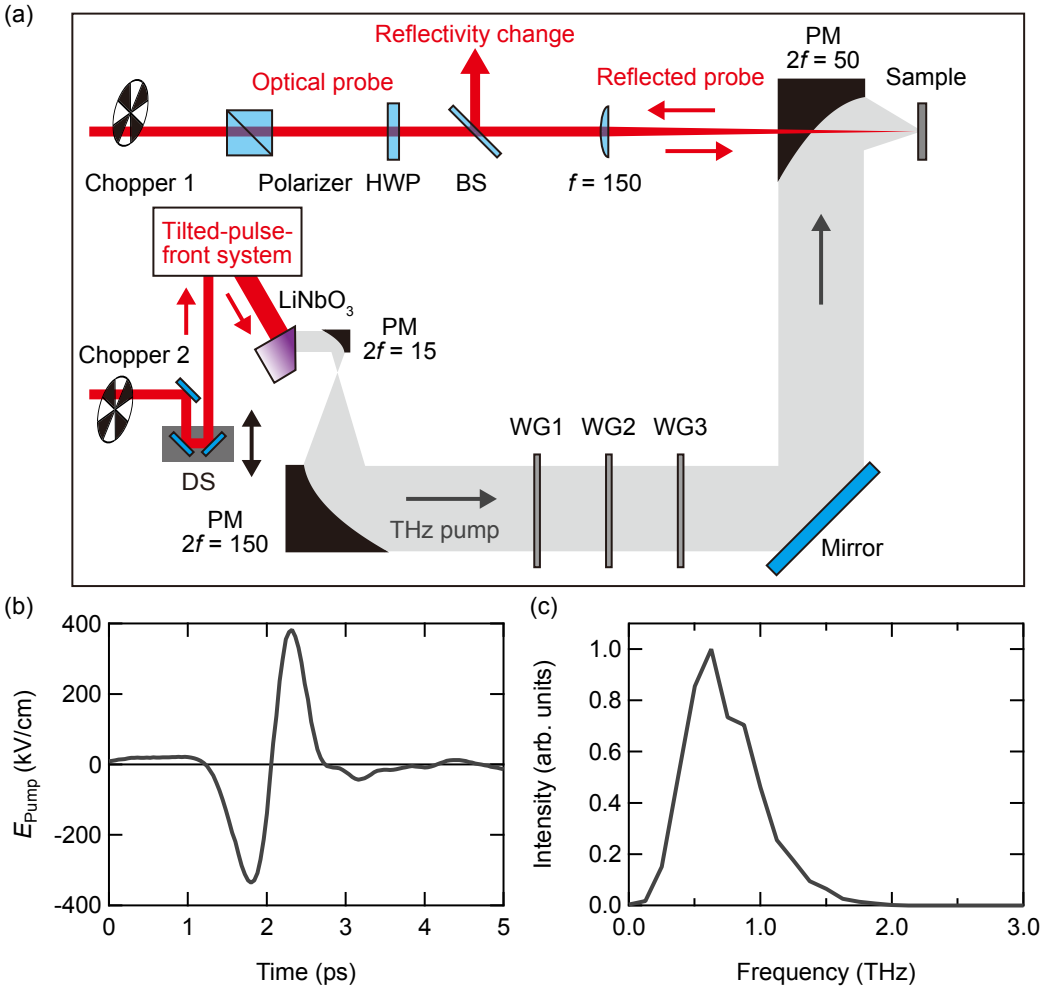

Figure 4-2: (a) Schematic representation of the THz pump-optical probe spectroscopy setup. PM, DS, HWP, BS and WG are parabolic mirror, delay stage, half-wave plate, beam splitter, and wire grid polarizer, respectively. (b), (c) The waveform and power spectrum of the THz-pump E-field measured at the sample position, respectively.

4.2.2 THz-pump induced transient reflectivity change

THz pump-optical probe spectroscopy measurements have been carried out as a function of the pump and probe polarization angles θ_{Pump}, θ_{Probe} defined in Fig. 4-3(a), to distinguish the Higgs-mode and charge density fluctuation (CDF) contributions.

Figures 4-3(b) and (c) represent the THz pump-induced reflectivity change $\Delta R/R$ at 15 K for UD76 and OD67, respectively. In both samples, $\Delta R/R$'s exhibit induced oscillations which follow the squared THz-pump E-field ($E_{\mathrm{Pump}}(t)^2$). In addition to the induced oscillation, $\Delta R/R$'s have decaying components that survives for as long as 10 ps. When increasing the THz-pump E-field, $\Delta R/R$ monotonically increases in OD67, while it shows a saturation above 200 kV/cm in UD76. The THz-pump peak E-field dependences of $\Delta R/R$ at fixed delay times for UD76 and OD67 are shown in Figs. 4-3(d) and (e), respectively. For UD76, $\Delta R/R$ follows the square of the THz-pump E-field for weaker peak E-fields, while it saturates above 170 kV/cm. For OD67, $\Delta R/R$ follows the square of the THz-pump E-field and does not show a substantial saturation behavior until 400 kV/cm. To ensure the third-order nonlinear regime, we set the peak THz E-field to 130 kV/cm for UD76 and 220 kV/cm for OD67 denoted by the vertical arrows in Figs. 4-3(d) and (e), respectively.

Polarization dependence of $\Delta R/R$

In the third-order nonlinear regime, the oscillatory component in $\Delta R/R$ can be considered as a THz Kerr effect where the intense THz pulse modulates the optical reflectivity at the wavelength of 800 nm [121]. The amplitude of the THz Kerr signal can be written using the third-order nonlinear susceptibility $\chi^{(3)}$ as [85, 121]

$$\frac{\Delta R}{R}\left(E_i^{\mathrm{Pump}}, E_j^{\mathrm{Probe}}\right) \sim \frac{1}{R}\frac{\partial R}{\partial \varepsilon_1}\varepsilon_0 \,\mathrm{Re}\,\chi^{(3)}_{ijkl} E_k^{\mathrm{Pump}} E_l^{\mathrm{Pump}}, \tag{4-1}$$

where ε_1 is the real part of the dielectric constant and E_i is the i-th component of the THz-pump or optical-probe E-field. Since BSCCO has the tetragonal symmetry, the nonlinear susceptibility $\chi^{(3)}$ can be decomposed into the irreducible representations of D_{4h} point group as follows [85, 107]:

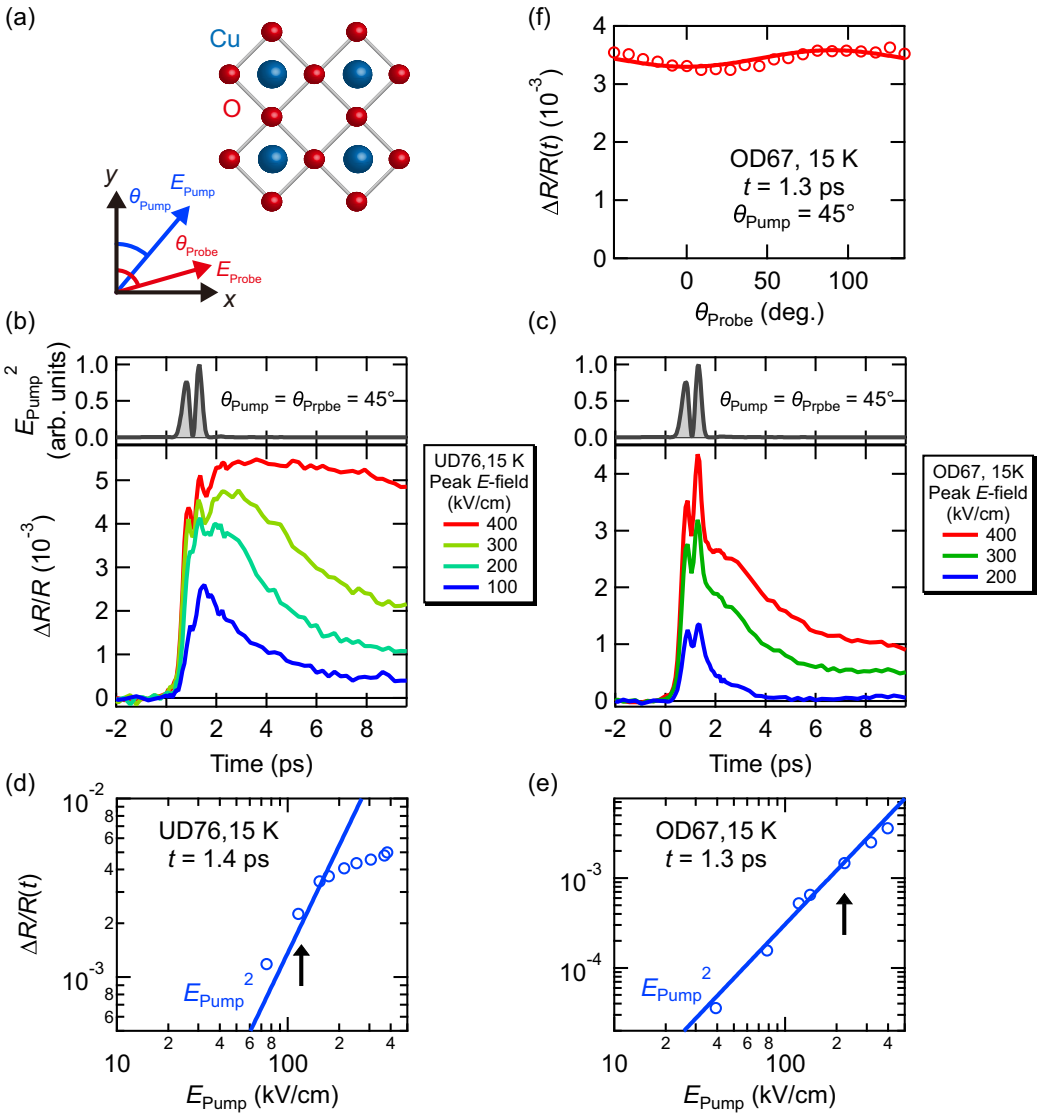

Figure 4-3: (a) A schematic of the CuO_2 plane. The pump (θ_{Pump}) and probe (θ_{Probe}) polarization angles are defined relative to the Cu-O bond (y-axis). (b), (c) THz-pump-induced transient reflectivity change $\Delta R/R$ at 15 K for UD76 and OD67, respectively. The upper panels are the waveforms of the squared THz-pump E-field. (d), (e) The amplitude of $\Delta R/R$ at a fixed delay of t at 15 K when $\theta_{\mathrm{Pump}} = \theta_{\mathrm{Probe}} = 45°$ for UD76 and OD67, respectively. The lines indicate the slope of 2 for the guides to the eye. The vertical arrows indicate the THz-pump peak E-field used for the experiments. (f) The amplitude of $\Delta R/R$ at delay time of 1.3 ps for OD67 at 15 K as a function of the probe polarization angle θ_{Probe} when $\theta_{\mathrm{Pump}} = 45°$.

$$\chi^{(3)}(\theta_{\mathrm{Pump}},\theta_{\mathrm{Probe}}) = \frac{1}{2}\left(\chi^{(3)}_{A_{1g}} + \chi^{(3)}_{B_{1g}}\cos 2\theta_{\mathrm{Pump}}\cos 2\theta_{\mathrm{Probe}} + \chi^{(3)}_{B_{2g}}\sin 2\theta_{\mathrm{Pump}}\sin 2\theta_{\mathrm{Probe}}\right). \quad (4\text{-}2)$$

Here, $\chi^{(3)}_{A_{1g}}$, $\chi^{(3)}_{B_{1g}}$, and $\chi^{(3)}_{B_{2g}}$ are defined as $\chi^{(3)}_{A_{1g}} = \chi^{(3)}_{xxxx} + \chi^{(3)}_{xxyy}$, $\chi^{(3)}_{B_{1g}} = \chi^{(3)}_{xxxx} - \chi^{(3)}_{xxyy}$, and $\chi^{(3)}_{B_{2g}} = \chi^{(3)}_{xyxy} + \chi^{(3)}_{xyyx}$, respectively.

Figure 4-3(f) shows the transient reflectivity change $\Delta R/R$ for OD67 at 15 K as a function of the probe polarization θ_{Probe}, and demonstrates that $\Delta R/R$ is dominated by the isotropic A_{1g} component while a slight polarization-angle-dependence is identified. Mean-field calculations demonstrated that the Higgs-mode response should appear only in the isotropic A_{1g} channel, whereas the CDF response should have the largest contribution in the polarization-dependent B_{1g} channel [85]. Therefore, the observed THz Kerr signal below T_{c} can be reasonably attributed to the Higgs-mode response, which is in good agreement with the results of the BSCCO single crystals [85]. The polarization dependent component thus most likely originates from the CDF. In the following, we focus on the A_{1g} components of $\Delta R/R$ to study the Higgs-mode response.

Temperature dependence of $\Delta R/R$

Figures 4-4(a) and (b) exhibit the A_{1g} component of the transient reflectivity change $\Delta R/R$ for $\theta_{\mathrm{Pump}} = 45°$ at selected temperatures for UD76 and OD67, respectively. At 30 K below T_{c}, the induced oscillation, i.e., THz Kerr signal which follows the squared THz-pump E-field $E_{\mathrm{Pump}}(t)^2$ is identified for both samples. In addition to the THz Kerr signal, $\Delta R/R$ has a decaying component which survives for as long as 10 ps. For UD76 at 120 K, above T_{c}, $\Delta R/R$ consists of a smaller THz Kerr signal and a decaying signal whose sign is switched after 2 ps. The negative decaying signal is also discerned in the THz-pump induced reflectivity change in UD and optimally doped (OP) BSCCO single crystal, which is ascribed to the quasiparticle relaxation in the pseudogap state [85] (the decaying component in OP sample is described in Chapter 2). At 268 K far above T_{c}, the decaying signal remains positive for all the delay times. For OD67 at 150 K above T_{c}, the signal is composed of a smaller THz Kerr signal and a decaying signal. The overall results are similar to those observed in the single crystals [85].

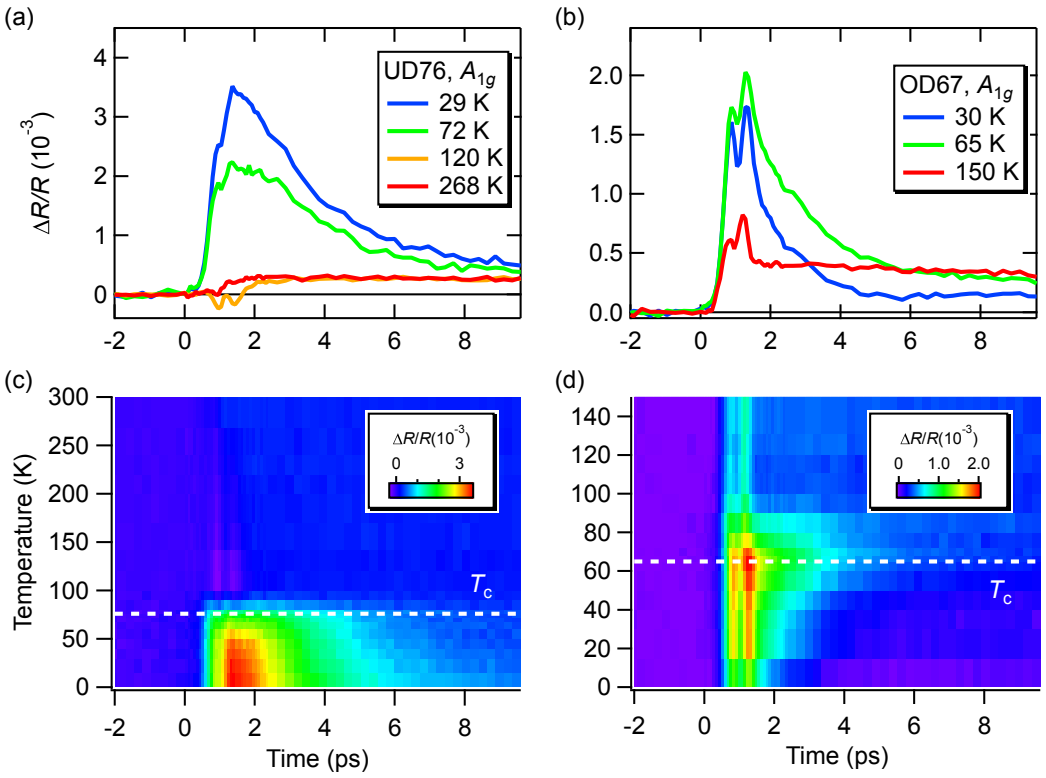

Figure 4-4: (a), (b) The A_{1g} components of the THz-pump-induced transient reflectivity change $\Delta R/R$ at selected temperatures for UD76 and OD67, respectively. (c), (d) The A_{1g} components of the reflectivity change $\Delta R/R$ as a function of temperature and delay time for UD76 and OD67, respectively. The horizontal white dashed lines denote T_c.

The temperature dependence of the A_{1g} components of the transient reflectivity change $\Delta R/R$ is shown in Figs. 4-4(c) and (d) for UD76 and OD67, respectively. In both samples, $\Delta R/R$ displays a sharp increase from slightly above T_c with decreasing the temperature.

Since the Higgs-mode response is expected to follow $E_{\mathrm{Pump}}(t)^2$, the amplitude of the THz Kerr signal can be extracted from the Fast Fourier transformation (FFT) of $\Delta R/R$. Figures 4-5(a) and (b) represent the FFT spectrum of the squared THz-pump E-field $E_{\mathrm{Pump}}(t)^2$ and the A_{1g} component of $\Delta R/R$ for the thin films. The FFT amplitude of the A_{1g} component of $\Delta R/R$ around 1.5 THz, which corresponds to the peak in the FFT spectrum

of $E_{\mathrm{Pump}}(t)^2$, increases with decreasing temperature, except for the data below 72 K for UD76. To discuss the precise temperature dependence of the FFT amplitude, we have to consider the temperature dependence of the THz E-field that penetrates into the sample, which will be described in the next subsection. The integrated FFT amplitudes from 1.2 to 2.2 THz (A_{FFT}) for UD76 and OD67 are plotted in Figs. 4-5(c) and (d), respectively. As the temperature is lowered, the integrated FFT amplitude A_{FFT} displays a sharp increase below 100 K for both samples, whereas it exhibits a rather gradual increase at higher temperatures. The origin of A_{FFT} at higher temperatures will be discussed in the discussion section.

Calculation of the third-order nonlinear susceptibility $\chi^{(3)}$

To quantitatively evaluate the temperature dependence of the amplitude of the THz Kerr signal, the temperature dependence of the squared THz-pump E-field inside the thin film should be considered in the analysis of third-order nonlinear susceptibility $\chi^{(3)}$ of the THz Kerr signal. Here, the temperature dependence of the squared THz-pump E-field inside the thin film (B_{FFT}) is estimated using the refractive index of the thin film and substrate obtained by THz time-domain spectroscopy (THz-TDS) in the transmission geometry, which will be described in the next subsection.

The third-order nonlinear susceptibility $\chi^{(3)}$ is evaluated by calculating the THz-pump E-field inside the thin film as follows. Firstly, the FFT of the A_{1g} component of $\Delta R/R(t)$ given by Eq. (4-1) can be expressed as

$$\begin{aligned}\frac{\Delta R_{A_{1g}}}{R}(\omega) &= \frac{1}{R}\frac{\partial R}{\partial \varepsilon_1}\varepsilon_0 \int_0^\infty \mathrm{Re}\chi^{(3)}_{A_{1g}} E_{\mathrm{Film}}(t)^2 e^{-i\omega t}\mathrm{d}t \\ &= \frac{1}{R}\frac{\partial R}{\partial \varepsilon_1}\varepsilon_0 \mathrm{Re}\chi^{(3)}_{A_{1g}} B(\omega). \end{aligned} \tag{4-3}$$

Here, $E_{\mathrm{Film}}(t)$ is the E-field inside the thin film in the time domain and $B(\omega)$ is the FFT of $E_{\mathrm{Film}}(t)^2$. In Eq. (4-3), the third-order nonlinear susceptibility of the Higgs mode $\mathrm{Re}\chi^{(3)}_{A_{1g}}$ is singled out from the integral because it has no frequency dependence when the probe photon energy is much higher than the pump photon energy and superconducting gap energy [85].

Secondly, the THz-pump E-field inside the film in the time domain $E_{\mathrm{Film}}(t)$ is calculated by using its FFT $E_{\mathrm{Film}}(\omega)$. In the frequency domain, this $E_{\mathrm{Film}}(\omega)$ can be expressed by the incident THz-pump E-field $E_{\mathrm{Pump}}(\omega)$ as follows:

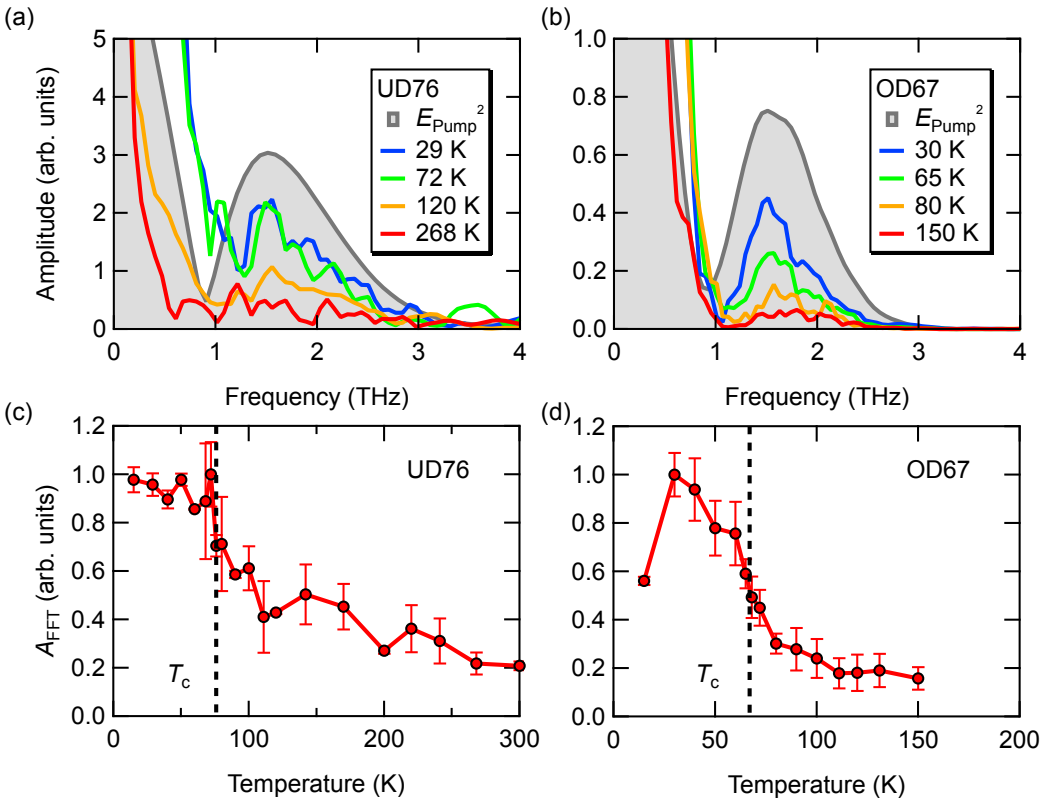

Figure 4-5: (a), (b) FFT spectrum of the A_{1g} component of $\Delta R/R$ at selected temperatures for UD76 and OD67, respectively. The gray curve is the FFT spectrum of the squared THz-pump E-field ($E_{\mathrm{Pump}}(t)^2$). (c), (d) Temperature dependence of the integrated FFT amplitude of $\Delta R/R$ from 1.2 to 2.2 THz (A_{FFT}) for UD76 and OD67, respectively. The vertical black dashed lines denote T_c.

$$\frac{E_{\mathrm{Film}}(\omega)}{E_{\mathrm{Pump}}(\omega)} = \frac{\dfrac{2}{1+n_{\mathrm{Film}}(\omega)}\, e^{i(n_{\mathrm{Sub}}(\omega)-1)\omega d/c}}{1-\dfrac{n_{\mathrm{Film}}(\omega)-1}{n_{\mathrm{Film}}(\omega)+1}\,\dfrac{n_{\mathrm{Film}}(\omega)-n_{\mathrm{Sub}}(\omega)}{n_{\mathrm{Film}}(\omega)+n_{\mathrm{Sub}}(\omega)}\, e^{2in_{\mathrm{Sub}}(\omega)\omega d/c}}. \tag{4-4}$$

Here, d is the thickness of the thin film, and $n_{\mathrm{Film}}(\omega)$ and $n_{\mathrm{Sub}}(\omega)$ are the complex refractive indices of the thin film and the substrate, respectively. Since the THz-pump FFT power spectrum $E_{\mathrm{Pump}}(\omega)^2$ covers the frequency

range from 0.1 to 1.5 THz as shown in Fig. 4-2(c), $E_{\mathrm{Film}}(\omega)$ can be calculated by using $n_{\mathrm{Film}}(\omega)$ and $n_{\mathrm{Sub}}(\omega)$ in the same frequency region. As the size of the thin film is 3×3 mm^2 and not large enough to measure the transmittance below 0.4 THz in THz-TDS measurements, the refractive index of the thin film $n_{\mathrm{Film}}(\omega)$ is obtained from the fitting to the complex optical conductivity $\sigma(\omega)$ with the two-fluid model written by Eq. (4-6) which is explained in the next subsection.

Finally, by integrating Eq. (4-3), the third-order nonlinear susceptibility can be described as

$$\mathrm{Re}\chi^{(3)}_{A_{1g}} = \frac{\int_{2\pi f_1}^{2\pi f_2} \frac{\Delta R_{A_{1g}}}{R}(\omega)\mathrm{d}\omega}{\int_{2\pi f_1}^{2\pi f_2} B(\omega)\mathrm{d}\omega} = \frac{A_{\mathrm{FFT}}}{B_{\mathrm{FFT}}}, \tag{4-5}$$

where the lower and upper limits of the integral are set to $f_1 = 1.2$ THz and $f_2 = 2.2$ THz, respectively. A_{FFT} is the integrated amplitudes of $\Delta R/R(\omega)$ from $\omega/2\pi = 1.2$ to 2.2 THz and shown in Figs. 4-5(c) and (d). B_{FFT} is the integrated amplitudes of $B(\omega)$ from $\omega/2\pi = 1.2$ to 2.2 THz and plotted in Figs. 4-6(a) and (b). Using these A_{FFT} and B_{FFT}, the nonlinear susceptibility $\mathrm{Re}\chi^{(3)}_{A_{1g}} \equiv \chi^{(3)}$ is calculated as shown in Figs. 4-7(a) and 4-8(a): it gradually increase as the temperature decreases from 200 K, and displays a slope change from slightly above T_{c}. As our previous work has demonstrated [85], we attribute the A_{1g} component of the THz Kerr signal below T_{c} to the Higgs mode. In the following, we discuss the temperature dependence of $\chi^{(3)}$ above T_{c}.

Figure 4-7(a) shows the nonlinear susceptibility $\chi^{(3)}$ for UD76 thin film as a function of temperature (the gray curve). To determine an onset temperature of the THz Kerr signal (T_1^{ons}), we take the second derivative of $\chi^{(3)}$ with respect to the temperature $\partial^2\chi^{(3)}/\partial T^2$ which is plotted by the red curve in Fig. 4-7(b). The onset temperature T_1^{ons} is determined as the upturn in the temperature dependence of the second derivative. Figures 4-7(c) and (d) are the expanded figures around T_{c} of Figs. 4-7(a) and (b), respectively. With decreasing temperature from high temperature, the nonlinear susceptibility $\chi^{(3)}$ shown in Fig. 4-7(a) has an onset not at T_{c} but between 80 K and 100 K, which are denoted by the orange dashed lines in Fig. 4-7(c). Concomitantly, the second derivative shows an onset around 90 K, as shown in Fig. 4-7(d). Thus, the onset temperature of the THz Kerr signal for UD76 is extracted as $T_1^{\mathrm{ons}} = 90$ K. We also identify a second onset temperature

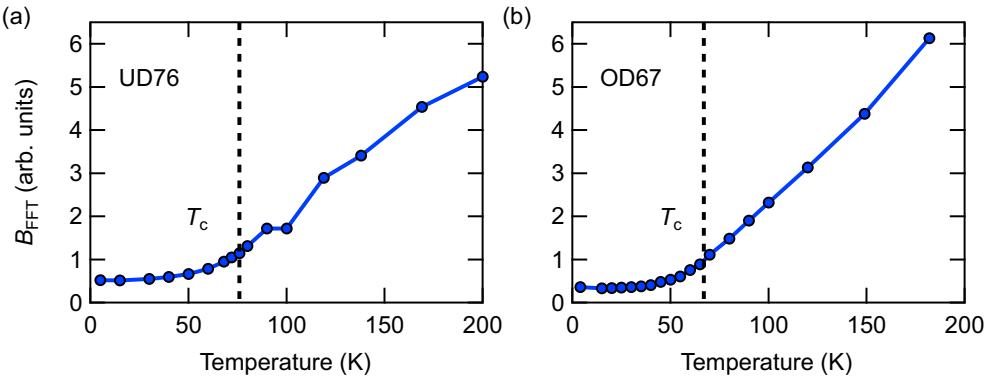

Figure 4-6: (a), (b) The FFT amplitude of the squared THz-pump E-field inside the thin film (B_{FFT}) as a function of temperature for UD76 and OD67, respectively. The FFT amplitude is normalized by its value at T_{c}.

of $\chi^{(3)}$ (T_2^{ons}) from the slope change in the temperature dependence of $\chi^{(3)}$, around $T_2^{\mathrm{ons}} = 185$ K as plotted in the inset of Fig. 4-7(a). We note that the $\chi^{(3)}$ signal above T_2^{ons} sustains even at room temperature for most of the samples. This high-temperature signal can be attributed to rather generic nonlinear transport in the normal metal phase as observed in metallic film and particles [122–128].

Next, we examine the temperature dependence of $\chi^{(3)}$ for OD67 thin film plotted in Fig. 4-8. Similarly to UD76 sample, the nonlinear susceptibility $\chi^{(3)}$ for OD67 in Fig. 4-8(c) displays a slope change not at T_{c} but slightyly above T_{c}. In the same manner with the UD76 sample, we evaluated the onset temperature from the upturn of $\partial^2\chi^{(3)}/\partial T^2$ which locates at 80 K as plotted in Fig. 4-8(d). Therefore, the first onset temperature of $\chi^{(3)}$ is determined as $T_1^{\mathrm{ons}} = 80$ K for OD67. From the inset in Fig. 4-8(a), the second onset temperature is estimated to be $T_2^{\mathrm{ons}} = 116$ K.

Since the first onset temperatures of $\chi^{(3)}$ (T_1^{ons}'s) for both thin films locate slightly above T_{c}, it is reasonable to attribute the finite $\chi^{(3)}$ response at $T_c < T < T_1^{\mathrm{ons}}$ to superconducting phase fluctuation, where the long-range phase coherence fluctuates on the picosecond time scale, which can be probed by THz and microwave spectroscopy [26–29, 129]. Accordingly, T_1^{ons} should be viewed as a temperature scale of phase fluctuation above T_{c}, but not as a well-defined phase transition temperature. We will further examine this interpretation in the following by comparing T_1^{ons} with the onset temperature of the phase stiffness obtained by THz-TDS on the same thin films. Moreover,

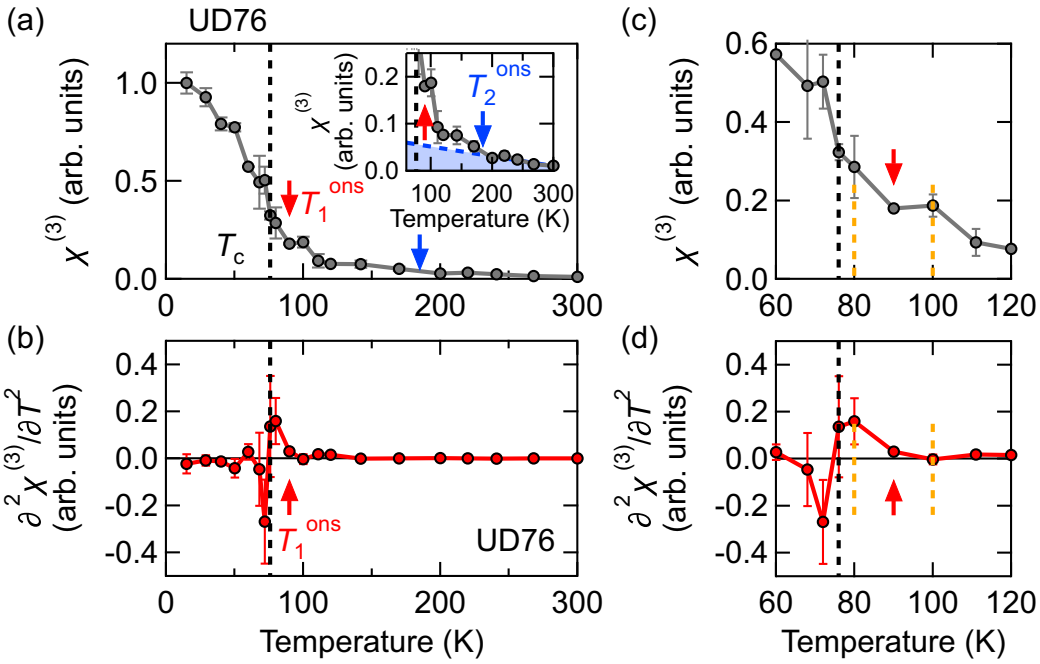

Figure 4-7: (a) The third-order nonlinear susceptibility of the THz Kerr signal $\chi^{(3)}$ for UD76 BSCCO thin film as a function of temperature. (b) The second derivative of $\chi^{(3)}$ with respect to the temperature. The vertical red arrows denote the onset temperature of the sharp increase in the THz Kerr signal $T_1^{\rm ons}$ determined from the second derivative $\partial^2\chi^{(3)}/\partial T^2$. The vertical blue arrows denote the onset temperature of the THz Kerr signal $T_2^{\rm ons}$. The inset in (a) is its expanded figure around $T_1^{\rm ons}$ and $T_2^{\rm ons}$. (c), (d) The expanded figures around T_c and $T_1^{\rm ons}$ of (a) and (b), respectively. The orange vertical dashed lines in (c) and (d) denote the error bars for $T_1^{\rm ons}$.

to clarify the origin of the second onset temperature $T_2^{\rm ons}$, we investigate the onset temperatures of $\chi^{(3)}$ in the single-crystalline samples with various hole concentrations. The origin of $T_2^{\rm ons}$ will be argued in the discussion section.

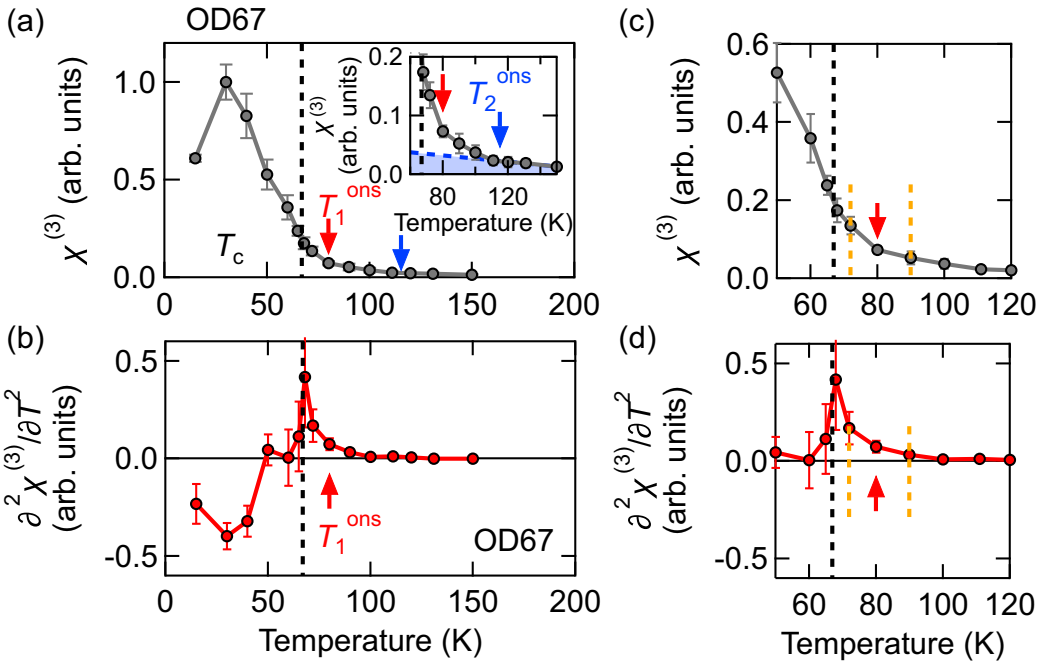

Figure 4-8: The third-order nonlinear susceptibility of the THz Kerr signal $\chi^{(3)}$ for OD67 BSCCO thin film as a function of temperature. (b) The second derivative of $\chi^{(3)}$ with respect to temperature. The vertical red arrows denote the onset temperature of the sharp increase in the THz Kerr signal $T_1^{\rm ons}$ determined from the second derivative $\partial^2\chi^{(3)}/\partial T^2$. The vertical blue arrows denote the onset temperature of the THz Kerr signal $T_2^{\rm ons}$. The inset in (a) is its expanded figure around $T_1^{\rm ons}$ and $T_2^{\rm ons}$. (c), (d) The expanded figures around $T_{\rm c}$ and $T_1^{\rm ons}$ of (a) and (b), respectively. The orange vertical dashed lines in (c) and (d) denote the error bars for $T_1^{\rm ons}$.

4.3 THz time-domain spectroscopy (THz-TDS)

4.3.1 Optical conductivity

To compare the onset temperature of the THz Kerr signal $T_1^{\rm ons}$ with that of the superconducting phase stiffness, we evaluate the superfluid density by THz-TDS in the transmission geometry. The details of the THz-TDS

measurement are described in Chapter 3. The obtained complex optical conductivity is plotted in Fig. 4-9(a)-(d). In both thin films, the imaginary part of the optical conductivity $\sigma_2(\omega)$ displays $1/\omega$-like divergent behavior below T_c, which is a signature of superconducting condensation.

4.3.2 Two-fluid model

The real and imaginary parts of the optical conductivity obtained in THz-TDS measurements are reasonably fitted by the two-fluid model, which is ascribed by [130]

$$\sigma_1(\omega) = N_s\delta(\omega) + \frac{\omega_p^2\tau}{1+\omega^2\tau^2},$$
$$\sigma_2(\omega) = \frac{N_s}{\omega} + \frac{\omega_p^2\tau^2\omega}{1+\omega^2\tau^2}, \tag{4-6}$$

where the first term represents the superconducting component, and the second term represents the Drude component. Here, N_s is the superfluid density, ω_p is the plasma angular frequency, and τ is the scattering time. The previous THz-TDS measurements and theories showed that the spectral weight is transferred from the delta function at zero frequency to the Drude component due to the inhomogeneity [129,131]. While two Drude components were assumed to reproduce the optical conductivity in Ref. [129], here to reduce the number of the fitting parameters, only one Drude component is assumed. In Figs. 4-9(a)-(d), the fitting results are shown by solid curves and well reproduce the complex optical conductivity of both samples. The temperature dependence of the three fitting parameters N_s, ω_p, and τ are exhibited in Figs. 4-9(e)-(h). The superfluid density N_s plotted in Figs. 4-9(e) and (g) sharply increases from above T_c for both films. The onset temperature of N_s is determined as $T_{Ns} = 90$ K for UD76 and $T_{Ns} = 80$ K for OD67. The onset temperature of N_s for UD76 is in good agreement with that reported in the previous THz optical conductivity measurement [25].

Next, we consider the validity of the fitting parameters ω_p and τ of the Drude component as shown in Figs. 4-9(f) and (h). Firstly, the scattering time τ displays an increasing tendency as the temperature is lowered in both samples. The temperature dependence of τ is consistent with the results reported by the THz spectroscpy [129], FTIR [132, 133], and ARPES [134], indicating that the obtained τ in this study is reasonable. To further confirm

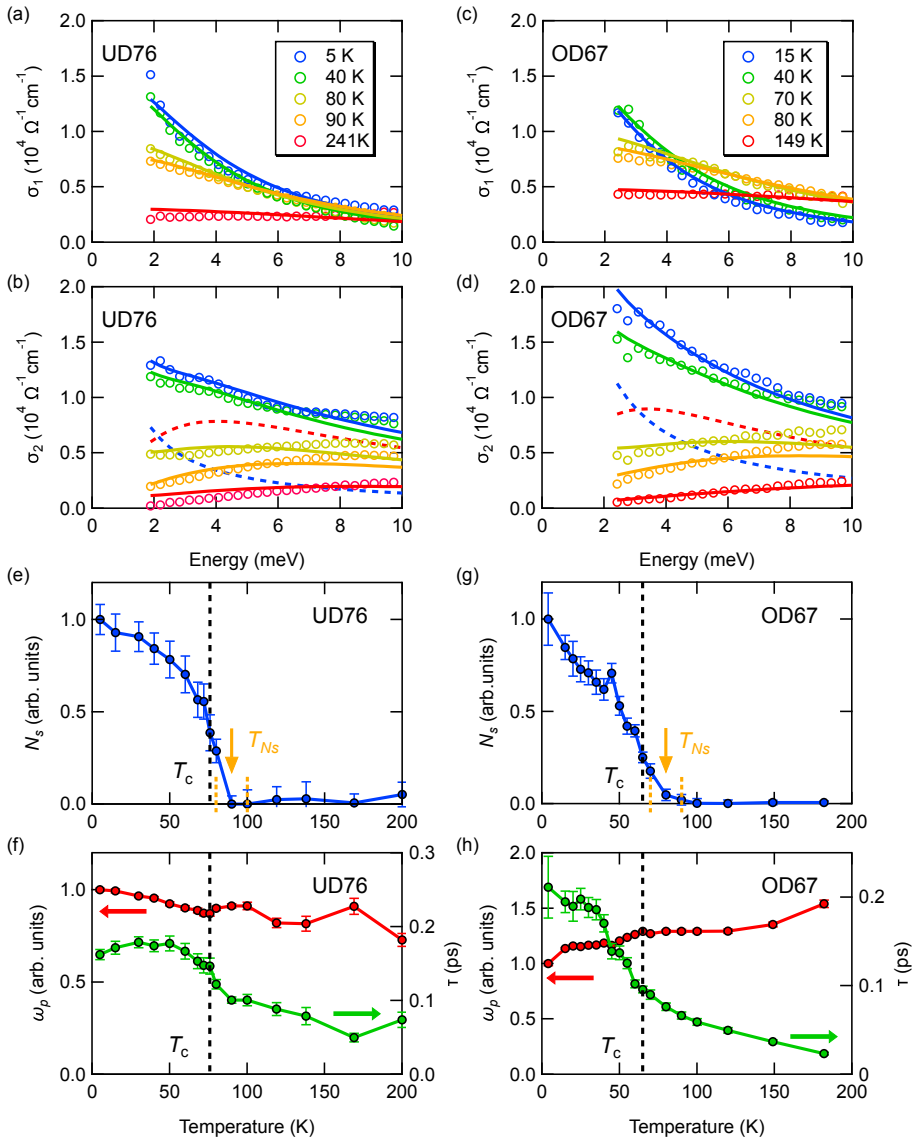

Figure 4-9: (a)-(d) Real and imaginary parts of the optical conductivity for UD76 and OD67 measured by THz-TDS. The open circles are the data, and the solid lines are the fitting curves by the two-fluid model. In (b) and (d), the dashed curves denote the superconducting component (blue) and Drude component (red) at 5 K for UD76 and at 15 K for OD67, respectively. (e)-(h) Temperature dependence of the fitting parameters in Eq. 4-6 for UD76 and OD67. (e) and (g) plot the superfluid density N_s as a function of temperature. (f) and (h) display the temperature dependence of the plasma angular frequency ω_p (red curve, left axis) and the scattering time τ (green curve, right axis). N_s and ω_p are normalized by their values at the lowest temperature (4 K). The vertical orange arrows denote the determined onset temperatures of N_s (T_{Ns}). The orange vertical dashed lines in (e) and (f) denote the error bars for T_{Ns}.

the validity of τ, we check that τ above T_c is close to the universal value given by the Planckian dissipation limit as $\hbar/\tau \sim k_B T$ [8, 135–137], which is a hallmark of the strange metal regime in cuprate superconductors. As an example, let us use the value of $\tau = 0.02$ ps for OD67 at $T = 180$ K. Considering that $1/\tau$ in Eq. (4-6) corresponds to the angular frequency, we can convert $1/\tau$ to the energy as $\hbar/\tau = 33$ meV. Since $k_B T = 15$ meV at $T = 180$ K where k_B is the Boltzmann constant, we obtain $\hbar/\tau = 2.1\ k_B T$. In the same manner, for UD76 at $T = 200$ K, we obtain $\hbar/\tau = 0.52\ k_B T$. In both samples, $\hbar/\tau$'s are the same order of magnitude as those given by the Planckian dissipation limit, confirming the validity of τ obtained by the fitting in this study.

Secondly, the plasma angular frequency ω_p shows a slight decrease below T_c for OD67 and does not show significant temperature dependence for UD76, while it is expected to decrease below T_c if the Ferrell-Glover-Tinkham (FGT) sum rule is satisfied [138,139]. This is possibly because the Drude component in the real part of the in-plane optical conductivity $\sigma_1(\omega)$ of BSCCO below 3 THz remains uncondensed below T_c, and the FGT sum rule is satisfied by the spectral weight of $\sigma_1(\omega)$ decrease at higher frequency up to 500 THz below T_c, as shown by Fourier-transform infrared spectroscopy (FTIR) [140]. Besides, the condensate spectral weight at zero frequency in $\sigma_1(\omega)$ can be transferred to a Drude component due to the spatial inhomogenuity of the superfluid density [129, 131], which results in the increase in ω_p below T_c. Therefore, we consider it is challenging to observe the decrease in the spectral weight of $\sigma_1(\omega)$ below T_c in BSCCO samples. However, we stress that the superfluid density N_s can be extracted from $\sigma_2(\omega)$, whose spectrum cannot be reproduced by a simple Drude model as discussed in the next subsection.

4.3.3 Alternative estimation of the superfluid density

To confirm the determination of N_s in a different manner, the superfluid density in $\sigma_2(\omega)$ is estimated by subtracting the Drude contribution, which corresponds to the second term of $\sigma_2(\omega)$ in Eq. (4-6). To this end, $\sigma_1(\omega)$ spectrum is first fitted by the Drude model, which can be written by the second term of $\sigma_1(\omega)$ in Eq. (4-6), as shown by the solid curves in Figs. 4-10(a) and (c). The corresponding fitting parameters of ω_p and τ are plotted as a function of temperature in Figs. 4-10(f) and (h), which are almost the same as those in Figs. 4-9(f) and (h). Then, the corresponding Drude contribution is subtracted from the experimentally obtained $\sigma_2(\omega)$ spectrum.

The subtracted spectra $\Delta\sigma_2(\omega)$ are displayed in Figs. 4-10(b) and (d). An upturn behavior toward the lower frequency range is obviously discerned even at 80 K for UD76 and at 70 K for OD67 (marked with the black arrows in Figs. 4-10(b) and (d)), indicating the presence of a superfluid component at those temperatures above T_c. On the contrary, $\Delta\sigma_2(\omega)$ at 90 K for UD76 shows a very small upturn toward the lower frequency, and that at 80 K for OD67 does not display this upturn behavior toward the lower frequency. Figures 4-10(e) and (g) show the temperature dependence of $\Delta\sigma_2(\omega)$ at the lowest frequency of 1.9 meV for UD76 and that of 2.4 meV for OD67. The onset temperatures are estimated as $T_{Ns} = 85$-95 K for UD76 and $T_{Ns} =$ 80-90 K for OD67. These values are in good agreement with those extracted by the two-fluid model, which further reinforces the determination of T_{Ns} by the two-fluid analysis. In the subtracted spectra of $\Delta\sigma_2(\omega)$, a finite peak around 8 meV is recognized, which is neither reproduced by the two-fluid model in Figs. 4-9(b) and (d). This high-frequency deviation might be due to the non-Drude behavior of cuprate superconductors.

4.4 Doping dependence of the THz Kerr signal in BSCCO bulk samples

To elucidate the hole doping dependence of $T_1^{\rm ons}$ and $T_2^{\rm ons}$, the THz Kerr signals in the BSCCO bulk samples are examined in a wide range of doping from the previous THz pump-optical probe spectroscopy results of my master course study [85]: the experiments were performed on underdoped (UD62 and UD74), optimally doped (OP90), and overdoped (OD82, OD66) single crystals. Since the temperature dependence of the THz E-field inside the sample does not strongly depend on the hole concentration, as shown in Figs. 4-6(a) and (b), the temperature dependence of the third-order nonlinear susceptibility $\chi^{(3)}$ for bulk samples is estimated by approximating the temperature dependence of the internal THz E-field with that of the UD76 thin film. In the following, we examine the temperature dependence of the THz Kerr signal for each BSCCO single crystal.

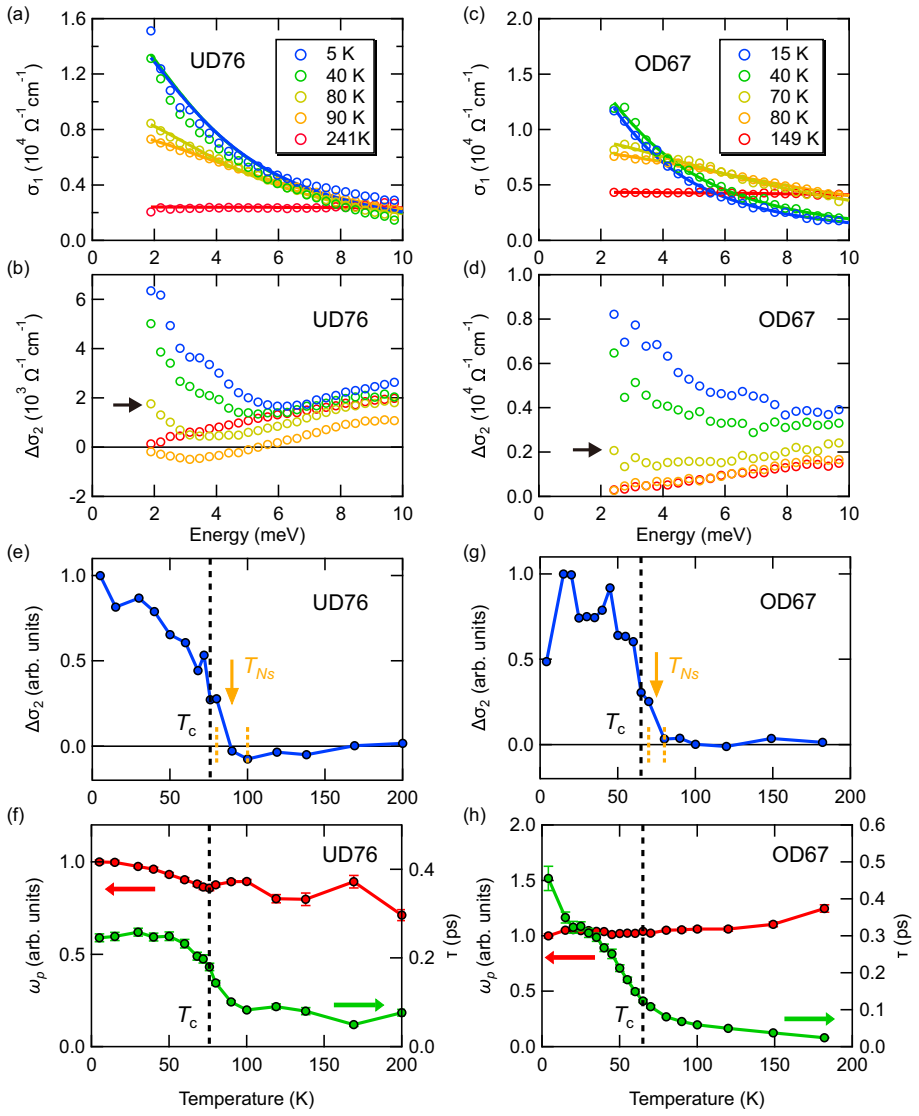

Figure 4-10: (a), (c) Real part of the optical conductivity for UD76 and OD67 measured by THz-TDS. The open circles are the data, and the solid lines are the fitting curves by the Drude model. (b), (d) The difference between the imaginary part of the optical conductivity and the Drude contribution obtained from the fits to the real part. The black horizontal arrows are described in the main text. (e), (g) Temperature dependence of $\Delta\sigma_2(\omega)$ at the lowest frequency of 1.9 meV for UD76 and that of 2.4 meV for OD67. The vertical orange arrows denote the determined onset temperature of $\Delta\sigma_2(\omega)$ (T_{Ns}). The orange vertical dashed lines in (e) and (g) denote the error bars for T_{Ns}. (f), (h) The temperature dependence of the plasma angular frequency ω_p (red curve, left axis) and the scattering time τ (green curve, right axis). N_s and ω_p are normalized by their values at the lowest temperature (4 K).

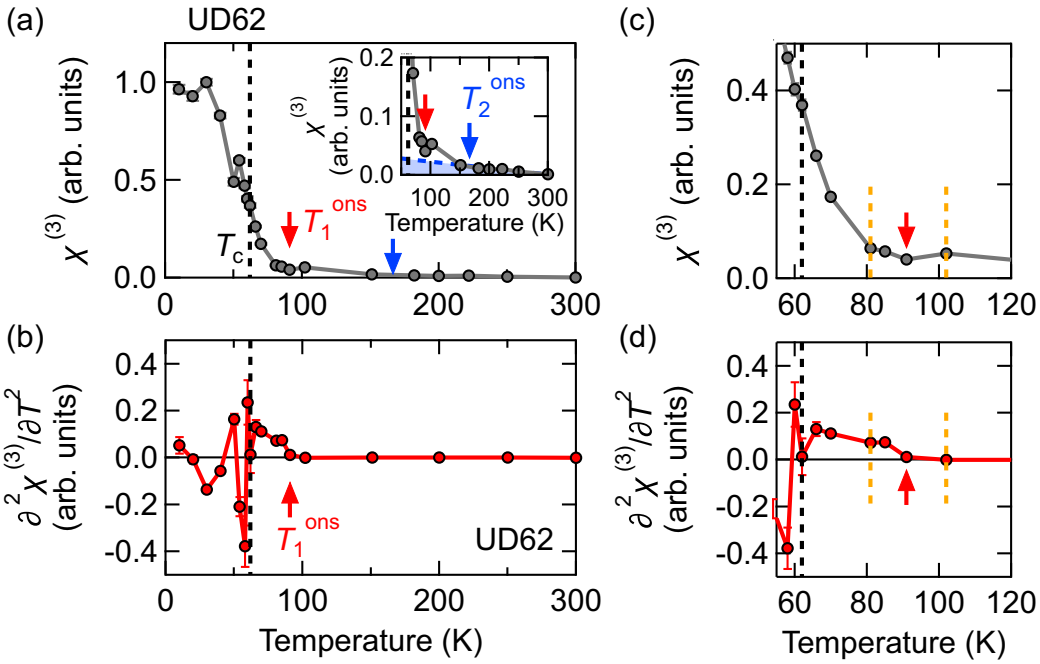

Figure 4-11: (a) The third-order nonlinear susceptibility of the THz Kerr signal $\chi^{(3)}$ for UD62 BSCCO bulk sample as a function of temperature. (b) The second derivative of $\chi^{(3)}$ with respect to temperature. The vertical red arrows denote the onset temperature of the sharp increase in the THz Kerr signal $T_1^{\rm ons}$ determined from the second derivative $\partial^2\chi^{(3)}/\partial T^2$. The vertical blue arrows denote the onset temperature of the THz Kerr signal $T_2^{\rm ons}$. The inset in (a) is its expanded figure around $T_1^{\rm ons}$ and $T_2^{\rm ons}$. (c), (d) The expanded figures around $T_{\rm c}$ and $T_1^{\rm ons}$ of (a) and (b), respectively. The orange vertical dashed lines in (c) and (d) denote the error bars for $T_1^{\rm ons}$.

UD62 BSCCO bulk sample

Figure 4-11 shows the temperature dependence of $\chi^{(3)}$ and $\partial^2\chi^{(3)}/\partial T^2$ for UD62. The nonlinear susceptibility $\chi^{(3)}$ in Fig. 4-11(c) shows an onset around 81-102 K (the orange dashed lines). Since the onset temperature of $\partial^2\chi^{(3)}/\partial T^2$ is discerned at 91 K in Fig. 4-11(d), we determine the first onset temperature as $T_1^{\rm ons} = 91$ K. In addition, one can see a change in the slope of $\chi^{(3)}$ above $T_1^{\rm ons}$ around $T_2^{\rm ons} = 166.5$ K in the inset of Fig. 4-11(a), which is in between 151 K and 182 K.

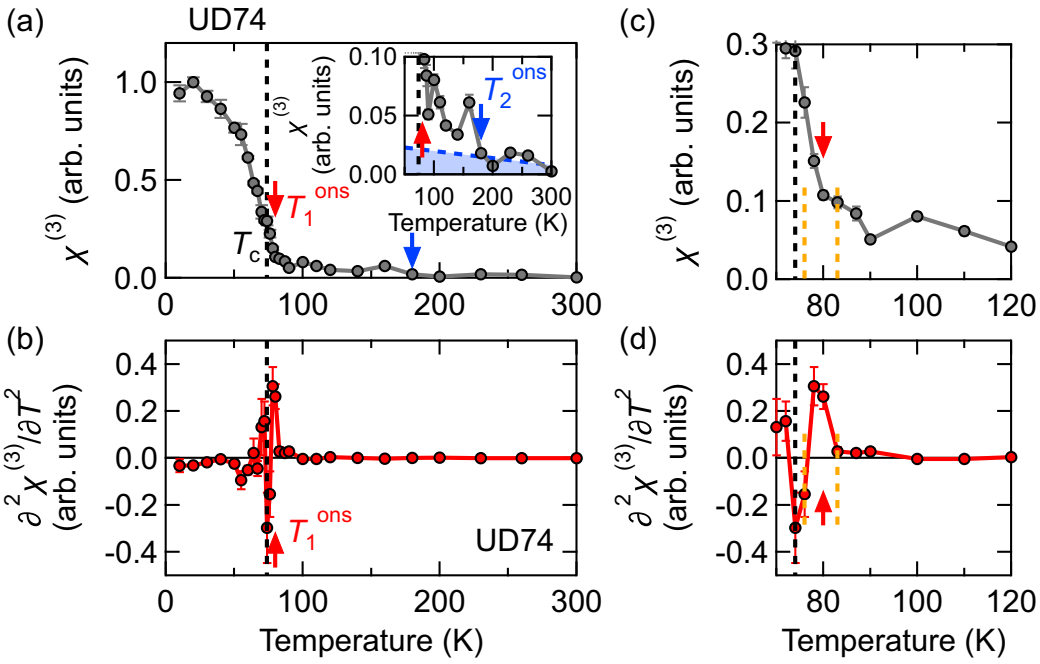

Figure 4-12: (a) The third-order nonlinear susceptibility of the THz Kerr signal $\chi^{(3)}$ for UD74 BSCCO bulk sample as a function of temperature. (b) The second derivative of $\chi^{(3)}$ with respect to temperature. The vertical red arrows denote the onset temperature of the sharp increase in the THz Kerr signal $T_1^{\rm ons}$ determined from the second derivative $\partial^2\chi^{(3)}/\partial T^2$. The vertical blue arrows denote the onset temperature of the THz Kerr signal $T_2^{\rm ons}$. The inset in (a) is its expanded figure around $T_1^{\rm ons}$ and $T_2^{\rm ons}$. (c), (d) The expanded figures around $T_{\rm c}$ and $T_1^{\rm ons}$ of (a) and (b), respectively. The orange vertical dashed lines in (c) and (d) denote the error bars for $T_1^{\rm ons}$.

UD74 BSCCO bulk sample

Figure 4-12 shows the temperature dependence of the THz Kerr signal for UD74. As shown in Fig. 4-12(c), $\chi^{(3)}$ displays a sharp increase below 80 K. One can also identify an onset of $\partial^2\chi^{(3)}/\partial T^2$ in Fig. 4-12(d). Therefore, we determine $T_1^{\rm ons} = 80$ K for UD74 sample. In the inset of Fig. 4-12(a), the slope of $\chi^{(3)}$ increases below $T_2^{\rm ons} = 180$ K.

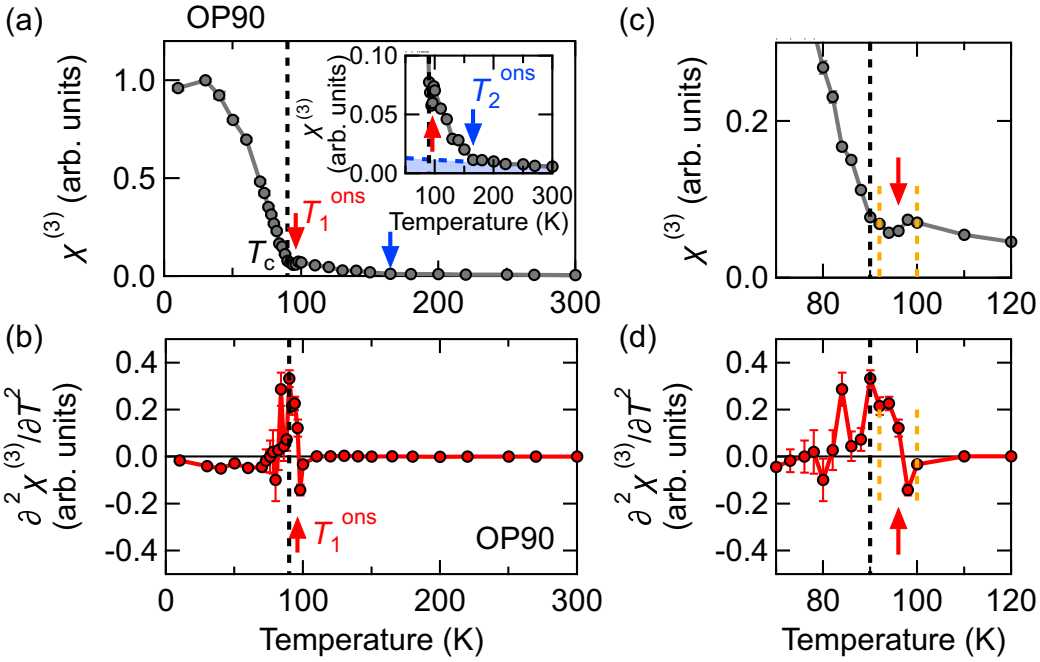

Figure 4-13: (a) The third-order nonlinear susceptibility of the THz Kerr signal $\chi^{(3)}$ for OP90 BSCCO bulk sample as a function of temperature. (b) The second derivative of $\chi^{(3)}$ with respect to temperature. The vertical red arrows denote the onset temperature of the sharp increase in the THz Kerr signal $T_1^{\rm ons}$ determined from the second derivative $\partial^2\chi^{(3)}/\partial T^2$. The vertical blue arrows denote the onset temperature of the THz Kerr signal $T_2^{\rm ons}$. The inset in (a) is its expanded figure around $T_1^{\rm ons}$ and $T_2^{\rm ons}$. (c), (d) The expanded figures around $T_{\rm c}$ and $T_1^{\rm ons}$ of (a) and (b), respectively. The orange vertical dashed lines in (c) and (d) denote the error bars for $T_1^{\rm ons}$.

OP90 BSCCO bulk sample

In Fig. 4-13, we plot the temperature dependence of $\chi^{(3)}$ and $\partial^2\chi^{(3)}/\partial T^2$ for OP90. As displayed In Fig. 4-13(c), $\chi^{(3)}$ increases below 98 K. This onset is also observed in $\partial^2\chi^{(3)}/\partial T^2$, as shown in Fig. 4-13(d). Thus, we determine the first onset temperature of $\chi^{(3)}$ for OP90 as $T_1^{\rm ons} = 98$ K. Above $T_1^{\rm ons}$, a change in the slope of $\chi^{(3)}$ is observed around $T_2^{\rm ons} = 165$ K in the inset of Fig. 4-13(a).

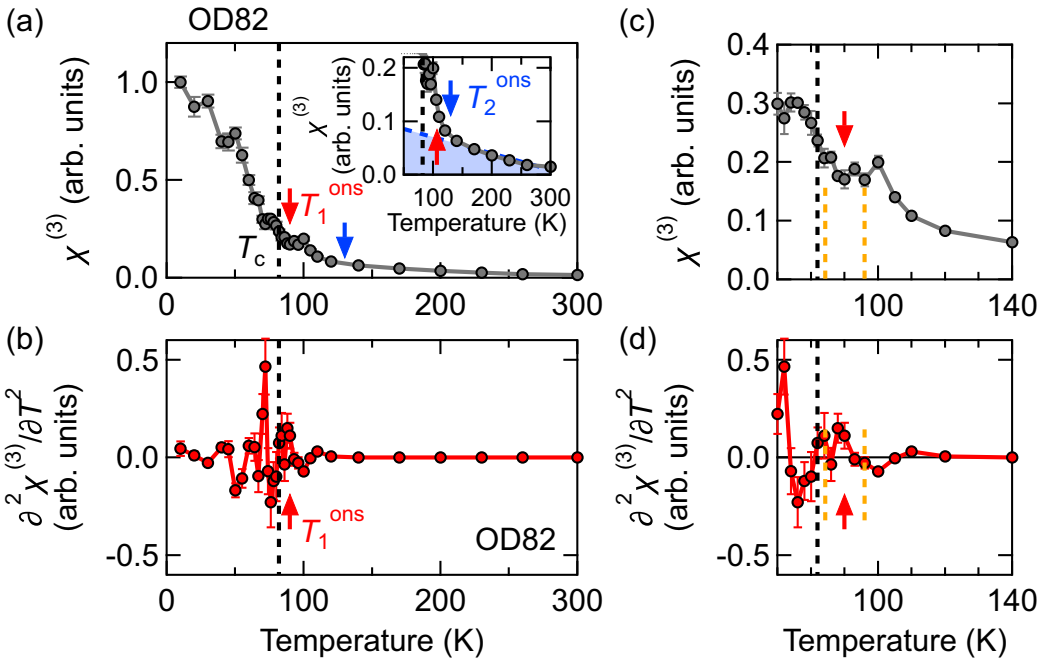

Figure 4-14: (a) The third-order nonlinear susceptibility of the THz Kerr signal $\chi^{(3)}$ for UD62 BSCCO bulk sample as a function of temperature. (b) The second derivative of $\chi^{(3)}$ with respect to temperature. The vertical red arrows denote the onset temperature of the sharp increase in the THz Kerr signal $T_1^{\rm ons}$ determined from the second derivative $\partial^2\chi^{(3)}/\partial T^2$. The vertical blue arrows denote the onset temperature of the THz Kerr signal $T_2^{\rm ons}$. The inset in (a) is its expanded figure around $T_1^{\rm ons}$ and $T_2^{\rm ons}$. (c), (d) The expanded figures around T_c and $T_1^{\rm ons}$ of (a) and (b), respectively. The orange vertical dashed lines in (c) and (d) denote the error bars for $T_1^{\rm ons}$.

OD82 BSCCO bulk sample

Figure 4-14 shows the THz Kerr signal for OD82 as a function of temperature. As plotted in Fig. 4-14(c), $\chi^{(3)}$ shows an onset around 84-96 K, which is denoted by the orange dashed lines, while the sharp increasing tendency is less clear compared to the UD and OP samples. However, the corresponding onset temperature of 90 K can be seen in $\partial^2\chi^{(3)}/\partial T^2$, as displayed in 4-14(d). Thus, we determine the first onset temperature as $T_1^{\rm ons} = 90$ K.

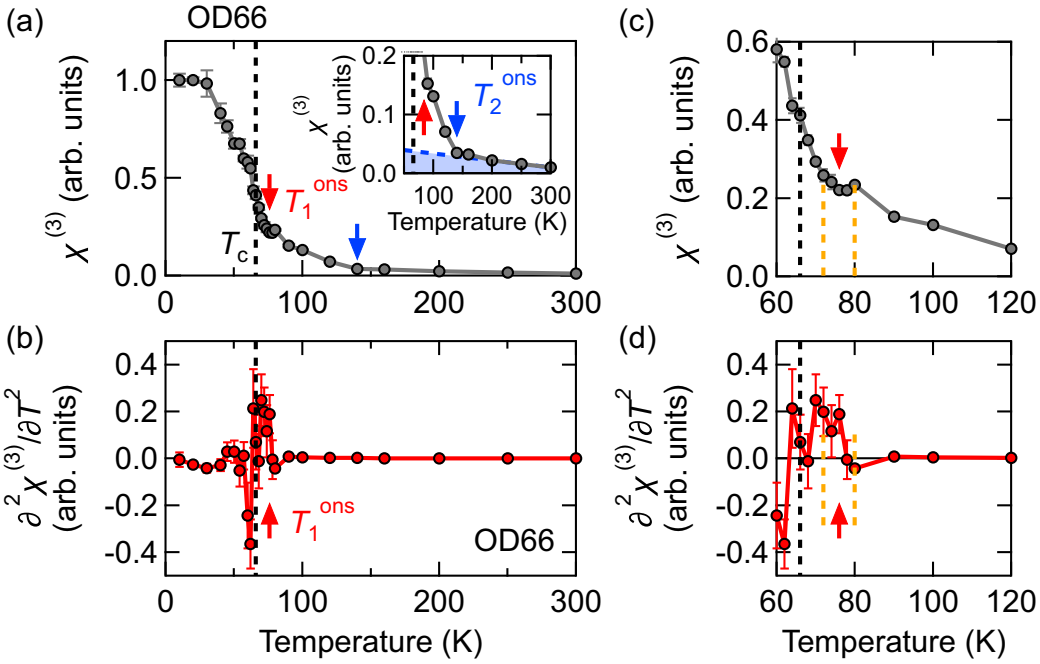

Figure 4-15: (a) The third-order nonlinear susceptibility of the THz Kerr signal $\chi^{(3)}$ for OD66 BSCCO bulk sample as a function of temperature. (b) The second derivative of $\chi^{(3)}$ with respect to temperature. The vertical red arrows denote the onset temperature of the sharp increase in the THz Kerr signal $T_1^{\rm ons}$ determined from the second derivative $\partial^2\chi^{(3)}/\partial T^2$. The vertical blue arrows denote the onset temperature of the THz Kerr signal $T_2^{\rm ons}$. The inset in (a) is its expanded figure around $T_1^{\rm ons}$ and $T_2^{\rm ons}$. (c), (d) The expanded figures around $T_{\rm c}$ and $T_1^{\rm ons}$ of (a) and (b), respectively. The orange vertical dashed lines in (c) and (d) denote the error bars for $T_1^{\rm ons}$.

In addition, one can see a change in the slope of $\chi^{(3)}$ around $T_2^{\rm ons} = 130$ K in the inset of Fig. 4-14(a), which is in between 120 K and 140 K.

OD66 BSCCO bulk sample

Figure 4-15 shows the temperature dependence of the THz Kerr signal for OD66. As shown in Fig. 4-15(c), $\chi^{(3)}$ displays a sharp increase between 72 K and 80 K. One can also identify the corresponding onset of $\partial^2\chi^{(3)}/\partial T^2$ at 76 K in Fig. 4-15(d). Therefore, we determine $T_1^{\rm ons} = 76$ K for OD66 sample. In the inset of Fig. 4-15(a), the slope of $\chi^{(3)}$ increases below $T_2^{\rm ons} = 140$ K.

4.5 Discussion

Figure 4-16 summarizes $T_1^{\rm ons}$ and $T_2^{\rm ons}$ for two thin films and five bulk samples as a function of doping. Here, we determine the hole concentration p using the Presland-Tallon's equation [141]:

$$1 - \frac{T_{\rm c}}{T_{\rm c}^{\rm max}} = 82.6(p - 0.16)^2, \tag{4-7}$$

where $T_{\rm c}^{\rm max}$ is $T_{\rm c}$ at the OP sample. In the following, we discuss the origins of these onset temperatures.

4.5.1 Origin of the onset temperature $T_1^{\rm ons}$

First, in both UD76 and OD67 BSCCO thin films, $T_1^{\rm ons}$ in the THz Kerr signal shows a good agreement with T_{Ns} in the superfluid density within the experimental error bars. This coincidence suggests that although the static superconducting phase coherence develops at $T_{\rm c}$, the THz probe is sensitive to the evolution of superconducting phase coherence fluctuating on the picosecond time scale which evolves from slightly above $T_{\rm c}$.

Figure 4-16 summarizes $T_1^{\rm ons}$ for two thin films and five bulk samples as a function of doping. For all the samples examined, the onset temperature of the Higgs mode $T_1^{\rm ons}$ lies slightly above $T_{\rm c}$. This result is consistent with the previously reported THz conductivity measurements in UD BSCCO thin films [25,26]. Similar behavior has also been reported in other cuprate superconductors such as $La_{2-x}Sr_xCuO_4$ (LSCO) and $YBa_2Cu_3O_{6+y}$ (YBCO): the onset temperature of the macroscopic superconducting phase fluctuation is shown to locate at most 20 K above $T_{\rm c}$ in a wide range of hole concentration when probed by microwave and THz spectroscopy [27–29, 31].

4.5.2 Origin of the onset temperature $T_2^{\rm ons}$

To explore the origin of the second onset temperature of the THz Kerr signal $T_2^{\rm ons}$, $T_2^{\rm ons}$ for all the samples studied are shown as a function of hole concentration in Fig. 4-16. It is evident that except for OD66, $T_2^{\rm ons}$ coincides with the local gap opening temperature reported in STM studies below which local superconducting patches emerge [41]. This coincidence suggests that $T_2^{\rm ons}$ is relevant to the gap opening in local superconducting patches, whereas the reason why $T_2^{\rm ons}$ of only OD66 deviates from the gap opening temperature

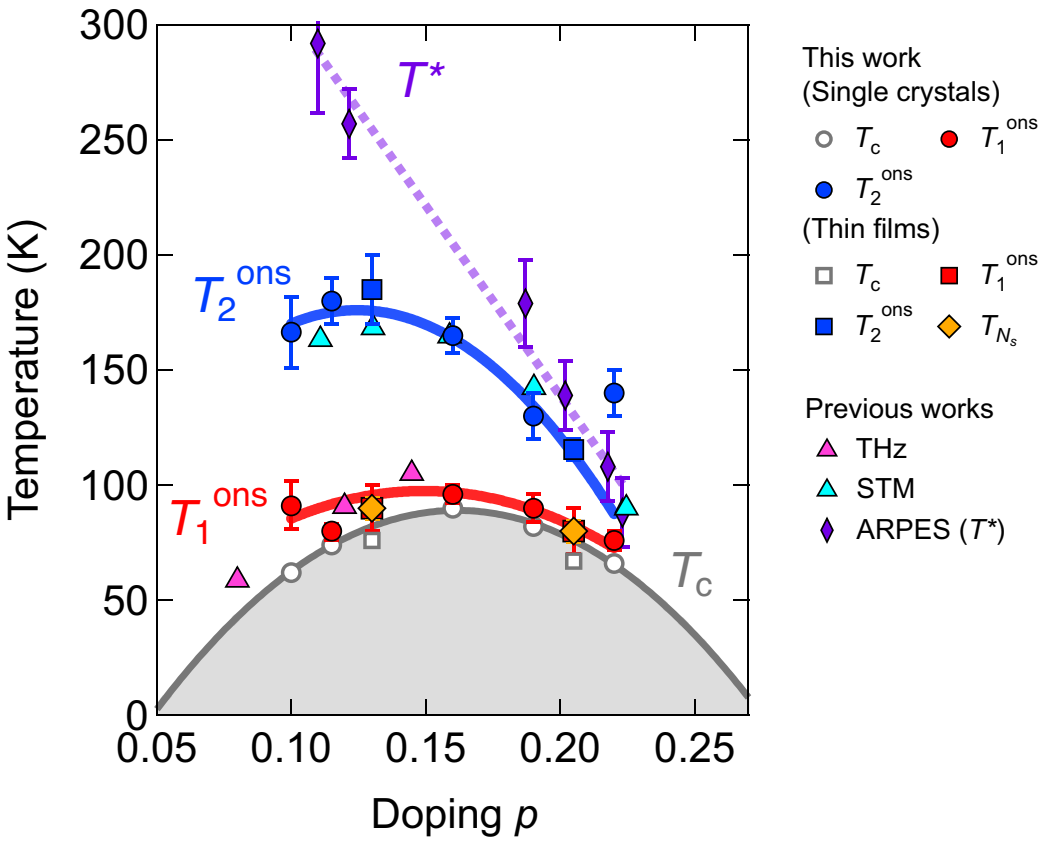

Figure 4-16: The onset temperature of the THz Kerr signal as a function of doping obtained from THz pump-optical probe spectroscopy and superfluid density evaluated by THz-TDS. The hole concentration p is estimated from T_c using the Presland and Tallon's equation in Eq. (4-7) [141]. The red and blue circles are T_1^{ons} and T_2^{ons} for BSCCO bulk samples evaluated from the data in Ref. [85]. The red and blue squares are T_1^{ons} and T_2^{ons} for BSCCO thin films studied here. The orange diamonds are the onset temperature of the superfluid density T_{Ns} for BSCCO thin films obtained by THz-TDS. The data of T_{Ns} for other hole concentrations plotted by magenta triangles are adopted from Ref. [25]. The light blue triangles denote the superconducting gap opening temperature for BSCCO adopted from Ref. [41]. The purple diamonds denote the pseudogap opening temperature T^* for BSCCO adopted from Ref. [118, 119].

in STM is unresolved. Previous studies in BSCCO from ARPES [43–45] and Nernst [36] measurements also demonstrate that the superconducting gap opening temperature is considerably higher than T_c, yet the values are distributed between T_1^{ons} and T_2^{ons} depending on the measurements. In addition, T_2^{ons} is substantially lower than the pseudogap opening temperature T^* in particular for the underdoped samples. This may indicate that in particular for the underdoped region, the preformed Cooper paring is not directly related to the pseudogap.

In other cuprates such as YBCO and LSCO, it has been shown that local superconducting patches appear at as high as 100 K above T_c by infrared spectroscopy [32–34] and Nernst measurements [35]. It is noteworthy that the two temperature scales of T_1^{ons} and T_2^{ons} have also been recognized in the FTIR studies for YBCO [33, 34], and they are in good agreement with those identified in the THz Kerr signal for BSCCO even though the materials are different. Like the previous FTIR studies for YBCO [33, 34], the growth of local superconducting patches below T_2^{ons} should also be identified in the THz-TDS measurements. Nevertheless, it is absent in the present results for BSCCO. This difference between FTIR and THz-TDS measurements might be due to the sensitivity to the superfluid density N_s: in the previous FTIR of Ref. [34], N_s above T_1^{ons} is 0.2-0.3% of that at the lowest temperature, whereas the error bars for N_s in our THz optical conductivity is estimated as 5-10% of the value at the lowest temperature. Therefore, even though the value of N_s above T_1^{ons} cannot be directly compared between BSCCO and YBCO, it is possible that a finite N_s above T_1^{ons} is below the noise floor in our THz-TDS measurement.

Furthermore, it has been recently reported that the macroscopic superconducting phase coherence vanishes rapidly above T_c in an exponential fashion by paraconductivity, nonlinear conductivity, and torque magnetometry measurements [40, 142, 143]. In these studies, the mechanism of the superconducting phase-locking among the locally formed superconducting islands is explained by a phenomenological percolation model. These observations suggest that the origin of the THz Kerr signal between T_1^{ons} and T_2^{ons} deserves further experimental investigations and requires a microscopic theory of the THz Kerr effect in the temperature regime of precursor superconductivity.

To summarize, we identify two onset temperatures in the THz Kerr signal of the BSCCO samples for a wide range of doping: the first one ($T_1^{\rm ons}$) is located slightly above $T_{\rm c}$, whereas the second one ($T_2^{\rm ons}$) is located substantially higher than $T_{\rm c}$. We find that $T_1^{\rm ons}$ coincides with that of the superfluid density evaluated from the THz optical conductivity measurements. This coincidence indicates that the superconducting phase fluctuation on the picosecond time scale evolves from slightly above $T_{\rm c}$. Furthermore, the second onset temperatures $T_2^{\rm ons}$'s for all the samples studied, except for OD66 sample, show a good agreement with the superconducting gap opening temperatures in the previous studies of BSCCO [36, 41, 43]. This agreement suggests that $T_2^{\rm ons}$ is reasonably ascribed to the preformed Cooper pairs far above $T_{\rm c}$. Moreover, particularly for the underdoped samples ($p < 0.16$), $T_2^{\rm ons}$ is located substantially lower than the pseudogap opening temperature T^*, suggesting that the origin of the pseudogap is not directly correlated with the preformed Cooper pairing.

Chapter 5

Optical pump-THz probe spectroscopy for $YBa_2Cu_3O_{6+y}$

本章については、5 年以内に雑誌等で刊行予定のため、非公開。

Chapter 6

THz pump-optical probe spectroscopy for $YBa_2Cu_3O_{6+y}$

本章については、5 年以内に雑誌等で刊行予定のため、非公開。

Chapter 7

THz third-harmonic generation in $YBa_2Cu_3O_{6+y}$

本章については、5 年以内に雑誌等で刊行予定のため、非公開。

Chapter 8

Summary and outlook

In this study, we have explored the superconducting fluctuations and the photo-induced nonequilibrium superconductivity via the THz nonlinear optical responses arising from the collective excitation of the superconducting order parameter in high-T_c cuprate superconductors; the Higgs mode and the Josephson plasma resonance (JPR).

Superconducting fluctuations in $Bi_2Sr_2CaCu_2O_{8+x}$

Firstly, we have investigated the in-plane Higgs-mode response through the observation of the THz Kerr effect in the *ab*-plane $Bi_2Sr_2CaCu_2O_{8+x}$ (BSCCO) thin films utilizing the THz pump-optical probe spectroscopy. We observe the induced oscillation, i.e., the THz Kerr signal, in the THz-pump induced in-plane reflectivity change which follows the squared THz electric field. In the THz Kerr signal, two onset temperatures are identified. Combining the results of single-crystalline samples, we have found that the first one ($T_1^{\rm ons}$) is slightly above T_c, whereas the second one ($T_2^{\rm ons}$) is located substantially higher than T_c. $T_1^{\rm ons}$ coincides with that of the superfluid density evaluated from the THz optical conductivity, suggesting that although the static superconducting phase coherence develops below T_c, the THz probe is sensitive to the superconducting phase fluctuation on the picosecond time scale which evolves from slightly above T_c. Notably, the second onset temperature $T_2^{\rm ons}$'s for all the samples studied, except for OD66 sample, coincide with the superconducting gap opening temperatures in the previous studies of BSCCO [36, 41, 43]. This coincidence indicates that $T_2^{\rm ons}$ is reasonably associated with the preformed Cooper pairs far above T_c. Furthermore, par-

ticularly in underdoped samples ($p < 0.16$), $T_2^{\rm ons}$ is much lower than the pseudogap opening temperature T^*, which may indicate that in the underdoped region, the pseudogap is not directly relevant to the preformed Cooper paring.

Photo-induced nonequilibrium optical responses in $YBa_2Cu_3O_{6+y}$

Secondly, we have applied the THz nonlinear optical responses to elucidate the optically-induced nonequilibrium superconductivity. To this end, we have started from the optical pump-THz probe spectroscopy for the *ac*-plane underdoped $YBa_2Cu_3O_{6+y}$ single crystal (UD61) with three pump wavelengths: 800 nm, 1.5 μm, and 14 μm. We have observed the photo-induced $1/\omega$-like increase in the imaginary part of the *c*-axis optical conductivity above T_c, consistent with the previous studies [53–57]. On the contrary, a photo-induced decrease in the *a*-axis THz reflectivity is discerned, which is incompatible with the interpretation of the photo-induced superconductivity.

Next, the observed transient optical conductivity is examined by the in-plane Higgs-mode response by THz pump-optical probe spectroscopy for the *ab*-plane underdoped $YBa_2Cu_3O_{6+y}$ single crystal (UD78). We have identified the THz-pulse driven Higgs mode and the superconducting quasiparticle (QP) excitation below T_c in the THz-pump induced in-plane optical reflectivity change $\Delta R/R$. When the sample is irradiated with the pump pulse at the wavelength of 1.4 μm below T_c, the Higgs-mode and QP responses are suppressed, consistent with the photo-induced destruction of the superconductivity. Above T_c, neither the Higgs mode nor the QP responses are observed in $\Delta R/R$, indicating that it is unlikely to attribute the photo-induced state above T_c to the superconducting phase.

To further examine the photo-induced state above T_c, we have investigated the THz third-harmonic generation (THG) from the *c*-axis Josephson current for the *ac*-plane UD61 YBCO sample. Using the narrowband THz-pulse polarized along the *c*-axis with the central frequency of 0.5 THz, we have observed the THG at 1.5 THz in the reflected THz electric field from UD61 below T_c. Besides, we have performed the 800-nm pump-THG probe experiments and shown that the THG intensity below T_c decreases after photo-excitation, consistent with the results of the Higgs-mode response. At 100 K, the THG is not identified either in equilibrium or in the photo-induced

state.

Therefore, we have concluded that the optically-induced increase in the imaginary part of the c-axis optical conductivity is attributed to the QP excitation but not to the photo-induced superconductivity. Since the temperature range where the characteristic c-axis transient conductivity emerges agrees with the pseudogap temperature region, the observed nonequilibrium response is most likely ascribed to the QP excitation across the pseudogap. Even though the photo-induced state is not attributed to the superconductivity, it is highly intriguing that coherent QPs with the scattering rate as low as a few THz appear right after the photo-excitation in the pseudogap region, considering the incoherent c-axis transport in equilibrium. By investigating the time evolution of the scattering rate of the transient Drude-like response with a broader probe frequency range, one can understand what interacts with the photo-excited pseudogap QPs on the picosecond timescale, which might give a clue to understanding the pseudogap phase.

Outlook

As an initial step, we have investigated the superconducting fluctuations in high-T_c cuprate superconductors utilizing the Higgs-mode response by the nonlinear THz excitation. This measurement method demonstrated here would provide access for the study of dynamical interplay between the superconductivity and other competing or coexisting orders in unconventional superconductors though the observation of the collective modes arising from those orders in the time domain.

In addition, the Higgs mode in cuprate superconductors is still in its infancy and deserves to be further investigated. Meanwhile, the observations of the Higgs mode in cuprates are limited to the THz pulse excitation with a photon energy around 2.5 meV, which is much smaller than the superconducting gap energy at the antinode in BSCCO and YBCO [186]. Therefore, to reveal the energy spectrum of the Higgs mode, the mid-infrared pulse excitation whose photon energy reaches to the antinodal superconducting gap is promising in the future study.

Subsequently, we have studied the nonequilibrium dynamics of YBCO using the THz reflectivity along the c-axis as a probe. We show that the multilayer analysis to extract the optically-induced surface refractive index gives a significant artifact in the superconducting state. In this regard, it is desired to use ac-plane thin film samples to study the nonequilibrium c-

axis optical response to overcome the penetration depth mismatch between the pump and probe pulses. Combining the nonequilibrium c-axis optical response above T_c, this study might enable us to investigate the relation between the superconductivity and the pseudogap.

Finally, we have then studied the light-induced nonequilibrium state in cuprate superconductors by applying the THz nonlinear responses of the Higgs mode and JPR. As an ultrafast probe of the superconducting order parameter, these THz nonlinear responses would lay the foundation to explore the nonequilibrium phenomena.

Appendix A

Supplemental data of the THz pump-optical probe spectroscopy for $Bi_2Sr_2CaCu_2O_{8+x}$

In Chapter 4, we have used the $Bi_2Sr_2CaCu_2O_{8+x}$ (BSCCO) films of different thicknesses due to the limited availability of high quality BSCCO thin films grown on MgO. However, in this appendix, we show the film thickness d_{Film} does not affect the result of the THz pump-optical probe spectroscopy (TPOP) experiment.

The penetration depth δ at the frequency ω is given by [130]

$$\delta = \frac{c}{2\kappa(\omega)\omega}. \tag{A.1}$$

Here, c is the speed of light and $\kappa(\omega)$ is the imaginary part of the refractive index of the film. First, let us consider the penetration depth of the near-infrared(NIR) probe δ_{NIR}. By using the dielectric function for underdoped (T_{c} = 66 K) and optimally doped (T_{c} = 88 K) BSCCO single crystal at 1.55 eV given by Ref. [187], the penetration depth for the near-infrared (NIR) probe, δ_{NIR}, is calculated as 198 nm for underdoped sample at 20 K and 190 nm for optimally doped sample at 15 K, indicating that δ_{NIR} does not strongly depend on doping. We also estimated δ_{NIR} for optimally doped BSCCO single crystal (T_{c} = 88 K) to be 186 nm at 15 K and 178 nm at 200 K using the dielectric function given in Ref. [188] indicating that δ_{NIR} does not strongly

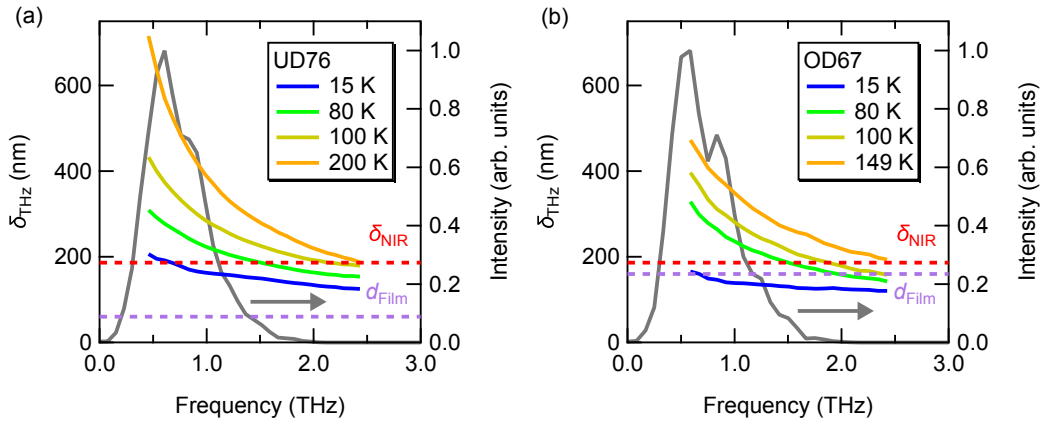

Figure A.1: The penetration depth of the THz-pump E-field (δ_{THz}) at the indicated temperatures for (a) UD76 and (b) OD67. The THz-pump power spectrum is also shown by a gray curve. The red dotted horizontal lines are the penetration depth of the NIR-probe E-field (δ_{NIR}) at 30 K calculated by using the data in Ref. [188]. The purple dotted horizontal lines denote the thickness of each film.

depend on temperature. Since δ_{NIR} is substantially larger than the thickness of each film d_{Film} (60 nm for UD76 and 160 nm for OD67, respectively), the NIR-probe E-field experiences a part of the MgO substrate. However, the contribution from the substrate to the THz Kerr signal is negligible as discussed below.

The THz-pump induced reflectivity change at 800 nm for MgO substrate can be written similarly as Eq. (4-1) in Chapter 4 as [121]

$$\frac{\Delta R}{R} = \frac{\partial R}{\partial n} c\varepsilon_0 n_2 E_{\mathrm{pump}}^2, \tag{A.2}$$

where n is the refractive index of MgO at 800 nm, n_2 is the second order nonlinear refractive index of MgO for the THz-pump 800-nm probe measurement and E_{pump} is the peak THz-pump E-field. At room temperature, the refractive index of MgO at 800 nm is $n = 1.72$ [189], and the second order nonlinear refractive index of MgO for 1-THz pump 800-nm probe measurement is $n_2 = 0.5\times10^{-16}$ cm^2/W [190]. For $E_{\mathrm{pump}} = 400$ kV/cm, which is the maximum peak E-field in our experiments, the reflectivity change can be calculated from Eq. (A.2) as $\Delta R/R = 3.0\times10^{-9}$. This value is negligibly small compared to the observed $\Delta R/R$ for BSCCO which is the order of 10^{-4}

in the normal state. Thus we can neglect the effect of the substrate in the pump-probe signal.

Next, we estimate the penetration depth of the THz pump, δ_{THz}, from the measured THz optical conductivity in Figs. 4-9(a)-(d). The results are represented in Fig. A.1. Since the power spectrum of THz-pump has the main portion below 1 THz, we focus on the behavior of δ_{THz} below 1 THz. One can see that δ_{THz} is substantially larger than d_{Film}. This indicates that the effect of the THz pump is homogeneous along the depth direction of the film. Therefore, we conclude that the difference of the thickness of the film does not affect the experimental results.

Appendix B

Effective optical response calculated from the stack of thin layers

本章については、5 年以内に雑誌等で刊行予定のため、非公開。

Appendix C

Fitting parameter dependence of the THz reflectivity change along the a-axis of $YBa_2Cu_3O_{6+y}$ in optical pump-THz probe spectroscopy

本章については、5 年以内に雑誌等で刊行予定のため、非公開。

Bibliography

[1] H. K. Onnes, "The disappearance of the resistivity of mercury", *Communicatie Leiden*, **120b,122b,124c**, (1911).

[2] L. Bardeen, L. Cooper, and J. Schrieffer, "Superconductivity theory", *Physical Review*, **108**, 1175, (1957).

[3] J. G. Bednorz and K. A. Müller, "Possible high T_c superconductivity in the Ba-La-Cu-O system", *Zeitschrift für Physik B Condensed Matter*, **64**, 189–193, (1986).

[4] C. C. Tsuei and J. R. Kirtley, "Pairing symmetry in cuprate superconductors", *Reviews of Modern Physics*, **72**, 969–1016, (2000).

[5] B. Keimer, S. A. Kivelson, M. R. Norman, S. Uchida, and J. Zaanen, "From quantum matter to high-temperature superconductivity in copper oxides", *Nature*, **518**, 179–186, (2015).

[6] I. M. Vishik, "Photoemission perspective on pseudogap, superconducting fluctuations, and charge order in cuprates: a review of recent progress", *Reports on Progress in Physics*, **81**, 062501, (2018).

[7] N. Doiron-Leyraud, C. Proust, D. LeBoeuf, J. Levallois, J. B. Bonnemaison, R. Liang, D. A. Bonn, W. N. Hardy, and L. Taillefer, "Quantum oscillations and the Fermi surface in an underdoped high-T_c superconductor", *Nature*, **447**, 565–568, (2007).

[8] C. Proust and L. Taillefer, "The Remarkable Underlying Ground States of Cuprate Superconductors", *Annual Review of Condensed Matter Physics*, **10**, 409–429, (2019).

[9] L. Taillefer, "Scattering and Pairing in Cuprate Superconductors", *Annual Review of Condensed Matter Physics*, **1**, 51–70, (2010).

[10] M. Takigawa, A. P. Reyes, P. C. Hammel, J. D. Thompson, R. H. Heffner, Z. Fisk, and K. C. Ott, "Cu and O NMR studies of the magnetic properties of $YBa_2Cu_3O_{6.63}$ (T_c = 62 K)", *Physical Review B*, **43**, 247–257, (1991).

[11] T. Timusk and B. Statt, "The pseudogap in high-temperature superconductors: An experimental survey", *Reports on Progress in Physics*, **62**, 61–122, (1999).

[12] H. Ding, T. Yokoya, J. C. Campuzano, T. Takahashi, M. Randeria, M. R. Norman, T. Mochiku, K. Kadowaki, and J. Giapintzakis, "Spectroscopic evidence for a pseudogap in the normal state of underdoped high-T_c superconductors", *Nature*, **382**, 51–54, (1996).

[13] A. G. Loeser, Z. X. Shen, D. S. Dessau, D. S. Marshall, C. H. Park, P. Fournier, and A. Kapitulnik, "Excitation gap in the normal state of underdoped $Bi_2Sr_2CaCu_2O_{8+\delta}$", *Science*, **273**, 325–329, (1996).

[14] D. S. Marshall, D. S. Dessau, A. G. Loeser, C. H. Park, A. Y. Matsuura, J. N. Eckstein, I. Bozovic, P. Fournier, A. Kapitulnik, W. E. Spicer, and Z. X. Shen, "Unconventional electronic structure evolution with hole doping in $Bi_2Sr_2CaCu_2O_{8+\delta}$: Angle-resolved photoemission results", *Physical Review Letters*, **76**, 4841–4844, (1996).

[15] A. Kaminski, S. Rosenkranz, H. M. Fretwell, J. C. Campuzano, Z. Li, H. Raffy, W. G. Cullen, H. You, C. G. Olson, C. M. Varma, and H. Höchst, "Spontaneous breaking of time-reversal symmetry in the pseudogap state of a high-T_c superconductor", *Nature*, **416**, 610–613, (2002).

[16] H. Mook, Y. Sidis, B. Fauqué, V. Balédent, and P. Bourges, "Observation of magnetic order in a superconducting $YBa_2Cu_3O_{6.6}$ single crystal using polarized neutron scattering", *Physical Review B*, **78**, 020506, (2008).

[17] J. Xia, E. Schemm, G. Deutscher, S. A. Kivelson, D. A. Bonn, W. N. Hardy, R. Liang, W. Siemons, G. Koster, M. M. Fejer, and A. Kapitulnik, "Polar kerr-effect measurements of the high-temperature $YBa_2Cu_3O_{6+x}$ superconductor: Evidence for broken symmetry near the pseudogap temperature", *Physical Review Letters*, **100**, (2008).

[18] M. J. Lawler, K. Fujita, J. Lee, A. R. Schmidt, Y. Kohsaka, C. K. Kim, H. Eisaki, S. Uchida, J. C. Davis, J. P. Sethna, and E. A. Kim, "Intra-unit-cell electronic nematicity of the high-T_c copper-oxide pseudogap states", *Nature*, **466**, 347–351, (2010).

[19] R. H. He, M. Hashimoto, H. Karapetyan, J. D. Koralek, J. P. Hinton, J. P. Testaud, V. Nathan, Y. Yoshida, H. Yao, K. Tanaka, W. Meevasana, R. G. Moore, D. H. Lu, S. K. Mo, M. Ishikado, H. Eisaki, Z. Hussain, T. P. Devereaux, S. A. Kivelson, J. Orenstein, A. Kapitulnik, and Z. X. Shen, "From a single-band metal to a high-temperature superconductor via two thermal phase transitions", *Science*, **331**, 1579–1583, (2011).

[20] Y. Sato, S. Kasahara, H. Murayama, Y. Kasahara, E.-G. Moon, T. Nishizaki, T. Loew, J. Porras, B. Keimer, T. Shibauchi, and Y. Matsuda, "Thermodynamic evidence for a nematic phase transition at the onset of the pseudogap in $YBa_2Cu_3O_{6+y}$", *Nature Physics*, **13**, 1074–1078, (2017).

[21] H. Murayama, Y. Sato, R. Kurihara, S. Kasahara, Y. Mizukami, Y. Kasahara, H. Uchiyama, A. Yamamoto, E.-G. Moon, J. Cai, J. Freyermuth, M. Greven, T. Shibauchi, and Y. Matsuda, "Diagonal nematicity in the pseudogap phase of $HgBa_2CuO_{4+\delta}$", *Nature Communications*, **10**, 3282, (2019).

[22] S. Mukhopadhyay, R. Sharma, C. K. Kim, S. D. Edkins, M. H. Hamidian, H. Eisaki, S. I. Uchida, E.-A. Kim, M. J. Lawler, A. P. Mackenzie, J. C. S. Davis, and K. Fujita, "Evidence for a vestigial nematic state in the cuprate pseudogap phase", *Proceedings of the National Academy of Sciences*, **116**, 13249–13254, (2019).

[23] D. F. Agterberg, J. C. S. Davis, S. D. Edkins, E. Fradkin, D. J. Van Harlingen, S. A. Kivelson, P. A. Lee, L. Radzihovsky, J. M. Tranquada, and Y. Wang, "The Physics of Pair-Density Waves: Cuprate Superconductors and Beyond", *Annual Review of Condensed Matter Physics*, **11**, 231–270, (2020).

[24] V. J. Emery and S. A. Kivelson, "Importance of phase fluctuations in superconductors with small superfluid density", *Nature*, **374**, 434–437, (1995).

[25] J. Corson, R. Mallozzi, J. Orenstein, J. N. Eckstein, and I. Bozovic, "Vanishing of phase coherence in underdoped $Bi_2Sr_2CaCu_2O_{8+\delta}$", *Nature*, **398**, 221, (1999).

[26] J. Orenstein, J. Corson, S. Oh, and J. Eckstein, "Superconducting fluctuations in $Bi_2Sr_2Ca_{1-x}Dy_xCu_2O_{8+\delta}$ as seen by terahertz spectroscopy", *Annalen der Physik*, **15**, 596, (2006).

[27] L. S. Bilbro, R. V. Aguilar, G. Logvenov, O. Pelleg, I. Božović, and N. P. Armitage, "Temporal correlations of superconductivity above the transition temperature in $La_{2-x}Sr_xCuO_4$ probed by terahertz spectroscopy", *Nature Physics*, **7**, 298–302, (2011).

[28] D. Nakamura, Y. Imai, A. Maeda, and I. Tsukada, "Superconducting Fluctuation Investigated by THz Conductivity of $La_{2-x}Sr_xCuO_4$ Thin Films", *Journal of the Physical Society of Japan*, **81**, 044709, (2012).

[29] H. Kitano, T. Ohashi, A. Maeda, and I. Tsukada, "Critical microwave-conductivity fluctuations across the phase diagram of superconducting $La_{2-x}Sr_xCuO_4$ thin films", *Physical Review B*, **73**, 092504, (2006).

[30] M. S. Grbić, N. Barišić, A. Dulčić, I. Kupčić, Y. Li, X. Zhao, G. Yu, M. Dressel, M. Greven, and M. Požek, "Microwave measurements of the in-plane and c-axis conductivity in $HgBa_2CuO_{4+\delta}$: Discriminating between superconducting fluctuations and pseudogap effects", *Physical Review B*, **80**, 094511, (2009).

[31] M. S. Grbić, M. Požek, D. Paar, V. Hinkov, M. Raichle, D. Haug, B. Keimer, N. Barišić, and A. Dulčić, "Temperature range of superconducting fluctuations above T_c in $YBa_2Cu_3O_{7-\delta}$ single crystals", *Physical Review B*, **83**, 144508, (2011).

[32] A. Dubroka, M. Rössle, K. W. Kim, V. K. Malik, D. Munzar, D. N. Basov, A. A. Schafgans, S. J. Moon, C. T. Lin, D. Haug, V. Hinkov, B. Keimer, T. Wolf, J. G. Storey, J. L. Tallon, and C. Bernhard, "Evidence of a Precursor Superconducting Phase at Temperatures as High as 180 K in $RBa_2Cu_3O_{7-\delta}$ (R = Y, Gd, Eu) Superconducting Crystals from Infrared Spectroscopy", *Physical Review Letters*, **106**, 047006, (2011).

[33] E. Uykur, K. Tanaka, T. Masui, S. Miyasaka, and S. Tajima, "Persistence of the Superconducting Condensate Far above the Critical Temperature of $YBa_2(Cu, Zn)_3O_y$ Revealed by c-Axis Optical Conductivity Measurements for Several Zn Concentrations and Carrier Doping Levels", *Physical Review Letters*, **112**, 127003, (2014).

[34] K. Lee, K. Kamiya, M. Nakajima, S. Miyasaka, and S. Tajima, "Investigation of Precursor Superconducting State in $YBa_2Cu_3O_{7-\delta}$ through In-Plane Optical Spectroscopy", *Journal of the Physical Society of Japan*, **86**, 023701, (2017).

[35] Y. Wang, Z. A. Xu, T. Kakeshita, S. Uchida, S. Ono, Y. Ando, and N. P. Ong, "Onset of the vortexlike Nernst signal above T_c in $La_{2-x}Sr_xCuO_4$ and $Bi_2Sr_{2-y}La_yCuO_6$", *Physical Review B*, **64**, 224519, (2001).

[36] Y. Wang, L. Li, and N. P. Ong, "Nernst effect in high-T_c superconductors", *Physical Review B*, **73**, 024510, (2006).

[37] Y. Wang, L. Li, M. J. Naughton, G. D. Gu, S. Uchida, and N. P. Ong, "Field-Enhanced Diamagnetism in the Pseudogap State of the Cuprate $Bi_2Sr_2CaCu_2O_{8+\delta}$ Superconductor in an Intense Magnetic Field", *Physical Review Letters*, **95**, 247002, (2005).

[38] L. Li, Y. Wang, M. J. Naughton, S. Ono, Y. Ando, and N. P. Ong, "Strongly nonlinear magnetization above T_c in $Bi_2Sr_2CaCu_2O_{8+\delta}$", *Europhysics Letters (EPL)*, **72**, 451, (2005).

[39] L. Li, Y. Wang, S. Komiya, S. Ono, Y. Ando, G. D. Gu, and N. P. Ong, "Diamagnetism and Cooper pairing above T_c in cuprates", *Physical Review B*, **81**, 054510, (2010).

[40] G. Yu, D.-D. Xia, D. Pelc, R.-H. He, N.-H. Kaneko, T. Sasagawa, Y. Li, X. Zhao, N. Barišić, A. Shekhter, and M. Greven, "Universal precursor of superconductivity in the cuprates", *Physical Review B*, **99**, 214502, (2019).

[41] K. K. Gomes, A. N. Pasupathy, A. Pushp, S. Ono, Y. Ando, and A. Yazdani, "Visualizing pair formation on the atomic scale in the high-T_c superconductor $Bi_2Sr_2CaCu_2O_{8+\delta}$", *Nature*, **447**, 569–572, (2007).

[42] T. Kondo, Y. Hamaya, A. D. Palczewski, T. Takeuchi, J. S. Wen, Z. J. Xu, G. Gu, J. Schmalian, and A. Kaminski, "Disentangling Cooper-pair formation above the transition temperature from the pseudogap state in the cuprates", *Nature Physics*, **7**, 21–25, (2011).

[43] T. Kondo, A. D. Palczewski, Y. Hamaya, T. Takeuchi, J. S. Wen, Z. J. Xu, G. D. Gu, and A. Kaminski, "Formation of Gapless Fermi Arcs and Fingerprints of Order in the Pseudogap State of Cuprate Superconductors", *Physical Review Letters*, **111**, 157003, (2013).

[44] T. J. Reber, N. C. Plumb, Y. Cao, Z. Sun, Q. Wang, K. McElroy, H. Iwasawa, M. Arita, J. S. Wen, Z. J. Xu, G. D. Gu, Y. Yoshida, H. Eisaki, Y. Aiura, and D. S. Dessau, "Prepairing and the "filling" gap in the cuprates from the tomographic density of states", *Physical Review B*, **87**, 060506, (2013).

[45] T. Kondo, W. Malaeb, Y. Ishida, T. Sasagawa, H. Sakamoto, T. Takeuchi, T. Tohyama, and S. Shin, "Point nodes persisting far beyond T_c in Bi2212", *Nature Communications*, **6**, 7699, (2015).

[46] W. Zhang, C. L. Smallwood, C. Jozwiak, T. L. Miller, Y. Yoshida, H. Eisaki, D.-H. Lee, and A. Lanzara, "Signatures of superconductivity and pseudogap formation in nonequilibrium nodal quasiparticles revealed by ultrafast angle-resolved photoemission", *Physical Review B*, **88**, 245132, (2013).

[47] I. Madan, T. Kurosawa, Y. Toda, M. Oda, T. Mertelj, P. Kusar, and D. Mihailovic, "Separating pairing from quantum phase coherence dynamics above the superconducting transition by femtosecond spectroscopy", *Scientific Reports*, **4**, 5656, (2015).

[48] L. Perfetti, B. Sciolla, G. Biroli, C. J. van der Beek, C. Piovera, M. Wolf, and T. Kampfrath, "Ultrafast Dynamics of Fluctuations in High-Temperature Superconductors Far from Equilibrium", *Physical Review Letters*, **114**, 067003, (2015).

[49] F. Giusti, A. Marciniak, F. Randi, G. Sparapassi, F. Boschini, H. Eisaki, M. Greven, A. Damascelli, A. Avella, and D. Fausti, "Signatures of Enhanced Superconducting Phase Coherence in Optimally

Doped $Bi_2Sr_2Y_{0.08}Ca_{0.92}Cu_2O_{8+\delta}$ Driven by Midinfrared Pulse Excitations", *Physical Review Letters*, **122**, 067002, (2019).

[50] O. Cyr-Choinière, R. Daou, F. Laliberté, D. LeBoeuf, N. Doiron-Leyraud, J. Chang, J.-Q. Yan, J.-G. Cheng, J.-S. Zhou, J. B. Goodenough, S. Pyon, T. Takayama, H. Takagi, Y. Tanaka, and L. Taillefer, "Enhancement of the Nernst effect by stripe order in a high-T_c superconductor", *Nature*, **458**, 743–745, (2009).

[51] C. Giannetti, M. Capone, D. Fausti, M. Fabrizio, F. Parmigiani, and D. Mihailovic, "Ultrafast optical spectroscopy of strongly correlated materials and high-temperature superconductors: a non-equilibrium approach", *Advances in Physics*, **65**, 58–238, (2016).

[52] D. Fausti, R. I. Tobey, N. Dean, S. Kaiser, A. Dienst, M. C. Hoffmann, S. Pyon, T. Takayama, H. Takagi, and A. Cavalleri, "Light-induced superconductivity in a stripe-ordered cuprate.", *Science*, **331**, 189–91, (2011).

[53] W. Hu, S. Kaiser, D. Nicoletti, C. R. Hunt, I. Gierz, M. C. Hoffmann, M. Le Tacon, T. Loew, B. Keimer, and A. Cavalleri, "Optically enhanced coherent transport in $YBa_2Cu_3O_{6.5}$ by ultrafast redistribution of interlayer coupling", *Nature Materials*, **13**, 705–711, (2014).

[54] S. Kaiser, C. R. Hunt, D. Nicoletti, W. Hu, I. Gierz, H. Y. Liu, M. Le Tacon, T. Loew, D. Haug, B. Keimer, and A. Cavalleri, "Optically induced coherent transport far above T_c in underdoped $YBa_2Cu_3O_{6+\delta}$", *Physical Review B*, **89**, 184516, (2014).

[55] C. R. Hunt, D. Nicoletti, S. Kaiser, D. Pröpper, T. Loew, J. Porras, B. Keimer, and A. Cavalleri, "Dynamical decoherence of the light induced interlayer coupling in $YBa_2Cu_3O_{6+\delta}$", *Physical Review B*, **94**, 224303, (2016).

[56] B. Liu, M. Först, M. Fechner, D. Nicoletti, J. Porras, T. Loew, B. Keimer, and A. Cavalleri, "Pump Frequency Resonances for Light-Induced Incipient Superconductivity in $YBa_2Cu_3O_{6.5}$", *Physical Review X*, **10**, 011053, (2020).

[57] S. J. Zhang, Z. X. Wang, H. Xiang, X. Yao, Q. M. Liu, L. Y. Shi, T. Lin, T. Dong, D. Wu, and N. L. Wang, "Photoinduced Nonequilibrium Response in Underdoped $YBa_2Cu_3O_{6+x}$ Probed by Time-Resolved Terahertz Spectroscopy", *Physical Review X*, **10**, 011056, (2020).

[58] D. Pekker and C. Varma, "Amplitude/Higgs Modes in Condensed Matter Physics", *Annual Review of Condensed Matter Physics*, **6**, 269–297, (2015).

[59] P. W. Anderson, "Random-Phase Approximation in the Theory of Superconductivity", *Physical Review*, **112**, 1900–1916, (1958).

[60] P. W. Anderson, "Coherent Excited States in the Theory of Superconductivity: Gauge Invariance and the Meissner Effect", *Physical Review*, **110**, 827–835, (1958).

[61] Y. Nambu, "Quasi-particles and gauge invariance in the theory of superconductivity", *Physical Review*, **117**, 648–663, (1960).

[62] J. Goldstone, A. Salam, and S. Weinberg, "Broken Symmetries", *Physical Review*, **127**, 965–970, (1962).

[63] F. Englert and R. Brout, "Broken symmetry and the mass of gauge vector mesons", *Physical Review Letters*, **13**, 321, (1964).

[64] P. W. Higgs, "Broken symmetries, massless particles and gauge fields", *Physics Letters*, **12**, 132–133, (1964).

[65] P. W. Higgs, "Broken symmetries and the masses of gauge bosons", *Physical Review Letters*, **13**, 508, (1964).

[66] R. Matsunaga, N. Tsuji, K. Makise, H. Terai, H. Aoki, and R. Shimano, "Polarization-resolved terahertz third-harmonic generation in a single-crystal superconductor NbN: Dominance of the Higgs mode beyond the BCS approximation", *Physical Review B*, **96**, 020505, (2017).

[67] R. Shimano and N. Tsuji, "Higgs Mode in Superconductors", *Annual Review of Condensed Matter Physics*, **11**, 103, (2020).

[68] A. F. Volkov and S. M. Kogan, "Collision less relaxation of the energy gap in superconductors", *Zh. Eksp. Teor. Fiz*, **65**, 2038, (1973).

[69] R. A. Barankov and L. S. Levitov, "Synchronization in the BCS Pairing Dynamics as a Critical Phenomenon", *Physical Review Letters*, **96**, 230403, (2006).

[70] E. A. Yuzbashyan and M. Dzero, "Dynamical Vanishing of the Order Parameter in a Fermionic Condensate", *Physical Review Letters*, **96**, 230404, (2006).

[71] E. A. Yuzbashyan, O. Tsyplyatyev, and B. L. Altshuler, "Relaxation and Persistent Oscillations of the Order Parameter in Fermionic Condensates", *Physical Review Letters*, **96**, 097005, (2006).

[72] T. Papenkort, V. M. Axt, and T. Kuhn, "Coherent dynamics and pump-probe spectra of BCS superconductors", *Physical Review B*, **76**, 224522, (2007).

[73] T. Papenkort, T. Kuhn, and V. M. Axt, "Coherent control of the gap dynamics of BCS superconductors in the nonadiabatic regime", *Physical Review B*, **78**, 132505, (2008).

[74] R. Sooryakumar and M. V. Klein, "Raman scattering by superconducting-gap excitations and their coupling to charge-density waves", *Physical Review Letters*, **45**, 660, (1980).

[75] P. B. Littlewood and C. M. Varma, "Gauge-invariant theory of the dynamical interaction of charge density waves and superconductivity", *Physical Review Letters*, **47**, 811–814, (1981).

[76] P. B. Littlewood and C. M. Varma, "Amplitude collective modes in superconductors and their coupling to charge-density waves", *Physical Review B*, **26**, 4883–4893, (1982).

[77] M.-A. Méasson, Y. Gallais, M. Cazayous, B. Clair, P. Rodière, L. Cario, and A. Sacuto, "Amplitude Higgs mode in the $2H$-$NbSe_2$ superconductor", *Physical Review B*, **89**, 060503(R), (2014).

[78] R. Grasset, T. Cea, Y. Gallais, M. Cazayous, A. Sacuto, L. Cario, L. Benfatto, and M.-A. Méasson, "Higgs-mode radiance and charge-density-wave order in $2H$-$NbSe_2$", *Physical Review B*, **97**, 094502, (2018).

[79] R. Grasset, Y. Gallais, A. Sacuto, M. Cazayous, S. Mañas-Valero, E. Coronado, and M.-A. Méasson, "Pressure-Induced Collapse of the Charge Density Wave and Higgs Mode Visibility in $2H$-TaS_2", *Physical Review Letters*, **122**, 127001, (2019).

[80] J. Hebling, G. Almasi, I. Kozma, and J. Kuhl, "Velocity matching by pulse front tilting for large area THz-pulse generation", *Optics Express*, **10**, 1161, (2002).

[81] T. Kampfrath, K. Tanaka, and K. A. Nelson, "Resonant and nonresonant control over matter and light by intense terahertz transients", *Nature Photonics*, **7**, 680–690, (2013).

[82] R. Matsunaga, Y. I. Hamada, K. Makise, Y. Uzawa, H. Terai, Z. Wang, and R. Shimano, "Higgs Amplitude Mode in the BCS Superconductors $Nb_{1-x}Ti_xN$ Induced by Terahertz Pulse Excitation", *Physical Review Letters*, **111**, 057002, (2013).

[83] R. Matsunaga, N. Tsuji, H. Fujita, A. Sugioka, K. Makise, Y. Uzawa, H. Terai, Z. Wang, H. Aoki, and R. Shimano, "Light-induced collective pseudospin precession resonating with Higgs mode in a superconductor", *Science*, **345**, 1145, (2014).

[84] R. Matsunaga and R. Shimano, "Nonlinear terahertz spectroscopy of Higgs mode in s-wave superconductors", *Physica Scripta*, **92**, 024003, (2017).

[85] K. Katsumi, N. Tsuji, Y. I. Hamada, R. Matsunaga, J. Schneeloch, R. D. Zhong, G. D. Gu, H. Aoki, Y. Gallais, and R. Shimano, "Higgs Mode in the d-Wave Superconductor $Bi_2Sr_2CaCu_2O_{8+x}$ Driven by an Intense Terahertz Pulse", *Physical Review Letters*, **120**, 117001, (2018).

[86] K. Katsumi, Z. Z. Li, H. Raffy, Y. Gallais, and R. Shimano, "Superconducting fluctuations probed by the Higgs mode in $Bi_2Sr_2CaCu_2O_{8+x}$ thin films", *Physical Review B*, **102**, 054510, (2020).

[87] H. Chu, M.-J. Kim, K. Katsumi, S. Kovalev, R. D. Dawson, L. Schwarz, N. Yoshikawa, G. Kim, D. Putzky, Z. Z. Li, H. Raffy, S. Germanskiy, J.-C. Deinert, N. Awari, I. Ilyakov, B. Green, M. Chen, M. Bawatna, G. Cristiani, G. Logvenov, Y. Gallais, A. V. Boris, B. Keimer, A. P.

Schnyder, D. Manske, M. Gensch, Z. Wang, R. Shimano, and S. Kaiser, "Phase-resolved Higgs response in superconducting cuprates", *Nature Communications*, **11**, 1793, (2020).

[88] N. Tsuji and H. Aoki, "Theory of Anderson pseudospin resonance with Higgs mode in superconductors", *Physical Review B*, **92**, 064508, (2015).

[89] T. Cea, C. Castellani, and L. Benfatto, "Nonlinear optical effects and third-harmonic generation in superconductors: Cooper pairs versus Higgs mode contribution", *Physical Review B*, **93**, 180507, (2016).

[90] T. Jujo, "Two-Photon Absorption by Impurity Scattering and Amplitude Mode in Conventional Superconductors", *Journal of the Physical Society of Japan*, **84**, 114711, (2015).

[91] N. Tsuji, Y. Murakami, and H. Aoki, "Nonlinear light-Higgs coupling in superconductors beyond BCS: Effects of the retarded phonon-mediated interaction", *Physical Review B*, **94**, 224519, (2016).

[92] T. Yu and M. W. Wu, "Gauge-invariant theory of quasiparticle and condensate dynamics in response to terahertz optical pulses in superconducting semiconductor quantum wells. I. s -wave superconductivity in the weak spin-orbit coupling limit", *Physical Review B*, **96**, 155311, (2017).

[93] T. Jujo, "Quasiclassical Theory on Third-Harmonic Generation in Conventional Superconductors with Paramagnetic Impurities", *Journal of the Physical Society of Japan*, **87**, 024704, (2018).

[94] T. Cea, P. Barone, C. Castellani, and L. Benfatto, "Polarization dependence of the third-harmonic generation in multiband superconductors", *Physical Review B*, **97**, 094516, (2018).

[95] F. Yang and M. W. Wu, "Gauge-invariant microscopic kinetic theory of superconductivity in response to electromagnetic fields", *Physical Review B*, **98**, 094507, (2018).

[96] Y. Murotani and R. Shimano, "Nonlinear optical response of collective modes in multiband superconductors assisted by nonmagnetic impurities", *Physical Review B*, **99**, 224510, (2019).

[97] M. Hashimoto, E. A. Nowadnick, R.-H. He, I. M. Vishik, B. Moritz, Y. He, K. Tanaka, R. G. Moore, D. Lu, Y. Yoshida, M. Ishikado, T. Sasagawa, K. Fujita, S. Ishida, S. Uchida, H. Eisaki, Z. Hussain, T. P. Devereaux, and Z.-X. Shen, "Direct spectroscopic evidence for phase competition between the pseudogap and superconductivity in $Bi_2Sr_2CaCu_2O_{8+\delta}$", *Nature Materials*, **14**, 37–42, (2015).

[98] K. Momma and F. Izumi, "An integrated three-dimensional visualization system VESTA using wxWidgets", *Commission on Crystallogr. Comput., IUCr Newslett*, **7**, 106–119, (2006).

[99] S. Tajima, G. D. Gu, S. Miyamoto, A. Odagawa, and N. Koshizuka, "Optical evidence for strong anisotropy in the normal and superconducting states in $Bi_2Sr_2CaCu_2O_{8+z}$", *Physical Review B*, **48**, 16164–16167, (1993).

[100] D. N. Basov and T. Timusk, "Electrodynamics of high-T_c superconductors", *Reviews of Modern Physics*, **77**, 721–779, (2005).

[101] C. C. Homes, T. Timusk, D. Bonn, R. Liang, and W. N. Hardy, "Optical properties along the c-axis of $YBa_2Cu_3O_{6+x}$, for $x = 0.50 \rightarrow 0.95$ evolution of the pseudogap", *Physica C: Superconductivity*, **254**, 265–280, (1995).

[102] T. Matsuoka, T. Fujimoto, K. Tanaka, S. Miyasaka, S. Tajima, K. Fujii, M. Suzuki, and M. Tonouchi, "Terahertz time-domain reflection spectroscopy for high-T_c superconducting cuprates", *Physica C: Superconductivity and its Applications*, **469**, 982–984, (2009).

[103] D. Van der Marel, H. J. A. Molegraaf, J. Zaanen, Z. Nussinov, F. Carbone, A. Damascelli, H. Eisaki, M. Greven, P. H. Kes, and M. Li, "Quantum critical behaviour in a high-T_c superconductor", *Nature*, **425**, 271–274, (2003).

[104] D. Van der Marel and A. A. Tsvetkov, "Transverse-optical Josephson plasmons: Equations of motion", *Physical Review B*, **64**, (2001).

[105] M. Tinkham, *Introduction to Superconductivity*, Dover Publications, 2 edition, (2004).

[106] S. Rajasekaran, J. Okamoto, L. Mathey, M. Fechner, V. Thampy, G. D. Gu, and A. Cavalleri, "Probing optically silent superfluid stripes in cuprates", *Science*, **359**, 575–579, (2018).

[107] R. W. Boyd, *Nonlinear Optics*, Academic Press, 3rd edition, (2008).

[108] J. Hebling, A. G. Stepanov, G. Almási, B. Bartal, and J. Kuhl, "Tunable THz pulse generation by optical rectification of ultrashort laser pulses with tilted pulse fronts", *Applied Physics. B: Lasers and Optics*, **78**, 593, (2004).

[109] H. Hirori, A. Doi, F. Blanchard, and K. Tanaka, "Single-cycle terahertz pulses with amplitudes exceeding 1 MV/cm generated by optical rectification in $LiNbO_3$", *Applied Physics Letters*, **98**, 091106, (2011).

[110] C. Winnewisser, P. U. Jepsen, M. Schall, V. Schyja, and H. Helm, "Electro-optic detection of THz radiation in $LiTaO_3$, $LiNbO_3$ and ZnTe", *Applied Physics Letters*, **70**, 3069, (1997).

[111] Y.-S. Lee, *Principles of terahertz science and technology*, Springer: New York, (2009).

[112] G. Cerullo and S. De Silvestri, "Ultrafast optical parametric amplifiers", *Review of Scientific Instruments*, **74**, 1, (2003).

[113] C. Manzoni and G. Cerullo, "Design criteria for ultrafast optical parametric amplifiers", *Journal of Optics*, **18**, 103501, (2016).

[114] D. Zhang, Y. Kong, and J.-y. Zhang, "Optical parametric properties of 532-nm-pumped beta-barium-borate near the infrared absorption edge", *Optics Communications*, **184**, 485, (2000).

[115] C.-W. Chen, Y.-K. Hsu, J. Y. Huang, C.-S. Chang, J.-Y. Zhang, and C.-L. Pan, "Generation properties of coherent infrared radiation in the optical absorption region of GaSe crystal", *Optics Express*, **14**, 10636, (2006).

[116] N. Dean, *Electronic and Structural Dynamics of Complex Materials*, PhD thesis, Jesus College, Oxford, (2011).

[117] S. Watanabe, N. Minami, and R. Shimano, "Intense terahertz pulse induced exciton generation in carbon nanotubes.", *Optics Express*, **19**, 1528, (2011).

[118] I. M. Vishik, M. Hashimoto, R.-H. He, W.-S. Lee, F. Schmitt, D. Lu, R. G. Moore, C. Zhang, W. Meevasana, T. Sasagawa, S. Uchida, K. Fujita, S. Ishida, M. Ishikado, Y. Yoshida, H. Eisaki, Z. Hussain, T. P. Devereaux, and Z.-X. Shen, "Phase competition in trisected superconducting dome", *Proceedings of the National Academy of Sciences*, **109**, 18332, (2012).

[119] H. Anzai, A. Ino, M. Arita, H. Namatame, M. Taniguchi, M. Ishikado, K. Fujita, S. Ishida, and S. Uchida, "Relation between the nodal and antinodal gap and critical temperature in superconducting Bi2212", *Nature Communications*, **4**, 1815, (2013).

[120] S. Benhabib, Y. Gallais, M. Cazayous, M.-A. Méasson, R. D. Zhong, J. Schneeloch, A. Forget, G. D. Gu, D. Colson, and A. Sacuto, "Three energy scales in the superconducting state of hole-doped cuprates detected by electronic Raman scattering", *Physical Review B*, **92**, 134502, (2015).

[121] M. C. Hoffmann, N. C. Brandt, H. Y. Hwang, K.-L. Yeh, and K. A. Nelson, "Terahertz Kerr effect", *Applied Physics Letters*, **95**, 231105, (2009).

[122] W. K. Burns and N. Bloembergen, "Third-harmonic generation in absorbing media of cubic or isotropic symmetry", *Physical Review B*, **4**, 3437–3450, (1971).

[123] D. Ricard, P. Roussignol, and C. Flytzanis, "Surface-mediated enhancement of optical phase conjugation in metal colloids", *Optics Letters*, **10**, 511, (1985).

[124] C. K. Sun, F. Vallée, L. H. Acioli, E. P. Ippen, and J. G. Fujimoto, "Femtosecond-tunable measurement of electron thermalization in gold", *Physical Review B*, **50**, 15337–15348, (1994).

[125] R. H. Groeneveld, R. Sprik, and A. Lagendijk, "Femtosecond spectroscopy of electron-electron and electron-phonon energy relaxation in Ag and Au", *Physical Review B*, **51**, 11433–11445, (1995).

[126] J. Hohlfeld, S. S. Wellershoff, J. Güdde, U. Conrad, V. Jähnke, and E. Matthias, "Electron and lattice dynamics following optical excitation of metals", *Chemical Physics*, **251**, 237–258, (2000).

[127] C. Gadermaier, A. S. Alexandrov, V. V. Kabanov, P. Kusar, T. Mertelj, X. Yao, C. Manzoni, D. Brida, G. Cerullo, and D. Mihailovic, "Electron-Phonon Coupling in High-Temperature Cuprate Superconductors Determined from Electron Relaxation Rates", *Physical Review Letters*, **105**, 257001, (2010).

[128] M. Conforti and G. Della Valle, "Derivation of third-order nonlinear susceptibility of thin metal films as a delayed optical response", *Physical Review B*, **85**, 245423, (2012).

[129] J. Corson, J. Orenstein, S. Oh, J. O'Donnell, and J. N. Eckstein, "Nodal Quasiparticle Lifetime in the Superconducting State of $Bi_2Sr_2CaCu_2O_{8+\delta}$", *Physical Review Letters*, **85**, 2569–2572, (2000).

[130] M. Dressel and G. Gruner, *Electrodynamics of Solids*, Cambridge University Press, (2002).

[131] J. Orenstein, "Optical conductivity of a superfluid density wave", *Physica C: Superconductivity*, **390**, 243–248, (2003).

[132] A. V. Puchkov, D. N. Basov, and T. Timusk, "The pseudogap state in high-T_c superconductors: An infrared study", *Journal of Physics Condensed Matter*, **8**, 10049–10082, (1996).

[133] J. Hwang, T. Timusk, and G. D. Gu, "High-transition-temperature superconductivity in the absence of the magnetic-resonance mode", *Nature*, **427**, 714–717, (2004).

[134] A. Kaminski, J. Mesot, H. Fretwell, J. C. Campuzano, M. R. Norman, M. Randeria, H. Ding, T. Sato, T. Takahashi, T. Mochiku, K. Kadowaki, and H. Hoechst, "Quasiparticles in the superconducting state of $Bi_2Sr_2CaCu_2O_{8+\delta}$", *Physical Review Letters*, **84**, 1788–1791, (2000).

[135] J. Zaanen, "Why the temperature is high", *Nature*, **430**, 512–513, (2004).

[136] J. A. Bruin, H. Sakai, R. S. Perry, and A. P. Mackenzie, "Similarity of scattering rates in metals showing T-linear resistivity", *Science*, **339**, 804–807, (2013).

[137] A. Legros, S. Benhabib, W. Tabis, F. Laliberté, M. Dion, M. Lizaire, B. Vignolle, D. Vignolles, H. Raffy, Z. Z. Li, P. Auban-Senzier, N. Doiron-Leyraud, P. Fournier, D. Colson, L. Taillefer, and C. Proust, "Universal T-linear resistivity and Planckian dissipation in overdoped cuprates", *Nature Physics*, **15**, 142–147, (2019).

[138] R. A. Ferrell and R. E. Glover III, "Conductivity of superconducting films: A sum rule", *Physical Review*, **109**, 1398, (1958).

[139] M. Tinkham and R. Ferrell, "Determination of the superconducting skin depth from the energy gap and sum rule", *Physical Review Letters*, **2**, 331, (1959).

[140] A. F. Santander-Syro, R. P. Lobo, N. Bontemps, W. Lopera, D. Giratá, Z. Konstantinovic, Z. Z. Li, and H. Raffy, "In-plane electrodynamics of the superconductivity in $Bi_2Sr_2CaCu_2O_{8+\delta}$: Energy scales and spectral weight distribution", *Physical Review B*, **70**, 134504, (2004).

[141] M. R. Presland, J. L. Tallon, R. G. Buckley, R. S. Liu, and N. E. Flower, "General trends in oxygen stoichiometry effects on T_c in Bi and Tl superconductors", *Physica C:*, **176**, 95, (1991).

[142] D. Pelc, M. Vučković, M. S. Grbić, M. Požek, G. Yu, T. Sasagawa, M. Greven, and N. Barišić, "Emergence of superconductivity in the cuprates via a universal percolation process", *Nature Communications*, **9**, 4327, (2018).

[143] P. Popčević, D. Pelc, Y. Tang, K. Velebit, Z. Anderson, V. Nagarajan, G. Yu, M. Požek, N. Barišić, and M. Greven, "Percolative nature of the direct-current paraconductivity in cuprate superconductors", *npj Quantum Materials*, **3**, 42, (2018).

[144] Y. Yamada and Y. Shiohara, "Continuous crystal growth of $YBa_2Cu_3O_{7-x}$ by the modified top-seeded crystal pulling method", *Physica C: Superconductivity and its applications*, **217**, 182–188, (1993).

[145] B. Liu, *Controlling superconductivity using tailored THz pulses*, PhD thesis, University of Hamburg, (2019).

[146] J. T. Kindt and C. A. Schmuttenmaer, "Theory for determination of the low-frequency time-dependent response function in liquids using time-resolved terahertz pulse spectroscopy", *The Journal of Chemical Physics*, **110**, 8589–8596, (1999).

[147] R. D. Averitt, G. Rodriguez, J. L. W. Siders, S. A. Trugman, and A. J. Taylor, "Conductivity artifacts in optical-pump THz-probe measurements of $YBa_2Cu_4O_7$", *Journal of the Optical Society of America B*, **17**, 327, (2000).

[148] H. Němec, F. Kadlec, and P. Kužel, "Methodology of an optical pump-terahertz probe experiment: An analytical frequency-domain approach", *Journal of Chemical Physics*, **117**, 8454–8465, (2002).

[149] H. Němec, F. Kadlec, S. Surendran, P. Kužel, and P. Jungwirth, "Ultrafast far-infrared dynamics probed by terahertz pulses: A frequency domain approach. I. Model systems", *The Journal of Chemical Physics*, **122**, 104503, (2005).

[150] H. Němec, F. Kadlec, C. Kadlec, P. Kužel, and P. Jungwirth, "Ultrafast far-infrared dynamics probed by terahertz pulses: A frequency-domain approach. II. Applications", *The Journal of Chemical Physics*, **122**, 104504, (2005).

[151] J. P. Revelle, A. Kumar, and A. F. Kemper, "Theory of Time-Resolved Optical Conductivity of Superconductors: Comparing Two Methods for Its Evaluation", *Condensed Matter*, **4**, 79, (2019).

[152] C. Giannetti, G. Coslovich, F. Cilento, G. Ferrini, H. Eisaki, N. Kaneko, M. Greven, and F. Parmigiani, "Discontinuity of the ultrafast electronic response of underdoped superconducting $Bi_2Sr_2CaCu_2O_{8+\delta}$ strongly excited by ultrashort light pulses", *Physical Review B*, **79**, 224502, (2009).

[153] L. Stojchevska, P. Kusar, T. Mertelj, V. V. Kabanov, Y. Toda, X. Yao, and D. Mihailovic, "Mechanisms of nonthermal destruction of the superconducting state and melting of the charge-density-wave state by femtosecond laser pulses", *Physical Review B*, **84**, 180507, (2011).

[154] P. Kusar, V. V. Kabanov, J. Demsar, T. Mertelj, S. Sugai, and D. Mihailovic, "Controlled Vaporization of the Superconducting Condensate in Cuprate Superconductors by Femtosecond Photoexcitation", *Physical Review Letters*, **101**, 227001, (2008).

[155] M. Beyer, D. Stadter, M. Beck, H. Schafer, V. V. Kabanov, G. Logvenov, I. Bozovic, G. Koren, and J. Demsar, "Photoinduced melting of superconductivity in the high-T_c superconductor $La_{2-x}Sr_xCuO_4$ probed by time-resolved optical and terahertz techniques", *Physical Review B*, **83**, 214515, (2011).

[156] Y. Toda, T. Mertelj, P. Kusar, T. Kurosawa, M. Oda, M. Ido, and D. Mihailovic, "Quasiparticle relaxation dynamics in underdoped $Bi_2Sr_2CaCu_2O_{8+\delta}$ by two-color pump-probe spectroscopy", *Physical Review B*, **84**, 174516, (2011).

[157] C. L. Smallwood, W. Zhang, T. L. Miller, C. Jozwiak, H. Eisaki, D.-H. H. Lee, and A. Lanzara, "Time- and momentum-resolved gap dynamics in $Bi_2Sr_2CaCu_2O_{8+\delta}$", *Physical Review B*, **89**, 115126, (2014).

[158] Z. Zhang, C. Piovera, E. Papalazarou, M. Marsi, M. D'Astuto, C. J. van der Beek, A. Taleb-Ibrahimi, and L. Perfetti, "Photoinduced filling of near-nodal gap in $Bi_2Sr_2CaCu_2O_{8+\delta}$", *Physical Review B*, **96**, 064510, (2017).

[159] S. J. Zhang, Z. X. Wang, L. Y. Shi, T. Lin, M. Y. Zhang, G. D. Gu, T. Dong, and N. L. Wang, "Light-induced new collective modes in the superconductor $La_{1.905}Ba_{0.095}CuO_4$", *Physical Review B*, **98**, 020506, (2018).

[160] H. Niwa, N. Yoshikawa, K. Tomari, R. Matsunaga, D. Song, H. Eisaki, and R. Shimano, "Light-induced nonequilibrium response of the superconducting cuprate $La_{2-x}Sr_xCuO_4$", *Physical Review B*, **100**, 104507, (2019).

[161] L. Perfetti, P. A. Loukakos, M. Lisowski, U. Bovensiepen, H. Eisaki, and M. Wolf, "Ultrafast Electron Relaxation in Superconducting $Bi_2Sr_2CaCu_2O_{8+\delta}$ by Time-Resolved Photoelectron Spectroscopy", *Physical Review Letters*, **99**, 197001, (2007).

[162] S. C. Riggs, O. Vafek, J. B. Kemper, J. B. Betts, A. Migliori, F. F. Balakirev, W. N. Hardy, R. Liang, D. A. Bonn, and G. S. Boebinger, "Heat capacity through the magnetic-field-induced resistive transition in an underdoped high-temperature superconductor", *Nature Physics*, **7**, 332–335, (2011).

[163] J. Kemper, *Measurement of the heat capacity of cuprate superconductors in high magnetic fields*, PhD thesis, College of arts and science, Florida State University, (2014).

[164] R. Ulbricht, E. Hendry, J. Shan, T. F. Heinz, and M. Bonn, "Carrier dynamics in semiconductors studied with time-resolved terahertz spectroscopy", *Reviews of Modern Physics*, **83**, 543–586, (2011).

[165] S. L. Cooper, D. Reznik, A. Kotz, M. A. Karlow, R. Liu, M. V. Klein, W. C. Lee, J. Giapintzakis, D. M. Ginsberg, B. W. Veal, and A. P. Paulikas, "Optical studies of the a-, b-, and c-axis charge dynamics in $YBa_2Cu_3O_{6+x}$", *Physical Review B*, **47**, 8233–8248, (1993).

[166] B. Fauqué, Y. Sidis, V. Hinkov, S. Pailhès, C. T. Lin, X. Chaud, and P. Bourges, "Magnetic order in the pseudogap phase of high-T_c superconductors", *Physical Review Letters*, **96**, 197001, (2006).

[167] R. Daou, J. Chang, D. Leboeuf, O. Cyr-Choinière, F. Laliberté, N. Doiron-Leyraud, B. J. Ramshaw, R. Liang, D. A. Bonn, W. N. Hardy, and L. Taillefer, "Broken rotational symmetry in the pseudogap phase of a high-T_c superconductor", *Nature*, **463**, 519–522, (2010).

[168] R. D. Averitt, G. Rodriguez, A. I. Lobad, J. L. W. Siders, S. A. Trugman, and A. J. Taylor, "Nonequilibrium superconductivity and quasiparticle dynamics in $YBa_2Cu_3O_{7-\delta}$", *Physical Review B*, **63**, 140502, (2001).

[169] R. A. Kaindl, M. A. Carnahan, D. S. Chemla, S. Oh, and J. N. Eckstein, "Dynamics of Cooper pair formation in $Bi_2Sr_2CaCu_2O_{8+\delta}$", *Physical Review B*, **72**, 060510, (2005).

[170] P. J. Turner, R. Harris, S. Kamal, M. E. Hayden, D. M. Broun, D. C. Morgan, A. Hosseini, P. Dosanjh, G. K. Mullins, J. S. Preston, R. Liang, D. A. Bonn, and W. N. Hardy, "Observation of Weak-Limit

Quasiparticle Scattering via Broadband Microwave Spectroscopy of a *d*-Wave Superconductor", *Physical Review Letters*, **90**, 4, (2003).

[171] M. A. Quijada, D. B. Tanner, R. J. Kelley, M. Onellion, H. Berger, and G. Margaritondo, "Anisotropy in the *ab*-plane optical properties of $Bi_2Sr_2CaCu_2O_8$ single-domain crystals", *Physical Review B*, **60**, 14917–14934, (1999).

[172] 濱田裕紀、富田圭祐、泊開人、松永隆佑、李祈願、宮坂茂樹、田島節子、島野亮, "$YBa_2Cu_3O_y$ 単結晶におけるテラヘルツ波パルス誘起超高速コヒーレント非線形光学応答", 日本物理学会講演概要集, **71**, 1282, (2016).

[173] M. Opel, R. Nemetschek, M. C. Hoffmann, R. Philipp, P. F. Müller, R. Hackl, I. Tüttő, A. Erb, B. Revaz, E. Walker, H. Berger, and L. Forró, "Carrier relaxation, pseudogap, and superconducting gap in high-T_c cuprates: A Raman scattering study", *Physical Review B*, **61**, 9752, (2000).

[174] M. Le Tacon, A. Sacuto, A. Georges, G. Kotliar, Y. Gallais, D. Colson, and A. Forget, "Two energy scales and two distinct quasiparticle dynamics in the superconducting state of underdoped cuprates", *Nature Physics*, **2**, 537–543, (2006).

[175] S. Blanc, Y. Gallais, M. Cazayous, M.-A. Méasson, A. Sacuto, A. Georges, J. S. Wen, Z. J. Xu, G. D. Gu, and D. Colson, "Loss of antinodal coherence with a single *d*-wave superconducting gap leads to two energy scales for underdoped cuprate superconductors", *Physical Review B*, **82**, 144516, (2010).

[176] Q. Chen, I. Kosztin, B. Jankó, and K. Levin, "Pairing fluctuation theory of superconducting properties in underdoped to overdoped cuprates", *Physical Review Letters*, **81**, 4708–4711, (1998).

[177] C. C. Chien, Y. He, Q. Chen, and K. Levin, "Two-energy-gap preformed-pair scenario for cuprate superconductors: Implications for angle-resolved photoemission spectroscopy", *Physical Review B*, **79**, (2009).

[178] P. U. Jepsen and B. M. Fischer, "Dynamic range in terahertz time-domain transmission and reflection spectroscopy", *Optics Letters*, **30**, 29, (2005).

[179] P. U. Jepsen, D. G. Cooke, and M. Koch, "Terahertz spectroscopy and imaging - Modern techniques and applications", *Laser and Photonics Reviews*, **5**, 124–166, (2011).

[180] H. A. Hafez, S. Kovalev, J.-C. Deinert, Z. Mics, B. Green, N. Awari, M. Chen, S. Germanskiy, U. Lehnert, J. Teichert, Z. Wang, K.-J. Tielrooij, Z. Liu, Z. Chen, A. Narita, K. Müllen, M. Bonn, M. Gensch, and D. Turchinovich, "Extremely efficient terahertz high-harmonic generation in graphene by hot Dirac fermions", *Nature*, **561**, 507–511, (2018).

[181] S. Chakravarty, A. Sudbø, P. W. Anderson, and S. Strong, "Interlayer tunneling and gap anisotropy in high-temperature superconductors", *Science*, **261**, 337–340, (1993).

[182] O. K. Andersen, A. I. Liechtenstein, O. Jepsen, and F. Paulsen, "LDA energy bands, low-energy hamiltonians, t', t'', $t_\perp(\mathbf{k})$, and $J_\perp$", *Journal of Physics and Chemistry of Solids*, **56**, 1573–1591, (1995).

[183] L. B. Ioffe and A. J. Millis, "Superconductivity and the c axis spectral weight of high-T_c superconductors", *Science*, **285**, 1241–1244, (1999).

[184] C. Bernhard, L. Yu, A. Dubroka, K. W. Kim, M. Rössle, D. Munzar, J. Chaloupka, C. T. Lin, and T. Wolf, "Broad-band infrared ellipsometry measurements of the c-axis response of underdoped $YBa_2Cu_3O_{7-\delta}$: Spectroscopic distinction between the normal-state pseudogap and the superconducting gap", *Journal of Physics and Chemistry of Solids*, **69**, 3064–3069, (2008).

[185] M. C. Beard, G. M. Turner, and C. A. Schmuttenmaer, "Transient photoconductivity in GaAs as measured by time-resolved terahertz spectroscopy", *Physical Review B*, **62**, 15764–15777, (2000).

[186] B. Loret, N. Auvray, G. D. Gu, A. Forget, D. Colson, M. Cazayous, Y. Gallais, I. Paul, M. Civelli, and A. Sacuto, "Universal relationship between the energy scales of the pseudogap phase, the superconducting

state, and the charge-density-wave order in copper oxide superconductors", *Physical Review B*, **101**, 214520, (2020).

[187] H. J. A. Molegraaf, C. Presura, D. Van der Marel, P. H. Kes, M. Li, B. Keimer, and C. Bernhard, "Superconductivity-induced transfer of in-plane spectral weight in $Bi_2Sr_2CaCu_2O_{8+\delta}$.", *Science*, **295**, 2239–2241, (2002).

[188] A. B. Kuzmenko, H. J. A. Molegraaf, F. Carbone, and D. Van der Marel, "Temperature-modulation analysis of superconductivity-induced transfer of in-plane spectral weight in $Bi_2Sr_2CaCu_2O_8$", *Physical Review B*, **72**, 144503, (2005).

[189] R. E. Stephens and I. H. Malitson, "Index of refraction of magnesium oxide", *Journal of Research of the National Bureau of Standards*, **49**, 249–252, (1952).

[190] M. Sajadi, M. Wolf, and T. Kampfrath, "Terahertz-field-induced optical birefringence in common window and substrate materials", *Optics Express*, **23**, 28985, (2015).

Publication

Article

1. K. Katsumi, N. Tsuji, and Y. I. Hamada, and R. Matsunaga, J. Schneeloch, and R. D. Zhong, and G. D. Gu, and H. Aoki, and Y. Gallais, and R. Shimano,"Higgs mode in the *d*-wave superconductor $Bi_2Sr_2CaCu_2O_{8+x}$ driven by an intense terahertz pulse", *Physical Review Letters* **120**, 117001 (2018). *Editors' suggestion.*

2. H. Chu, M.-J. Kim, K. Katsumi, S. Kovalev, R. D. Dawson, L. Schwarz, N. Yoshikawa, G. Kim, D. Putzky, Z. Z. Li, H. Raffy, S. Germanskiy, J.-C. Deinert, N. Awari, I. Ilyakov, B. Green, M. Chen, M. Bawatna, G. Christiani, G. Logvenov, Y. Gallais, A. V. Boris, B. Keimer, A. Schnyder, D. Manske, M. Gensch, Z. Wang, R. Shimano and S. Kaiser, "Phase-resolved Higgs response in superconducting cuprates", *Nature Communications* **11**, 1793 (2020).

3. K. Katsumi, Z. Z. Li, H. Raffy, Y. Gallais, and R. Shimano, "Superconducting fluctuations probed by the Higgs mode in $Bi_2Sr_2CaCu_2O_{8+x}$ thin films", *Physical Review B* **102**, 054510 (2020).

4. S. Nakamura, K. Katsumi, H. Terai and R. Shimano, "Nonreciprocal Terahertz Second Harmonic Generation in Superconducting NbN under Supercurrent Injection", *Physical Review Letters* **125**, 097004 (2020).

Review article

1. 島野亮、室谷悠太、勝見恒太、固体物理、「高強度テラヘルツ・赤外パルスが拓く非平衡物性」、第 54 巻、第 11 号、623-636 (2019).

International Conference

1. K. Katsumi, Y. I. Hamada, R. Matsunaga, J. Schneeloch, R. D. Zhong, G. D. Gu, Y. Gallais, and R. Shimano, "Exploring THz-induced dynamics of a *d*-wave superconducting condensate in the cuprate $Bi_2Sr_2CaCu_2O_{8+\delta}$" 6th International Conference on Photoinduced Phase Transitions PIPT6, Sendai, Japan, (June 4th - 9th, 2017).

2. K. Katsumi, R. Matsunaga, J. Schneeloch, R. D. Zhong, G. D. Gu, Y. Gallais, and R. Shimano, "Terahertz pulse induced non-equilibrium dynamics of a *d*-wave cuprate superconductor", International School and Workshop on Electronic Crystals ECRYS-2017, Poster, Corse, France, (August 21st - September 2nd, 2017).

3. K. Katsumi, N. Tsuji, and Y. I. Hamada, and R. Matsunaga, J. Schneeloch, and R. D. Zhong, and G. D. Gu, and H. Aoki, and Y. Gallais, and R. Shimano, "Observation of Higgs mode in the d-wave superconductor $Bi_2Sr_2CaCu_2O_{8+\delta}$ by THz pump-optical probe spectroscopy", Low Energy Electrodynamics of Solids LEES 2018, Poster, Portonovo, Italy, (June 24th-29th, 2018).

4. K. Katsumi, Z. Z. Li, H. Raffy, Y. Gallais, and R. Shimano, "Observation of superconducting fluctuation in $Bi_2Sr_2CaCu_2O_{8+x}$ thin films by the intense terahertz pulse-driven Higgs mode", 2018 Workshop of Max Planck-UBC-UTokyo Center for Quantum Materials, Poster, Hongo, Japan, (December 9th-11th, 2018).

5. K. Katsumi, Z. Z. Li, H. Raffy, Y. Gallais, and R. Shimano, "Study of superconducting fluctuation in cuprate superconductors through the observation of Higgs mode oscillation", Spectroscopies in Novel Superconductors SNS2019, Poster, Hongo, Japan, (June 16th-21th, 2019).

6. K. Katsumi, Z. Z. Li, H. Raffy, Y. Gallais, and R. Shimano, "Superconducting fluctuation probed by the terahertz pulse-driven Higgs mode in $Bi_2Sr_2CaCu_2O_{8+x}$ thin films", 2019 Workshop of Max Planck-UBC-UTokyo Center for Quantum Materials, Poster, Vancouver, Canada (December 9th-10th, 2019).

Domestic Conference

1. 勝見恒太、濱田裕紀、松永隆佑、Y. Gallais、島野亮、“$Bi_2Sr_2CaCu_2O_{8+x}$ 単結晶における高強度テラヘルツ波励起非平衡ダイナミクス”、第 9 回文部科学省「最先端の光の創成を目指したネットワーク研究拠点プログラム」シンポジウム、講演番号 E-21、弘済会館, (2017 年 1 月).

2. 勝見恒太、濱田裕紀、松永隆佑、R. D. Zhong、J. Schneeloch、G. D. Gu、Y. Gallais、島野亮、“ 高温超伝導体 $Bi_2Sr_2CaCu_2O_{8+x}$ 単結晶におけるテラヘルツ波励起非平衡ダイナミクス ”、第 8 回低温センター研究交流会、講演番号 P-40、東京大学、(2017 年 2 月).

3. 勝見恒太、濱田裕紀、松永隆佑、R. D. Zhong、J. Schneeloch、G. D. Gu、Y. Gallais、島野亮、“ $Bi_2Sr_2CaCu_2O_{8+x}$ 単結晶におけるテラヘルツ波励起非平衡ダイナミクス”、2017 年日本物理学会第 72 回年次大会、講演番号 18aB14-12、大阪大学、(2017 年 3 月).

4. 勝見恒太、辻直人、濱田裕紀、松永隆佑、R. D. Zhong、J. Schneeloch、G. D. Gu、青木秀夫、Y. Gallais、島野亮、“ $Bi_2Sr_2CaCu_2O_{8+x}$ 単結晶における高強度テラヘルツ波励起非平衡ダイナミクス ”、第 10 回文部科学省「最先端の光の創成を目指したネットワーク研究拠点プログラム」シンポジウム、講演番号 E17、京都大学、(2018 年 1 月).

5. 勝見恒太、辻直人、濱田裕紀、松永隆佑、R. D. Zhong、J. Schneeloch、G. D. Gu、青木秀夫、Y. Gallais、島野亮、“ 高強度テラヘルツパルスを用いた d 波超伝導体 $Bi_2Sr_2CaCu_2O_{8+x}$ におけるヒッグスモードの観測 ”、第 9 回低温センター研究交流会、講演番号 O-04、東京大学、(2018 年 2 月).

6. 勝見恒太，R. Grasset，Y. Gallais，J. Higgins，R. Greene，島野亮、“ Higgs spectroscopy in a d-wave superconductor ”、第 9 回低温センター研究交流会、講演番号 P-42、東京大学、(2018 年 2 月).

7. 勝見恒太、Z. Z. Li、H. Raffy、Y. Gallais、島野亮、“ 高強度テラヘルツ波パルス誘起ヒッグスモードを用いた $Bi_2Sr_2CaCu_2O_{8+x}$ 薄膜における超伝導ゆらぎの研究 ”、第 10 回低温センター研究交流会、講演番号 P-07、東京大学、(2019 年 2 月).

8. 勝見恒太、Z. Z. Li、H. Raffy、Y. Gallais、島野亮、“ テラヘルツ波誘起ヒッグスモードを用いた $Bi_2Sr_2CaCu_2O_{8+x}$ 薄膜における超伝導ゆらぎ

の観測”、2019 年日本物理学会第 74 回年次大会、講演番号 15aS-PS-35、九州大学、(2019 年 3 月).

9. 中村祥子、富田圭祐、勝見恒太、寺井弘高、島野亮、“電流注入下の s 波超伝導体 NbN におけるテラヘルツ第 2 高調波発生”、2019 年日本物理学会第 74 回年次大会、講演番号 14pK207-10、九州大学、(2019 年 3 月).

10. 中村祥子、勝見恒太、寺井弘高、島野亮、“電流注入下の s 波超伝導体 NbN におけるピン止めされた磁束に由来する偶数次高調波発生”、2019 年日本物理学会秋季大会、講演番号 12pK36-9、岐阜大学、(2019 年 9 月).

11. 勝見恒太、Z. Z. Li、H. Raffy、Y. Gallais、島野亮、“ヒッグスモードを用いた銅酸化物超伝導体 $Bi_2Sr_2CaCu_2O_{8+x}$ における超伝導ゆらぎの観測”、第 11 回低温センター研究交流会、講演番号 P-05、東京大学、(2020 年 2 月).

12. 礒山和基、吉川尚孝、J. Wong、勝見恒太、色摩直樹、崎下雄稀、鍋島冬樹、前田京剛、島野亮、“テラヘルツ波で見る鉄系超伝導体 $FeSe_{0.5}Te_{0.5}$ の光励起状態”、第 11 回低温センター研究交流会、講演番号 P-06、東京大学、(2020 年 2 月).

13. 西田森彦、勝見恒太、島野亮、光パラメトリック増幅と差周波発生を用いた中赤外光源の開発”、第 11 回低温センター研究交流会、講演番号 P-08、東京大学、(2020 年 2 月).

14. 中村祥子、勝見恒太、寺井弘高、島野亮、“電流注入下の s 波超伝導体 NbN における非相反テラヘルツ第 2 高調波発生”、第 11 回低温センター研究交流会、講演番号 P-47、東京大学、(2020 年 2 月).

15. 礒山和基、吉川尚孝、J. Wong、勝見恒太、色摩直樹、崎下雄稀、鍋島冬樹、前田京剛、島野亮、“光励起された鉄系超伝導体 $FeSe_{0.5}Te_{0.5}$ からのテラヘルツ第 3 高調波発生”、 2020 年日本物理学会第 75 回年次大会、講演番号 18p-PSB-149、名古屋大学、(2020 年 3 月).

16. 勝見恒太、西田森彦、宮坂茂樹、田島節子、島野亮、“銅酸化物超伝導体 $YBa_2Cu_3O_y$ における光励起非平衡ダイナミクス”、日本物理学会 2020 年秋季大会、講演番号 11aE1-4、オンライン開催、(2020 年 9 月).

17. 礒山和基、吉川尚孝、勝見恒太、J. Wong、色摩直樹、崎下雄稀、鍋島冬樹、前田京剛、島野亮、“鉄系超伝導体 $FeSe_{0.5}Te_{0.5}$ における光誘起超伝導増強、日本物理学会 2020 年秋季大会、講演番号 11aE1-3、オンライン開催、(2020 年 9 月).

18. 中村祥子、勝見恒太、寺井弘高、島野亮、“テラヘルツ第 2 高調波発生から見る超伝導 NbN における磁束量子ダイナミクス、日本物理学会 2020 年秋季大会、講演番号 8aF1-4、オンライン開催、(2020 年 9 月).

Award

1. *PIPT6 Best Poster Award*, 6th International Conference on Photoinduced Phase Transitions PIPT6, Sendai, Japan, (June 4th - 9th, 2017).

2. 2018 *Research Incentive Award* (Master Course), Graduate School of Science, The University of Tokyo, (March 22th, 2018)

3. *SNS Young Researchers Award*, International conference on Spectroscopies in Novel Superconductors (SNS2019), Hongo, Japan.

Acknowledgments

I would like to express my sincere gratitude to everyone who helped and supported me during my graduate school.

First of all, I would like to thank my supervisor, Prof. Ryo Shimano, for inspiring me to attain my research project. Also, I acknowledge his kind advice that really helped me improve my skills in writing articles and make presentations.

Prof. Yann Gallais at Université de Paris supported me when performing my experiments and writing articles by giving fruitful advice to interpret the data in my master course. Even in my doctoral course, he kindly helped me write the article. I really acknowledge his support.

I am grateful to Assistant Prof. Naotaka Yoshikawa for not only helping me proceed with my experiments but also giving me a lot of his knowledge, especially to handle mid-infrared pulses. The experiment with him in Dresden was one of the precious experience in my doctoral course.

I would like to thank Project Assistant Prof. Sachiko Nakamura for telling me about the cryogenic technique and sample preparation. It was my pleasure to work with her on the fantastic experiment of the terahertz second-harmonic generation in NbN under current injection.

Associate Prof. Ryusuke Matsunaga at ISSP, the previous assistant professor in our group, taught me fundamental experimental skills in my master course. I acknowledge his support and helping me improve my presentation skills and writing applications.

I am grateful to Yuki I. Hamada for not only improving my skills for performing experiments and analyzing data but also building the intense terahertz pulse-generation system in my master course.

I would like to thank Associate Prof. Naoto Tsuji at Physics depertment in University of Tokyo and Prof. Hideo Aoki at AIST for fruitful discussion and calculating the nonlinear susceptibility, which greatly helped our

interpretation of the Higgs mode in my master course.

I am grateful to thank Prof. Shigeki Miyasaka and Prof. Setsuko Tajima at Osaka University for supplying us with high-quality YBCO single crystals and giving valuable comments on my experiments.

Junior Prof. Stefan Kaiser at the Max Planck Institute for Solid State Research in Stuttgart collaborated with us to develop the optical parametric amplifier. I would like to appreciate his kind help. This collaboration was achieved by the Max Planck-UBC-UTokyo center for quantum materials.

I would like to thank the sample providers, John Schneeloch, Ruidan D. Zhong, and Genda D. Gu at Brookhaven National Lab, for supplying us with high quality BSCCO single crystals. I would also like to thank the sample providers, Zhi Z. Li and Hélène Raffy at Université Paris-Saclay, for providing us with excellent BSCCO thin films.

I also would like to thank my ALPS secondary supervisors Prof. Atushi Fujimori and Prof. Tetsuya Hasegawa, for giving me precious comments from different research areas.

The assistant Prof. Takenori Fujii and Dr. Ryo Toda at Cryogenic Research Center helped me use SQUID many times and polish the samples. I would like to appreciate their support.

I want to thank all of my group members, Takuya Sawano, Hiroaki Niwa, Yudai Iida, Kazuki Isoyama, Yoshua Hirai, Morihiko Nishida, Kunio Nishizawa, and Haruki Matsumoto, for sharing their time. I would like to express my special gratitude to Morihiko Nishida for working with me patiently. Also, I would like to thank Hiroaki Niwa for carefully reading this thesis and giving feedback.

I want to thank alumni of my group, Dr. Fumiya Sekiguchi, Dr. Go Yumoto, Dr. Masayuki Takayama, Dr. Keisuke Tomita, Dr. Romain Grasset, Kaito Tomari, Dr. Yuta Murotani, Hiroki Suganuma, and Jeremy Wong.

I would like to thank Mayuko Niwata, Eriko Sekine, and Yoko Sasaki for helping me with endless paperwork.

Besides, I would like to appreciate the financial support from JSPS.

Finally, I would like to be grateful to my family for supporting me every day.